SURFACE FUNCTIONALIZED POLY-LACTIC ACID (PLA) SCAFFOLDS
FOR BONE TISSUE ENGINEERING

A THESIS SUBMITTED TO
THE GRADUATE SCHOOL OF NATURAL AND APPLIED SCIENCES
OF
MIDDLE EAST TECHNICAL UNIVERSITY

BY

MAHSA MONIRIZAD

IN PARTIAL FULFILLMENT OF THE REQUIREMENTS
FOR
THE DEGREE OF MASTER OF SCIENCE
IN
ENGINEERING SCIENCES

FEBRUARY 2022

Approval of the thesis:

SURFACE FUNCTIONALIZED POLY-LACTIC ACID (PLA) SCAFFOLDS FOR BONE TISSUE ENGINEERING

submitted by **MAHSA MONIRIZAD** in partial fulfillment of the requirements for the degree of **Master of Science** in **Engineering Sciences, Middle East Technical University** by,

Prof. Dr. Halil Kalıpçılar
Dean, Graduate School of **Natural and Applied Sciences**   _____

Prof. Dr. Murat Dicleli
Head of the Department, **Engineering Sciences**   _____

Prof. Dr. Dilek Keskin
Supervisor, **Engineering Sciences, METU**   _____

Dr. Menekşe Ermiş Şen
Co-Supervisor, **BIOMATEN, METU**   _____

Examining Committee Members:

Prof. Dr. Caner Durucan
Metallurgical and Materials Eng., METU   _____

Prof. Dr. Dilek Keskin
Engineering Sciences, METU   _____

Prof. Dr. Sreeparna Banerjee
Biological Sciences, METU   _____

Prof. Dr. Ayşen Tezcaner
Engineering Sciences, METU   _____

Asst. Prof. Dr. Ali Deniz Dalgıç
Genetics and Bioengineering, Istanbul Bilgi University   _____

Date: 10.02.2022

I hereby declare that all information in this document has been obtained and presented in accordance with academic rules and ethical conduct. I also declare that, as required by these rules and conduct, I have fully cited and referenced all material and results that are not original to this work.

Name Last name: Mahsa Monirizad

Signature:

ABSTRACT

SURFACE FUNCTIONALIZED POLY-LACTIC ACID (PLA) SCAFFOLDS FOR BONE TISSUE ENGINEERING

Monirizad, Mahsa
Master of Science, Engineering Sciences
Supervisor: Prof. Dr. Dilek Keskin
Co-Supervisor: Dr. Menekşe Ermiş Şen

February 2022, 189 pages

The need for more effective tissue grafts for orthopedic applications is one of the main research areas of tissue engineering. In bone tissue engineering (BTE), scaffolds that can mimic bone tissue both from mechanical and biological perspectives are investigated mostly. In this study, it was aimed to develop a BTE scaffold that can mimic bone ECM, mechanical strength and cell biocompatibility in a single design and thus, various groups of scaffolds were characterized in terms of mechanical, biocompatibility, and osteogenic properties. Poly (lactic acid) was used to 3D print main scaffold frame with different internal architectures. Two sets of experiments were designed in this thesis, i) 10 different geometries were chosen according to their porosity and pore structures, alkali treated and coated with type I collagen and bioglass (BG) nanoparticles, to mimic organic and mineral matrix of the bone, ii) 3D scaffolds with 3 different geometries were selected and filled with Collagen, 0.5% BG and cell laden GelMA hydrogel to provide an interconnected cell migration and proliferation network. The 3D printed PLA scaffolds used in the first set of experiments, in general, displayed good biocompatibility, cell adhesion,

proliferation, and differentiation. Moreover, the candidate 3D scaffolds in both sets, successfully matched the mechanical properties of the trabecular bone. Voronoi-type scaffolds presented better elastic modulus, yield strength, cell proliferation and migration both in GelMA filled and collagen-coated scaffolds compared to other geometries. The osteogenic characterization of alkali modified Collagen-BG coated scaffolds, showed better results compared to untreated scaffolds.

Keywords: Bone Tissue Engineering, 3D Printing, Scaffold Architecture, Composite Coating, Methacrylated Gelatin

ÖZ

KEMİK DOKU MÜHENDİSLİĞİ İÇİN YÜZEY FONKSİYONELLEŞTİRİLMİŞ POLİ-LAKTİK ASİT (PLA) İSKELELER

Monirizad, Mahsa
Yüksek Lisans, Mühendislik Bilimleri
Tez Yöneticisi: Prof. Dr. Dilek Keskin
Ortak Tez Yöneticisi: Öğr. Gör. Dr. Menekşe Ermiş Şen

Şubat 2022, 189 sayfa

Ortopedik uygulamalar için daha etkili doku greftlerine olan ihtiyaç doku mühendisliğinin temel araştırma alanlarından biridir. Kemik doku mühendisliğinde (BTE) çoğunlukla kemik dokusunu hem mekanik hem de biyolojik açıdan taklit edebilen doku iskeleleri araştırılmaktadır. Bu çalışmada, tek bir tasarımda kemik dokunun ECM, mekanik mukavemet ve hücre biyouyumluluğunu taklit edebilen bir BTE iskelesi geliştirilmesi amaçlanmış ve çeşitli iskele grupları mekanik, biyouyumluluk ve osteojenik özellikler açısından karakterize edilmiştir. Farklı iç mimarilere sahip ana iskele çerçevesini 3B baskı yöntemi ile oluşturmak için poli (laktik asit) kullanılmıştır. Çalışmada iki deney seti tasarlanmıştır, i) kemiğin organik ve mineral matrisini taklit etmek için gözeneklilik ve gözenek yapılarına göre 10 farklı geometri seçilmiş, alkali çözelti ile modifiye edilmiş ve tip I kollajen ve biyocam (BG) nanopartiküllerle kaplanmıştır, ii) 3 farklı 3B geometriye sahip iskele seçilmiş ve bağlantılı bir hücre göçü ve çoğalma ağı sağlamak için Kollajen, %0.5 BG ve hücre yüklü GelMA hidrojel ile doldurulmuştur. İlk deney setinde kullanılan 3B basılmış PLA iskeleler biyouyumluluk, hücre yapışması, çoğalma ve farklılaşma yönlerinden iyi performans sergilemiştir. Ayrıca, her iki setteki aday 3B

doku iskeleleri, trabeküler kemiğin mekanik özelliklerini başarıyla yansıtmıştır. Voronoi tipi iskeleler, diğer geometrilere kıyasla hem GelMA dolgulu hem de kolajen kaplı gruplarda daha yüksek elastik modül, akma mukavemeti, hücre proliferasyonu ve migrasyonu göstermiştir. Alkali modifiye edilmiş, Collagen-BG kaplı iskelelerin osteojenik karakterizasyonu, işlenmemiş iskelelere kıyasla daha iyi sonuçlar vermiştir.

Anahtar Kelimeler: Kemik Doku Mühendisliği, 3B Baskı, İskele Mimarisi, Kompozit Kaplama, Jelatin Metakrilat

To my parents

ACKNOWLEDGMENTS

I am using this opportunity to express my gratitude to everyone who supported me throughout the research. Firstly, I would like to express my appreciation to my thesis supervisor Prof. Dr. Dilek Keskin for her encouragements, aspiring guidance and patience. My deepest gratitude goes to my co-supervisor Dr. Menekşe Ermiş Şen, for her invaluable guidance, friendly advice, patience and for always believing in me. Without her continuous support, this study would not be completed.

Albeit not directly involved in this study, Prof. Dr. Vasıf Hasırcı has been an inspiring figure for me, and I am truly thankful for his kindness and motivation.

I would like to thank the Center of Excellence in Biomaterials and Tissue Engineering (BIOMATEN) for allowing me to conduct my experimental studies with ease and all the necessary support along the way.

I am thankful for the support of Dr. Senem Heper Büyüksungur, Dilara Göksu Tamay, Ahmet Engin Pazarçeviren, Hossein Jodati, Bahadır Güner, and Çağdaş Ermiş.

I am grateful to my family for their encouragements, emotional and financial support. Without their everlasting love and support this would not be possible.

Lastly, I am really thankful to my husband Duarte Magalhães for his emotional support, friendly advice and making my life beautiful, lively and meaningful.

TABLE OF CONTENTS

LIST OF TABLES

TABLES

LIST OF FIGURES

FIGURES

LIST OF ABBREVIATIONS

3D	Three-Dimensional
ABS	Acrylonitrile Butadiene Styrene
ADSCs	Adipose-derived Stem Cells
Al	Aluminum
ALP	Alkaline Phosphatase
AM	Additive Manufacturing
BCP	Biphasic calcium phosphate
BG	Bioactive glass (Bioglass)
BM-MSCs	Bone Marrow-derived Mesenchymal Stem Cells
BMP	Bone Morphogenetic Protein
BMP	Bone Morphogenetic Proteins
BTE	Bone Tissue Engineering
Ca	Calcium
CAD	Computer-Aided Design
CB	Carbonate-Bicarbonate buffer
CLSM	Confocal Laser Scanning Microscopy
CP	Calcium phosphate
CPC	Calcium phosphate ceramics
DAPI	4',6-diaminO-2-phenylindole dihydrochloride

DMEM	Dulbecco's Modified Eagle Medium
DPSCs	Dental Pulp Stem Cells
DSC	Differential Scanning Calorimetry
ECM	Extracellular Matrix
EDS	Energy Dispersive Spectroscopy
EPC	Endothelial Progenitor Cell
ESCs	Embryonic Stem Cell
FDA	Food and Drug Administration
FDM	Fused Deposition Modelling
FGF	Fibroblast Growth Factors
FTIR-ATR	Fourier Transform Infrared-Attenuated Total Reflectance
GelMA	Gelatin Metharyloyl
HA	Hydroxyapatite
HCA	Hydroxycarbonate apatite
hFOB	human Fetal Osteoblast
HIPS	High Impact Polystyrene
ICC	Immunocytochemistry
ICP-OES	Inductively Coupled Plasma Optical Emission Spectrometer
IGF	Insulin-like Growth Factors
Li	Lithium
MDSCs	Muscle-derived Stem Cells
Mg	Magnesium

MMP	Matrix Metalloproteinase
MSC	Mesenchymal Stem Cell
Na	Sodium
NP	Nanoparticle
P	Phosphorous
PB	Phosphate Buffer
PBS	Phosphatase Bovine Serum
PCL	Polycaprolactone
PDGF	Platelet-Derived Growth Factor
PDMS	Polydimethylsiloxane
PEEK	Polyether Ether Ketone
PEM	Polyelectrolyte multilayer
Pen/Strep	Penicillin/Streptomycin
PETG	Polyethylene Eerephthalate Glycol-modified
PFA	Paraformaldehyde
PGA	Polyglycolic Acid
PHA	Polyhydroxyalkanoate
PHBV	Poly (3-hydroxybutyrate-co-3 hydroxyvalerate)
PIPES	Piperazine-N, N'-Bis (ethanesulfonic acid)
PLA	Polylactic Acid
PLGA	Poly (lactic-co-glycolic acid)

PLLA	Poly-L-lactic acid
PMMA	Polymethylmethacrylate
RGD	Arginine, Glycine, Aspartic Acid
RP	Rapid Prototyping
SBF	Simulated Body Fluid
SD	Standard Deviation
SEM	Scanning Electron Microscope
SLA	Stereolithography
SLS	Selective Laser Sintering
STL	Standard Triangulate Language
TCP	Tricalcium phosphate
TCPS	Tissue Culture Polystyrene
TE	Tissue Engineering
TE	Tris-EDTA
TEM	Transmission Electron Microscopy
TEOS	Tetraethyl Orthosilicate
TEP	Triethyl Phosphate
TGF-β	Transforming Growth Factor Beta
TIPS	Thermally Induced Phase Separation
TPU	Thermoplastic Polyurethane
UCB-MSCs	Umbilical Cord Blood-derived Mesenchymal Stem Cells
UV	Ultraviolet

v/v	Volume/volume
VEGF	Vascular Endothelial Growth Factor
w	Weight
w/v	Weight/volume
XRD	X-ray Diffraction
β-Gly	β-Glycerophosphate

CHAPTER 1

INTRODUCTION

This study combines the engineering aspects of mechanical design and manufacturing practices with biomaterials knowledge to obtain a novel bone scaffold. Computer-Aided Design (CAD) and Fused Deposition Modeling (FDM) methods are great candidates for modeling and producing scaffolds with controlled geometry. CAD allows precise modeling of the desired designs, and both size and geometry can be controlled to the point. In 3D printing, CAD models can be produced without conventional methods such as injection molding. These methods allow one-of-a-kind production of 3D structures if desired (without the need for mold production) and replicating products with high fidelity.

A brief definition of tissue engineering, some of the materials and production methods used in tissue engineering will be described in this chapter.

1.1 Bone

As we known as bone or osseous tissue makes up to 14% of our total body weight. It gives strength to the body, protects the organs such as the brain and heart, produces blood cells, regulates hemostasis, forms the body's shape, and supports moving, sitting, lying down, and many other activities. Tissues are two types, hard tissues and soft tissues. Bone is classified as hard connective tissue, which is composed up of organic matrix about 20-30 w/w% (mainly collagen type I over 90 w/w%) and inorganic or mineral matrix (hydroxyapatite crystals with the composition of $Ca_{10}(PO_4)_6(OH)_2$) roughly 60-70 w/w% and water 10 w/w%. The organic matrix

1

maintains the toughness, whereas the inorganic matrix contributes to the stiffness of the bone [1].

Bones, in general, are characterized as short, long, flat sesamoid, and irregular types (Figure 1.1), but they structurally are 2 main types as compact (cortical) and trabecular (cancellous, or spongy) bone. The compact bone is the outer shell of the bone, which is hard and dense with a porosity of about 10%, while the cancellous bone is the inner layer that is highly porous with interconnected pores. Spongy bone is more elastic than compact bone, so Young's modulus (E) of spongy bone is 10-900 MPa, while the elastic modulus of the cortical bone is around 350 GPa.

Figure 1.2 shows the bone structure from macro to nano level. Bone comprises 4 types of cells: osteoblasts, osteoclasts, osteocytes, and bone lining cells. Osteoblasts are responsible for new bone formation and organic matrix synthesis during ossification in a simple description. The organic matrix includes collagenous matrix and matrix proteins (osteopontin, osteocalcin, and bone sialoproteins). New bone formed by osteoblasts is initially amorphous calcium phosphate (CaP). During mineralization, amorphous CaP turns to crystallized hydroxyapatites.

On the other hand, osteoclasts are responsible for breaking down the bone and resorption minerals in the osteolysis process. These 2 types are involved in a dynamic process, and the equilibrium between their functions is critical for bone regeneration and structural integrity [2]. Osteocytes are the immature osteoblasts that maintain the communication inside the bone, and finally, bone lining cells are involved in regulating the calcium passage into and from the bone. Bone remodeling and function bone cells are represented in Figure 1.3.

Bone defects due to diseases, aging, infections, accidents, and congenital reasons are the problems of today's world. Over 10 million bone fractures happen in the United States annually and about 2.2 million people all over the world need bone implants [3]. Bone is a regenerative tissue capable of healing itself. However, this healing process cannot be done via body alone in the case of large defects.
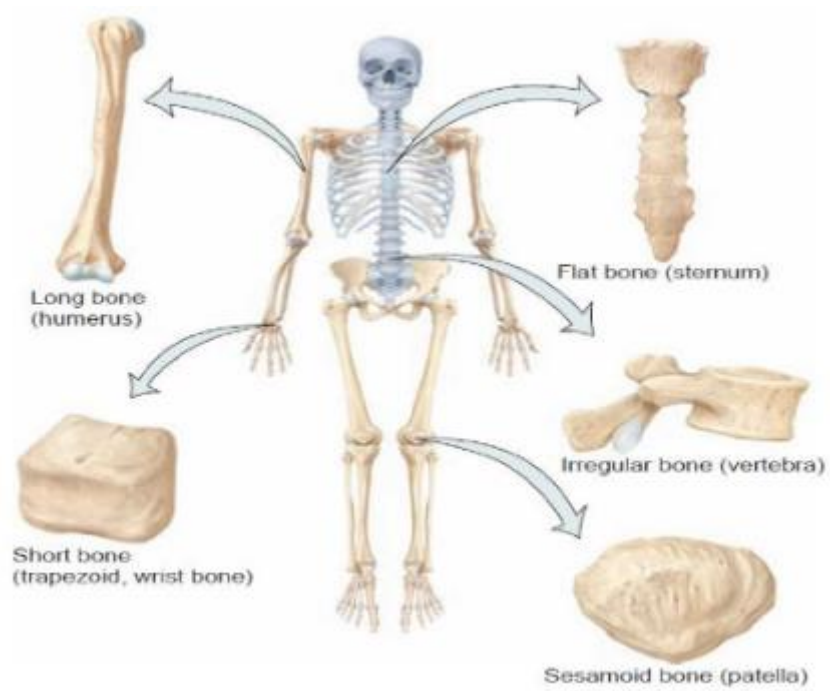
Figure 1.1. 5 types of bone. Taken from [4].
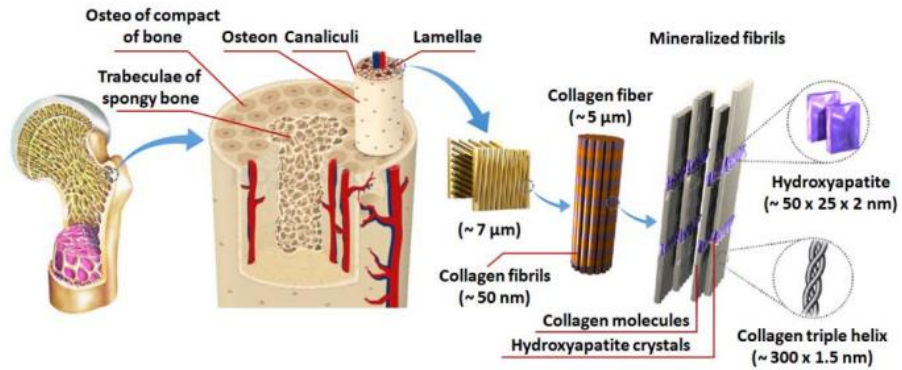
Figure 1.2. Schematic illustration of bone structure from macro to nano level. Taken from [5].
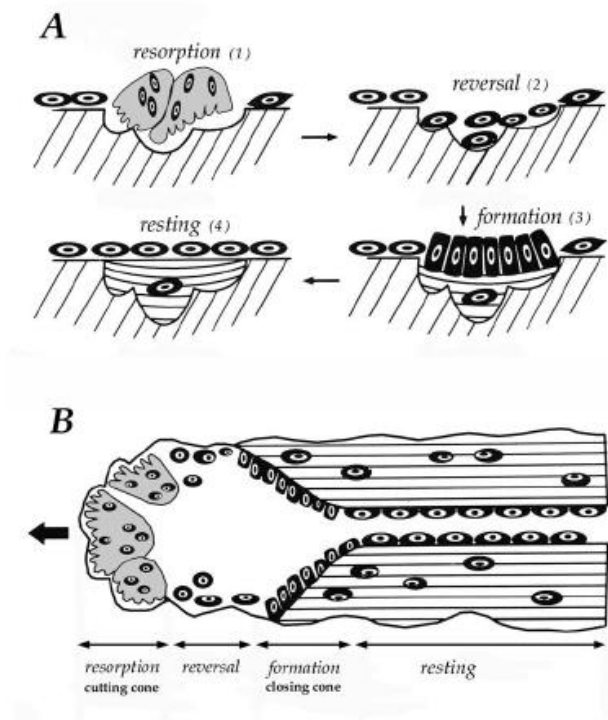
Figure 1.3. Schematic representative of cancellous bone remodeling. The first phase (1) shows resorption process activated by osteoclasts (gray shaded). In the second phase (2), osteoclasts die during apoptosis or migrate to the other sites. Then, mononuclear cells invade, and (3) Osteoblasts (black shaded) make a new bone matrix with the different collagen fiber orientation. In the last step, bone formation ceases, and the surface turns to a resting state. B represents the remodeling sequences in compact bone with the same phases as trabecular bone. The difference is osteoclasts dig the tunnel with 0.1mm diameter and 2mm length. After reversal and bone formation phases, resting osteoblasts are lined with blood vessels in the center of the channel. Taken from [6].

1.2   Tissue Engineering

Tissue loss is a problem of modern medicine, and there are several alternatives with advantages and disadvantages. Depending on the type of tissue, if the physical size of the defect (critical size) is suitable. The human body can regenerate if the soluble factors (hormones, peptides, etc.) for differentiation. When the physical damage is beyond the critical limit, new tissue is needed for repairing the defect [7]. Considering all risks associated with allografts and autografts (immune rejection, infection, transmission of pathogens, scarcity of donor tissue, donor site morbidity, surgery, and shortage of donor), tissue engineering (TE) is a promising approach that aims to provide methods to repair and regenerate the tissues with risks less than former methods [8]. Langer, and Vacanti first proposed the tissue engineering phrase in 1993. They described this term as "an interdisciplinary area that combines life sciences and engineering principles and mainly aimed regeneration and/or repair of organ loss and tissue damage caused by diseases, injuries, aging and trauma" [9]. TE utilizes the combination of biomaterials (scaffolds), cells, bio-factors (like Growth factors), and engineering methods to replace the injured tissues, restore and improve their function [8]. Growth factors provide cell adhesion, migration, differentiation, proliferation, and vascularization [10]. Tissue engineering, and mainly the purpose of this study, bone tissue engineering, is a growing field of research [8]. Figure 1.4 shows the schematic representation of the tissue engineering procedure.
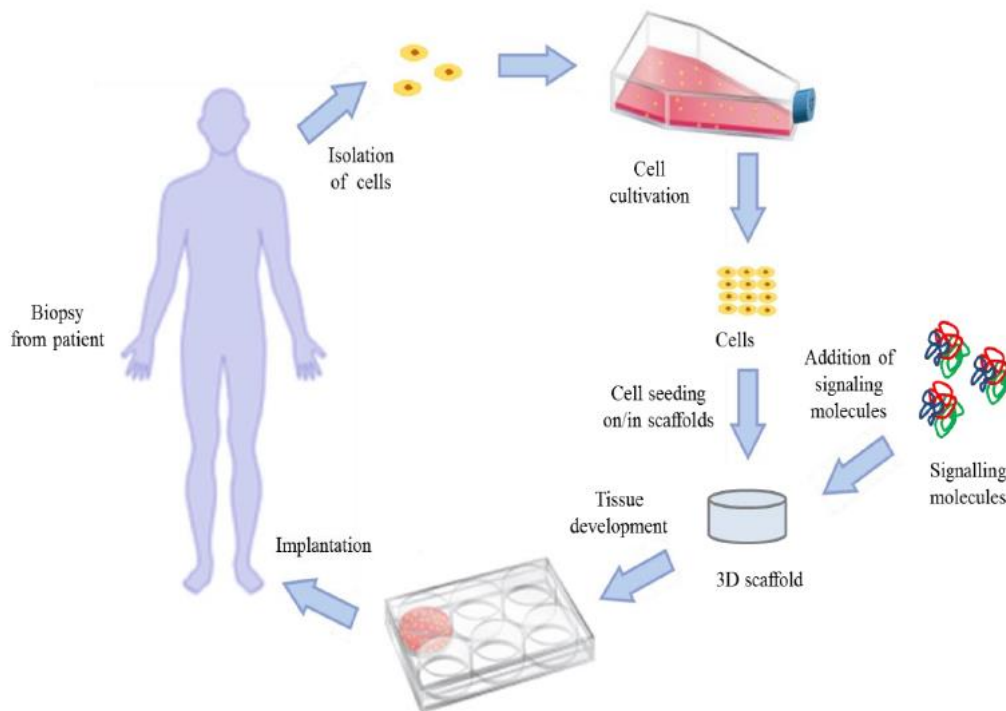
Figure 1.4. Tissue engineering procedure. Taken from [3].

1.3 Bone Tissue Engineering

Bone defects have caused critical issues in the world. As previously mentioned, these defects can result from infection, diseases, tumors, aging, etc. Autologous grafts, allogeneic grafts, or artificial bone are three main approaches to repair large-sized bone defects that require implants. Apart from donor site surgery, the first two approaches increase the risks of pathogen transmission. So, artificial implants seem to be suitable replacements despite the limited biocompatibility, biodegradability, and mechanical compliance. Bone tissue engineering (BTE) or simply bone scaffolds are the safest solutions with the least challenges faced to restore and maintain bone functions. BTE aims ,to find the best biomimetic replacement for bone in terms of structure, composition, and performance by applying biology, chemistry, and engineering principles [8].

Bone tissue engineering is a combination of some elements and factors. These components are primary cells, 3D cell carriers, so-called scaffolds, and bio-factors or growth factors [11].

Cells can be obtained from different sources such as allogenic, autogenic, and xenogeneic sources, and stem cells. Cells should be osteogenic, non-tumorigenic, and non-immunogenic [12]. The widely used cells for BTE are, human mesenchymal stem cells [13]–[15], and human fetal osteoblasts [16]–[18]. Adipose-derived stem cells (ASCs) [19] and periosteal cells [20] are the second widely cultured cells in the bone regeneration field. It has been reported that adipose stem cells have superior proliferation, differentiation, angiogenic and osteogenic natures than bone marrow cells in vivo [19].

Growth factors are polypeptides secreted by cells. As it is mentioned before, cytokines have various functions like initiation or inhibition of cell migration, adhesion, proliferation, and differentiation [21]. Some growth factors are applied to stimulate bone formation in BTE are insulin-like growth factors I [22], bone morphogenetic proteins (BMP-2 and BMP-7) [23], platelet-derived growth factor (PDGF) [24], fibroblast growth factors (FGF) [25], transforming growth factor β (TGF-β) [26], and vascular endothelial growth factor (VEGF) [27].

Other than growth factors, some small soluble molecules were also used as osteogenic differentiation factors or osteogenic supplements. Ascorbic acid, dexamethasone, and β-glycerophosphate are among the widely used ones. Cells use ascorbic acid as a cofactor and hydroxylate the proline and lysine residues in collagens found in the ECM. Ascorbic acid promotes collagen type I synthesis, which leads to integrin signaling. These events are conjugated with Runx-2 directed osteogenic differentiation. Dexamethasone is a synthetic glucocorticoid that enhances osteogenic differentiation through a cascade of events. It activates Runx-2 dependent transcriptional regulation [28]. Dexamethasone elevates the ALP and OC mRNA and protein levels and induce osteoblastogenesis [29]. For dystrophic matrix mineralization, β-glycerophosphate (β-Gly) which is an inorganic phosphate comes into play [28].

Scaffolds are integral part of BTE that supports tissue development and stimulates cell attachment and proliferation [30]. Scaffold microstructure such as porosity, particularly interconnected porosity and pore size, osteoconductivity, osteoinductivity, biodegradability, and biocompatibility play an important role in cell viability and tissue development [31], [32]. Two critical elements involved in scaffold application are selection of a biomaterial and fabrication technique [7]. Biomaterials can be metals, ceramics, synthetic or natural polymers, and composite materials. The manufacturing techniques for the fabrication of scaffolds can be classified into conventional (e.g., solvent-casting, gas foaming [33], sol-gel technique, freeze-drying [34]) and advanced techniques as electrospinning [17], and 3D printing or rapid prototyping (RP) (e.g., stereolithography, fussed deposition modeling (FDM), selective laser sintering (SLS) and bioprinting) [35]. Ideal scaffold resembles bone in mechanical and chemical properties, mimics bone ECM biochemistry, and allows tissue growth in high need. All these features for scaffold material selection and manufacturing process can be categorized in Figure 1.5. Achieving all the features and desired outcomes is not convenient.
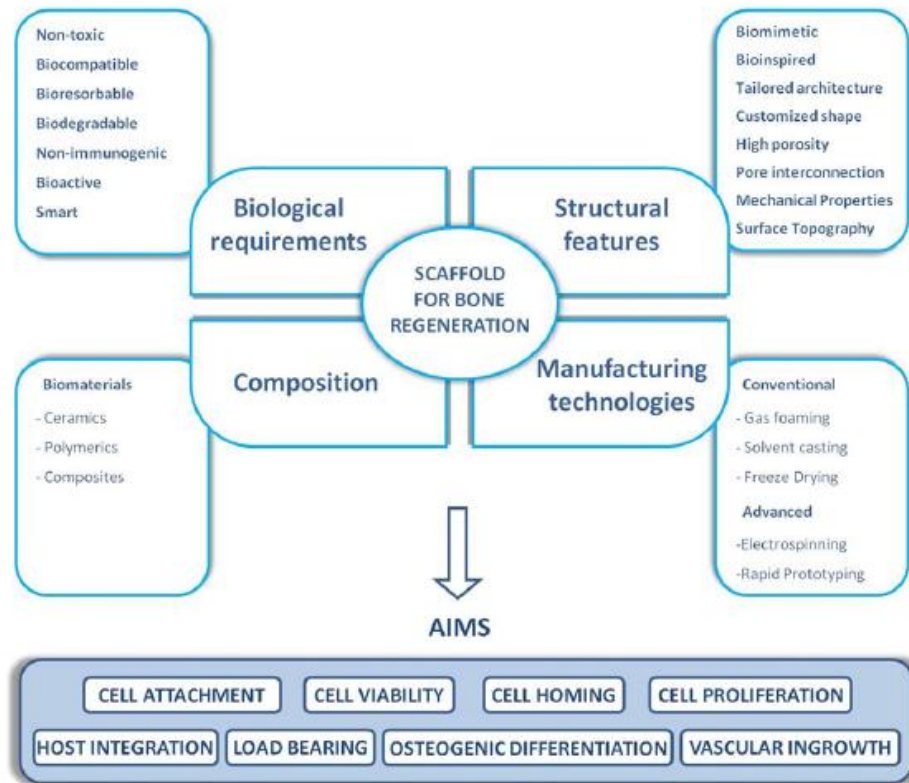
Figure 1.5. Ideal bone scaffold biological and structural requirements, compositions, and manufacturing techniques. Taken from [35].

1.3.1 Materials Used in Scaffold Production

Materials used for the fabrication of cell carriers are polymers, ceramics, and composites of polymer-ceramics. Polymers can be classified as natural and synthetic one. In this section, these biomaterial categories will be described in detail.

1.3.1.1 Natural Polymers

Some natural polymers used in the literature are collagen, silk fibroin, chitosan, alginate, Polyhydroxyalkanoates (PHAs), gelatin, etc. Natural polymers are from plant or animal resources and are known for cost-efficient production, biocompatibility, biodegradability, and low toxicity [36]. Despite all these benefits,

they lack good mechanical properties. They show high degradation rate, immune rejection, and pathogen transmission [37]. Some studies in the literature have demonstrated the use of natural polymers combined with ceramics or synthetic polymers to improve their properties [38]. Collagen, gelatin, silk fibroin, chitosan and alginate are some of the widely used natural polymers.

1.3.1.1.1   Collagen

Collagen is originally a Greek word meaning glue. It is a structural protein found in the ECM of connective tissues like bone, cartilage, skin, tendons, and ligaments [39]. It is also found in blood vessels and cornea. It has a helical structure made of fibrils. Figure 1.6 shows the collagen structure in detail. Up to 35% of proteins found in the body are collagen. Collagen is created mainly by fibroblast cells [40]. Collagens are divided into different types according to their structures [41]. The most common types are type I, II, III, IV, and V [42]. Type I has a fibrillar structure and can be found in skin, tendon, bone, etc. Type I collagen is the only collagen type found in the organic matrix of the bone and constitutes 90% of the collagen found in the body [43]. Collagen provides structural support by attaching to the integrin receptors of the cells [44].

Although it has poor mechanical properties, a combination of collagen with other polymers and ceramics overcomes this drawback. Biodegradability and low antigenicity are some benefits of collagen. Collagen can be used as reinforcement for ceramics and synthetic polymers for BTE purposes since it mimics the organic component of the bone. Several studies proved that collagen stimulates osteogenesis [45], [46]. Collagen has some medical applications such as cardiac applications [47], cosmetics [48], bone grafts, wound healing [49], etc. Collagen can be applied as injectable hydrogel [50], membranes, and films [51], sponges and scaffolds [52], or micro-nano spheres [53].
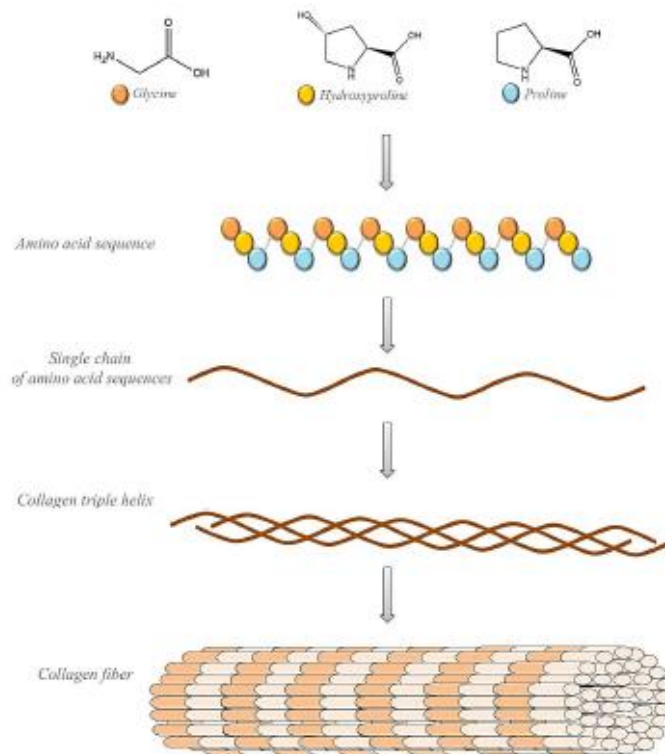
Figure 1.6. Collagen structure. Glycine, hydroxyproline and proline make amino acid sequences and single strand. Single chains form triple-strand helical structure of collagen and finally a group of helices makes a collagen fiber. Taken from [54].

1.3.1.1.2 Gelatin

Gelatin is a denatured derivative of collagen produced during hydrolysis of collagen and is the most abundant protein in the body. Gelatin can be extracted from collagen found in tendons, bones, cartilage, etc. [55]. It is biocompatible due to low cytotoxicity, biodegradable, low immunogenic and low-cost protein, and arginine-glycine-aspartic acid (RGD) and matrix metalloproteinase (MMP) amino acid motifs, it has received significant attention. RGD facilitates cell adhesion, and proliferation and MMP enhance cell remodeling [56]. In addition, it is more soluble in aqueous media compared to collagen. These benefits turn gelatin into a good candidate for TE and especially BTE. Figure 1.7 shows the chemical structure of the gelatin. The most important critiques are poor mechanical properties and fast

11

degradation. These properties can be overcome by cross-linking. Some cross-linkers are applied in the literature to enhance the gelatin's biological and mechanical properties. Cross-linking of gelatin with glutaraldehyde [57], with 1-ethyl-3- (3-dimethyl aminopropyl) carbodiimide (EDC) [58], and N-hydroxysuccinimide (NHS) used with EDC [59] are some of them presented in the literature.

Ren et al. has illustrated the in vitro bioactivity of gelatin and siloxane hybrid scaffolds and osteoblast cells differentiation [60].
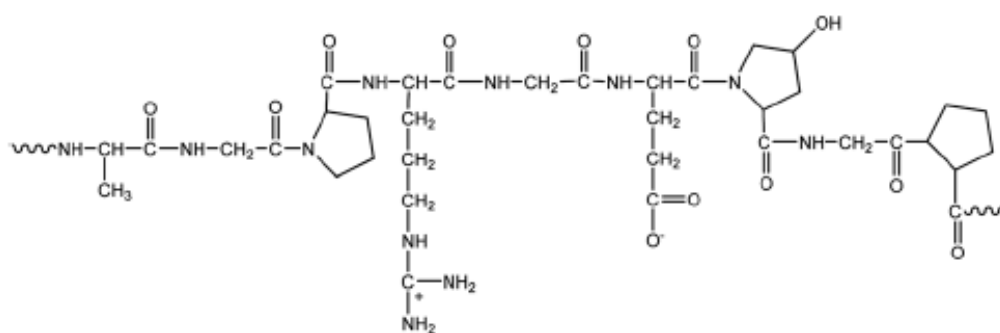
Figure 1.7. Structure of Gelatin. Taken from [61].

GelMA hydrogel was introduced by Van Den Bulcke et al., in 2000 [62]. Modifying gelatin with methacrylic anhydride and adding unsaturated bonds to the gelatin is another method to improve mechanical properties and control degradation rate. In this process, gelatin turns to gelatin methacryloyl, so-called GelMA. GelMA can crosslink under the ultraviolet (UV) light [63]. However, this UV light has an adverse effect on cell viability [64]. Figure 1.8 represents the GelMA synthesis by adding methacrylic anhydride at $50°C$ to the gelatin (A) and making hydrogel of GelMA under UV light (B). The concentration of methacrylic anhydride is usually less than 5 v/v%, so the RGD and MMP sequences are affected during methacrylation [56].
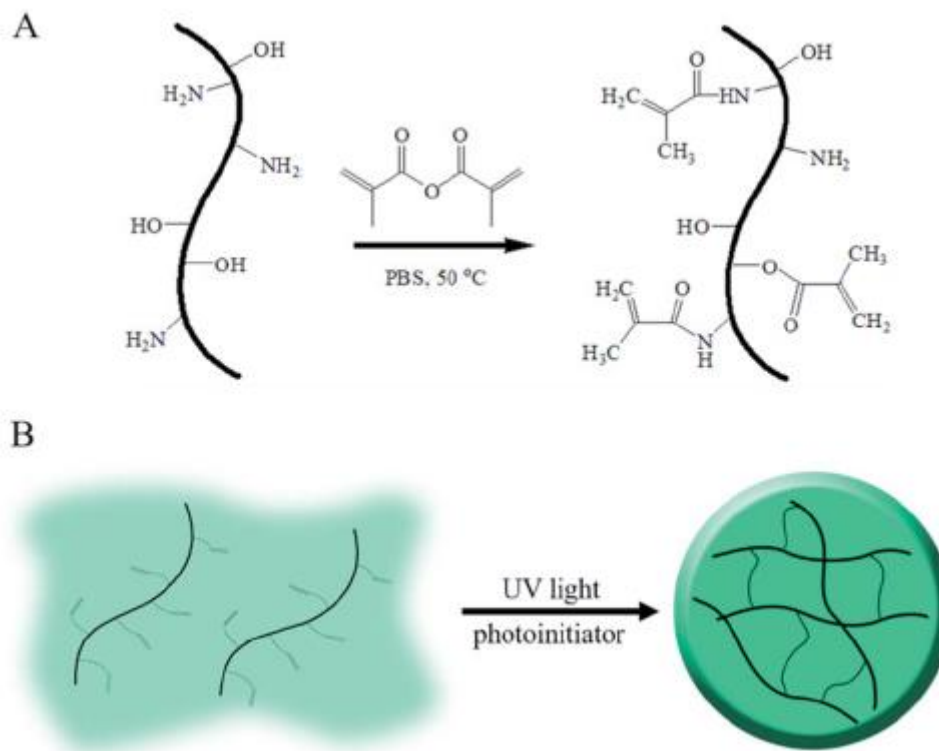
Figure 1.8. Schematic synthesis of GelMA and its hydrogel. Taken from [63].

Various elements can modify the mechanical properties of the GelMA. These factors are the concentration of GelMA [65], concentration of photo-initiator, polymerization method [66], UV intensity and duration, and crosslinking conditions [67]. It was shown by Lee et al. that the concentration of the GelMA inversely affects the pore size [68]. GelMA based materials are used frequently in biomedical applications, tissue engineering, drug delivery, and bone regeneration studies. GelMA with growth factors, other natural and synthetic polymers [69], and also inorganic materials like bioceramics [69], [70] in a composite form can provide promising results in the case of bone tissue engineering and bone regenerations. Composites of GelMA with natural polymers greatly impact mechanical properties [71]. Blending GelMA and type I collagen resulted in higher stiffness of the scaffold and enhanced viability of HUVEC [72]. Composites of GelMA with alginate have a positive influence on mechanical properties and cell adhesion and proliferation of

fibroblasts [73]. GelMA combined with PLA polymer is a widely used approach in scaffold production. 3D printed PLA scaffolds combined with GelMA as an encapsulation matrix for RGNP (cyclic RGD conjugated with gold nanoparticles) was the purpose of a study presented by Heo et al. [74].

1.3.1.2   Synthetic Polymers

Synthetic polymers have a significant role in TE and regenerative medicine. These polymers have better mechanical properties and processing flexibility than natural polymers [75]. They are biocompatible, biodegradable, and most important, the degradation rate can be adjusted according to the application [76]. Unlike natural polymers, synthetic polymers allow mechanical integrity to remain sufficient time; therefore, the polymer can be replaced by cell cell-secreted ECM, which leads to a new tissue formation [77]. Moreover, they do not have the concerns associated with natural polymers like pathogen transmission and immunogenicity [75]. The vast majority of synthetic polymers frequently used in the TE field, which are U.S.A. Food and Drug Administration (FDA) licensed belong to the polyester family [78]. Two main categories of the polyester family are polyglycolide and polylactides. Polylactic acid (PLA), polyglycolic acid (PGA) and their copolymers, poly (lactic-co-glycolic acid) (PLGA), and poly-L-lactic acid (PLLA) are examples of this family. Polycaprolactone (PCL) is also a widely applied biopolymer in the biomedical field. Synthetic polymers have medical applications such as wound dressing, degradable sutures, stents. [79].

1.3.1.2.1   Polylactic Acid

PLA is a thermoplastic aliphatic polyester. It is a recyclable and compostable eco-friendly biopolymer. Its backbone formula is $(C_3H_4O_2)_n$ or $[-C(CH_3)HC(=O)O-]_n$ and its structure is shown in Figure 1.9. It was firstly synthesized by Carothers (at DuPont) in 1932 [80]. PLA building block or monomer can be derived

14

from the fermentation of starch in the potato, corn, sugarcane, etc. [81]. Lactide has L- and D- lactide isomers [82]. It is a widely applied synthetic polymers as ink for 3D printing. It has low toxicity, biosafe, biocompatible and low cost. However, its side effects by implantation have been reported in the literature [83]. It has good mechanical properties as a synthetic polymer, but it is brittle and has lower compressive strength than natural bone. Therefore, its composites with ceramics got extensive amount of attention since ceramics can improve the mechanical properties and mineralization [84].

PLA has medical applications as a pin, rod, screw, washers, darts, and orthopedic scaffolds [85]. Its degradation product, lactic acid, can be found naturally in the body, and it can be removed by the tricarboxylic acid cycle; therefore, they do not accumulate in organs [86]. PLA is highly hydrophobic. However,, its hydrophilicity and wettability can be enhanced [87].

PLA and PGA are structurally similar, while their chemical and features are different due to the methyl group on the alpha carbon of the PLA [88]. PLLA is a polymer of L-lactide, which is a lactide isomer. In terms of mechanical features, PLA has higher properties than its copolymers PLLA and PDLA. PLLA is a biodegradable polymer and has been utilized mainly in degradable sutures, orthopedic and soft tissue implants, and facial fillers in volume loss [89]. In addition, PLLA stimulates collagen synthesis [90].

In vitro degradation of PLA was investigated with two different methods: first PLA is placed in phosphate buffer saline (PBS) [91]. Second, it was degraded enzymatically by enzymes, e.g., proteinase k [92].

PLA is commonly used as blend form, combined frequently with HA [93]–[96], with PCL [97], HA/PCL [98] and PEG/G5 [99] as ink for 3D printing. PLA/nHA filaments were produced by melt extrusion, to feed into a 3D printer. The results showed the final scaffold is cytocompatibile, cells were proliferated and spread properly on the surface, and nHA particles improved the adhesion of the cells [100].
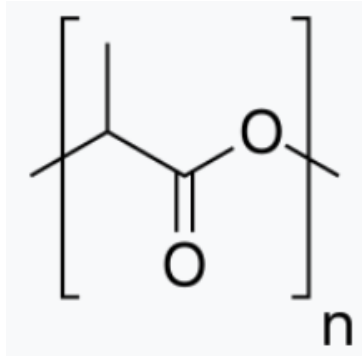
Figure 1.9. Chemical structure of polylactic acid.

1.3.1.3   Bioceramics

Ceramic materials are widely applied to repair and reconstruct the damage, failure, and disease [101]. These materials are known for high melting temperature, low electrical conductivity, hard refraction, resistance to corrosion, and crystallinity characteristics [102], [103]. In addition, ceramics were used in various hard tissue applications in the literature such as dental, missile ear, cranial, spinal, maxillofacial, and bone tissue engineering [104].

Bioceramics can be classified into two main classes as bioinert and bioactive ceramics. Bioinert materials are used as the hip joint femoral head. Two generally bioinert ceramics are alumina (Al_2O_3) and zirconia (ZrO_2).

The second group is bioactive ceramics. The word bioactive refers to a feature where material establishes a strong bond with the native bone and interacts with it or responds to the tissue. The bioactive ceramics group includes calcium phosphates, bioactive glasses, aluminum oxides, carolline, etc. Bioactive glasses so-called bioglasses and calcium phosphates, are the commonly used bioactive ceramics. According to the Ca/P ratio and crystal phases calcium phosphate ceramics (CPC) are divided into different groups. Hydroxyapatites (HA), tricalcium phosphate (TCP), and biphasic calcium phosphate (BCP) can be categorized in the calcium phosphate group [105]. Calcium phosphates are highly biocompatible and owing to their osteoconductivity. They are similar to the bone mineral phase. They have

16

applications in the BTE area as scaffolds, fillers, coating, and composites [106]. However, their brittleness is a deterrent factor in CPC application in long bone repair, and load-carrying applications, and they are employed in bone regeneration cases instead.

Despite the similarity of HA ($Ca_{10}(PO_4)_6(OH)_2$) to the mineral phase of the bone is the least soluble formulation of the calcium phosphate, which restricts its bioactivity and has slower degradation [105]. HA in high concentration facilitates the scaffold's desired osteoconduction and osteointegration properties [107].

HA can be synthesized from various routes. Solid-state reactions, precipitation and coprecipitation, hydrolysis and solution mediated reactions, hydrothermal, emulsion and microemulsion techniques and sol-gel methods are these routes.

TCP is the second most common inorganic phase in the bone. It is highly soluble, and it has a lower Ca/P ratio with two crystalline phases (α-TCP and β-TCP). The dissolution rate of the β-TCP is less than the former one. TCP has poor mechanical resistance and high resorbability [108].

To overcome the limitations of HA and β-TCP, a new group of calcium phosphates called biphasic calcium phosphate (BCP), which is a combination of both, is developed. This material has better bone ingrowth and mechanical properties than its constituent components [109].

Ceramic contributions as coatings, fillers, or bases for scaffolds in combination with synthetic and natural polymers have been observed extensively in the literature since they can mimic the inorganic structure of the bone. PLA combined with ceramics is beneficial regarding improvement of compressive strength and Mineralization [84]. Ceramics combined with PLA such as HA [110], tricalcium phosphate [111] and bioglasses ([112]–[114]) resembling mineral portion of bone are often used in literature. Nano-hydroxyapatite (HA)/collagen/PLA composite scaffold was presented by Liao et al. They showed that increasing PLA in the composite improved the compressive strength [110].

The second and most important group of bioactive ceramics are bioactive glasses or bioglasses in short. Glasses are the materials based on silica which some of them can

be replaced by calcium (Ca), Phosphorus (P) or sodium (Na) [115]. Glass ceramic materials are the composites of glasses with Lithium/Aluminum (Li/Al) or Magnesium/Aluminum (Mg/Al) crystals. Bioglass shows excellent biocompatibility, bioactivity and biomineralization (more than hydroxyapatite) even though it does not have the same composition as bone mineral. Bioglasses in the specific formulation are osteoinductive and osteoconductive [116]. Bioglasses are categorized into different types according to various compositions and ratios of SiO_2, CaO, P_2O_5 and Na_2O [117]. This type of glasses can form HA crystals layer upon soaking in biological fluids like simulated body fluid (SBF) [105]. In body fluids or SBF, calcium and phosphate ions in glasses and other ions are also released. Na^+ in body fluid, leaches faster than PO_4^{3-}, Si^{4+} and Ca^{2+} and a silica rich layer shapes on the glass surface which consequently leads to calcium phosphate layer deposition on the glass surface [117]. This Ca-P layer is amorphous at the beginning by augmentation of Ca^{2+} ions, nucleation starts, and it crystalizes and forms Hydroxycarbonate apatite (HCA). Figure 1.10 shows the mechanism of HCA formation on bioglass. To summarize, apatite formation consists of 5 stages, 1) rapid ion exchange in the solution or leaching, 2) network dissolution or breaking bonds in the reaction, 3) polycondensation and forming a silica gel, 4) formation of an amorphous calcium phosphate layer, 5) crystallization and forming HA layer. Bioglasses are bioactive and create chemical bond between tissue and scaffold [118]. These glasses boost cell growth and surface roughness as well as angiogenesis and differentiation of them to bone cells. Therefore, bioglasses own osteoconductive and osteoinductive characteristics [119]–[121]. They are also capable of osseointegration which means, direct contact and bond between native bone and contact surface of the implant [122]. Because of their poor mechanical features and low fracture toughness, they cannot be employed in load bearing applications [123].
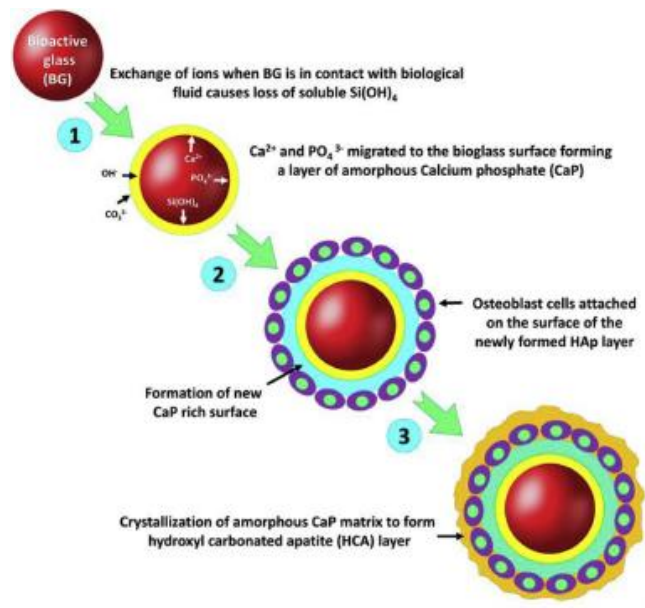
Figure 1.10. Schematic representation of HCA formation on the bioglass surface. Steps are described in the figure. Taken from [124].

Some of the most important and widely used bioglasses are summarized in the Table 1.1 [125]. Available commercial brands for bioactive glasses are also categorized in Table 1.2.

Table 1.1. Chemical compositions of the various types of bioglasses.

Bioglass	Composition (wt%)
58S (sol-gel method)	58% SiO_2, 38% CaO and 4% P_2O_5
45S5 (Bioglass®)	45% SiO_2, 24.5% Na_2O, 24.5% CaO and 6% P_2O_5
70S30C	70% SiO_2, 30% CaO
S53P4	53% SiO_2, 23% Na_2O, 20% CaO and 4% P_2O_5

Table 1.2. Some of the available commercial brands for bioactive glasses and their applications [126], [127].

Brand	Application Area
Bioglass® 45S5	Bone graft substite
Bio-Oss®	Dental bone graft
Cerabone®	Dental bone graft
UltraDEX®	Dentin treatment and repair
NovaMin®	Dental remineralization
Bioverit® I & II	Bone substitution (head & neck surgery)
NovaBone-C/M®	Bone graft substitute (orthopedic & facial reconstruction)

Bioglass® 45S5 was the first bioglass synthesized in 1969 by Dr. Hench at the University of Florida. Bioglasses were synthesized in micro then nano-size [128]. Yet, either micron or nano has clinical applications. Decreasing the size of the particles has a positive effect on their reactivity through prompt releasing of the ions and superior adsorption of the proteins from the BG surface. Nano size bioglass particles have applications in bone tissue engineering and implants, dental applications, drug delivery, soft tissue regeneration, wound healing, etc. [129], [130]. Barbeck et al., proposed a bi-layered bone substitute (combination of PLA and PLA/bioglass G5) [112]. They showed that G5 bioactive glass has reduced weight loss and led to high mechanical strength and vascularization. In another study, the PLA and PLA/BG 20% and PLA/BG 40% were produced and seeded with endothelial progenitor cells (EPC) and mesenchymal stem cells (MSC) [113]. In this study, Eldesoqi et al., claimed that the ultimate load of scaffolds has a direct relation with bioglass content. Composite scaffolds were generated by Eqtesadi et al. [114] by infiltration of PLA into bioglass 45S5 scaffolds in 2 ways: impregnation by immersion in molten PLA and coating in the solution of the PLA. PLA coating

showed higher strength. 2 years after this study, Motealleh et al. [131] investigated mechanical strength, degradation rate, and bioactivity of 45S5 BG scaffolds with different coatings. In this study, BG scaffolds were dip-coated with natural polymers such as alginate, chitosan, and gelatin and synthetic polymers as PLA, PCL, and polycaprolactone. It was demonstrated that natural polymers introduced greater reinforcement, apatite formation and bioactivity. Poly-D,L-lactide (PDLLA) and ploy(lactide-co-glycolide) (PLGA)-45S5 bioglass (10, 25,50 wt%) composite porous scaffolds were produced by freeze-drying technique. It was shown that the addition of BG has delayed the degradation rate and enhanced the degradation rate [132].

1.3.1.3.1 Bioactive Glass Synthesis Techniques

Bioactive glasses can be synthesized by a variety of methods. Traditional melting and sol-gel methods are the most common ones.

In the melting method, SiO_2 from soil source, Na_2O and CaO from carbonated sources and P_2O_5 in an oxide, form is melted in a Pt-Rh pot at 1350˚C-1400˚C. Subsequently, the melt is homogenized and poured into a mold. The bioglasses synthesized by this method are in the micro range in size, dense and do not contain organic components or water. The standard well known bioglass is 45S5 and is synthesized by this method at a temperature between 1300˚C-1500˚C. Upon modification of 45S5 BG, SiO_2 is modified while, P_2O_5 the compound does not change. Maintaining silica ratio less than 60% and high CaO/P_2O_5 During the synthesis, the critical factors in preserving the material surface reactive [133].

Sol-gel is another ordinary technique. Unlike the conventional melting method, the procedure takes place at room temperature in the sol-gel method. Hence, it is termed the cold method as well. The precursors in this method are usually metal salts and metal alkoxides. This procedure usually includes the following phases in order, a) dissolution of the precursors, b) condensation to form colloidal sol, c) gelation, d) aging, e) drying of gel, and f) calcination at high temperature (600˚C-700˚C). In the last step, the gel is transformed to bioglass at high temperature using furnace [129].

The unwanted organic compounds from hydrolysis and condensation steps are eliminated in the drying phase. The calcination step results in stability and bioactivity. Generally, calcination occurs at 600˚C, which is the least temperature that satisfies the stability and maximum bioactivity [134], [135]. The most well-known bioglass that can be synthesized through this method are 58S and 45S5 bioglass. Sol-gel method has advantages over the conventional melting method. This technique presents larger surface area, higher microporosity, purity and homogeneity in the final product compared to melting method [136].

The sol-gel method can be mediated via an alkali compound to accelerate the gelation process. In the quick alkali mediated sol-gel method, the alkali component, which is a base like ammonia (NH_3) (soluble in water) is added to the reaction, leading to rapid gelation and saving reaction time. Nonetheless, high gelation and precipitation rate may cause some deviations from the nominal composition. Ammonia concentration is inversely proportional to the gelation time and directly proportional to particle size [130]. The particles obtained from the alkali mediated method are generally less than the traditional sol-gel method. In the conventional method particles are usually in the micron range (bigger than 1 micron), whereas, in alkali mediated process, they are in the nano range.

The sol-gel method can be combined with other technologies. As an example, it can be combined with the coprecipitation method. In this technique, the precursors are hydrolyzed in an acidic environment, condensed to a gel, and precipitated in an alkaline solution. Lyophilization impedes the agglomeration of the gel during the drying. This procedure is followed by calcination. The high synthesis temperature improves the crystallinity quality. Well dispersed particles can be achieved as a product of this method without grinding and sieving. It is a low-cost production, and the resultant nanoparticles can be utilized for BTE scaffold and nanocomposite preparation [137].

1.3.2   Scaffold Design

Previously mechanical properties, biodegradability, and biocompatibility were discussed in biomaterial selection for the scaffolds. Another important feature for the bone scaffolds is the design of the scaffold or morphology, which effects the mechanical strength, osteogenic differentiation, permeability, nutrient diffusion, cellular responses and proliferation, bioactivity, vascularization [138], [139]. Some of the parameters which should be considered in scaffold architecture are total porosity, interconnective porosity, and pore size. Porosity, the interconnectivity of the pores, and pore size altogether form the scaffold shape. Cancellous bone is known for its interconnected porous structure. Scaffolds mimicking this type of bone should mimic its morphology as well.

Although porosity is an essential factor in cell migration and tissue formation, it drastically reduces the mechanical strength of the scaffold [107]. Reaching the optimal porosity of the scaffold with maximum mechanical properties, which governs the cell ingrowth and osteogenesis, is a huge challenge in the bone scaffold design area.

Interconnective porosity or open porosity is defined as "the ratio of the void space, which is accessible, to the bulk volume". It is a key factor in BTE and more critical than the porosity. In this type of porosity, pores are connected to each other, facilitating cell colonization and tissue formation [140].

Pores can be made in different ways using porogens like paraffin [138], foam-gel, freeze-drying, thermally induced phase separation, chemical or gas foaming, solvent casting and particle or salt leaching [141]. In these methods, pores of different sizes can be obtained. There are three types of macro, micro and nano size pores. Pore diameters more than 100 μm are called Macropores, in the range of 0.1-10 μm are micropores and less than 0.1 μm are called nanopores. Macropores facilitate cell ingrowth and vascularization. Micropores result in surface roughness which later mediates cell attachment [142] and finally, nanopores elevate the specific surface area that leads to enhanced bioactivity and protein adsorption [143], [144]. A

minimum pore size range for osteogenesis is 100-150 μm. An enhanced vascularization level and osteogenesis pores larger than 300 μm are required [141]. It was reported that the squared pores and triangular pores influence the morphology of the macrophage and the expression of cytokine [121].

Computer-aided designs allow us to achieve controlled interconnective porosity and pore size by customizing scaffolds designs [145], [146]. A large number of regular geometries using different CAD tools have been developed for BTE scaffolds and produced in 3D printing process [91], [147], [148].

There are also some complex designs which are theoretically proposed for bone tissue engineering applications and 3D printed but not utilized as a scaffold [149]–[152]. Among these, Gomez et al. [149], Herath et al. [150], and Chen et al. [151], proposed an irregular Voronoi tessellation method that highly mimics the bone's porous structure. It was proposed that the final properties of the product can be altered during the design step to match the trabecular bone properties such as total porosity and microstructural features. This structure favors cell adhesion, proliferation and osteoconduction. Voronoi tessellation (Figure 1.11 and 1.12) drove huge attention in many disciplines due to its abundance in nature and interesting mathematical properties. Figure 1.11 shows the procedure to obtain Voronoi architecture. This method will be discussed in detail in the next chapter. Vijayavenkataraman et al., used Triply periodic minimal surface (TPMS) design to print the ceramics (Alumina) as an implant [153]. Yu et al. [154] and Yang et al. [155], mechanically analyzed the TPMS structures. Gyroid, diamond schwarz-p and neovius shapes are examples of TPMS geometries.
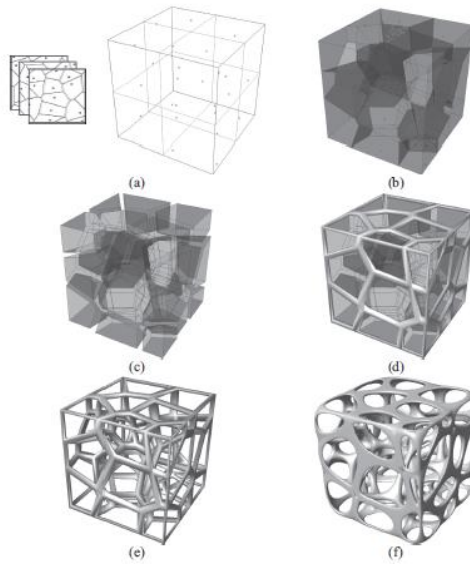
Figure 1.11. Procedure to obtain Voronoi structure. a) 2D Voronoi point coordinates (x,y) are processed at equal z distances to obtain the 3D coordinates (x,y,z) of all points. b) in the second step, the coordinates are processed to obtain the 3D Voronoi cell structure, c) each plane surface is self-copied and translated a fixed distance to create an open internal connected volume, d) and e) the porous external (c) and internal (d) Boolean operations are done to get contours and f) Final step is smoothing process to soften the mesh model. Taken from [149].

(i) NNP = 5; $\Phi(\%)$ = 89   (ii) NNP = 5; $\Phi(\%)$ = 69   (iii) NNP = 5; $\Phi(\%)$ = 49
(a)

(i) NNP = 5; $\Phi(\%)$ = 89   (ii) NNP = 25; $\Phi(\%)$ = 89   (iii) NNP = 50; $\Phi(\%)$ = 89
(b)
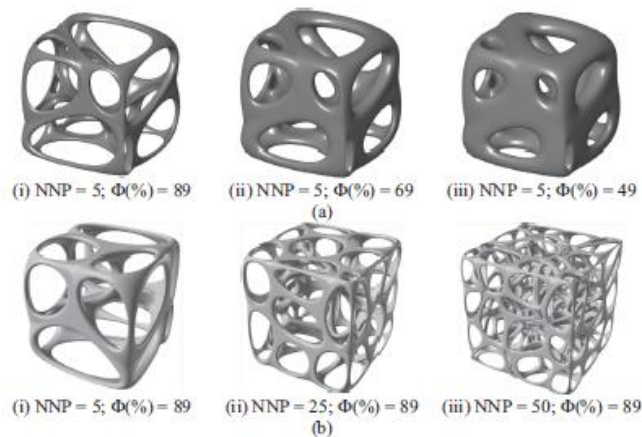
Figure 1.12. Number of nucleation points (NNP) and radii multiplier's effect on porosity. a) Shows the constant number of nucleation points with different porosity

(Φ) by tunning the trabecular separation and thickness. b) The constant porosity with different nucleation points. Taken from [149].

1.3.3   Scaffold Production Techniques

As is discussed previously, scaffolds are the essential parts of the BTE, and their physical and chemical properties such as mechanical, biocompatibility, and biodegradability are inevitably important factors. Sufficient mechanical strength during regeneration and repair, interconnected porosity to supply nutrients and oxygen and discard waste, and proper degradations rate in bone formation to preserve structural integrity are the main features needed to have a good scaffold design [156]. Various scaffold fabrication techniques help us to choose the best method according to desired properties and field of application. Some of these fabrication techniques can be categorized as freeze-drying, solvent castin, particulate leaching, gas foaming, thermally induced phase separation (TIPS), sol-gel method, electrospinning and additive manufacturing (AM). Additive manufacturing technique which is used in this study is described in next section.

1.3.3.1   Additive Manufacturing

Additive manufacturing (AM) or rapid prototyping is developed to fabricate complex and large geometries with a fine level of precision by adding layers on top of each other. As a result, printing imperfections and mechanical properties can be decreased and enhanced, respectively. This process is controlled by a computer. 3D models can be obtained by CAD or imaging techniques. After selecting the proper material according to the field of application, required porosity, mechanical and biological properties, the manufacturing process of scaffolds is chosen. The final steps would be the preclinical and clinical experiments (Figure 1.13). Three-dimensional printing (3D printing) is additive manufacturing (AM) technique, invented in Massachusetts Institute of Technology as inkjet printing liquid binder

solution onto a powder bed [157]. 3D printing provides flexibility to obtain optimum accuracy [30]. The influence of scaffold geometry, architecture and porosity, pore size, topography and wettability on cell behavior can be studied by rapid prototyping. Nozzle deposition-based AM techniques have shown superior flexibility among other processes. For PLA, 3D printing results in high precise geometries than other conventional methods [121].

AM can be divided into a few subcategories: fused deposition modeling (FDM), direct energy deposition, inkjet printing and contour crafting, stereolithography (SLA), laminated object manufacturing, and powder bed fusion.
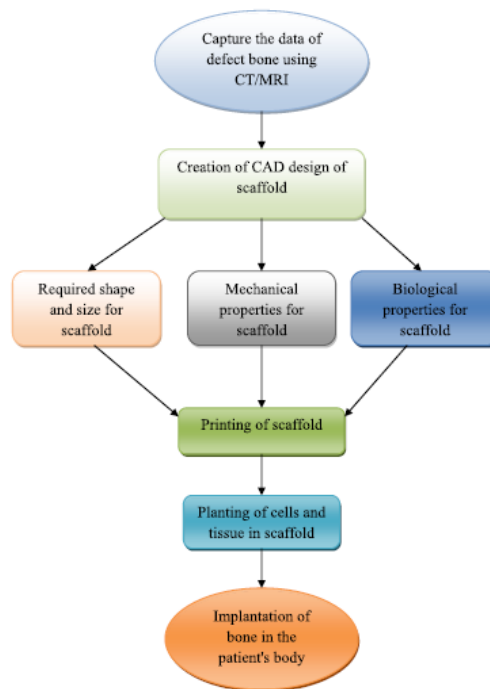
Figure 1.13. Representative flowchart for additive manufacturing. Taken from [30].

There are some terms and parameters associated with 3D printing:

- *Printing orientation:* After loading the 3D model on the slicing software the orientation of the printing can be altered. This term shows the direction that model is printed.

- *Layer height:* The thickness which the nozzle prints a single layer. By decreasing the layer thickness the printing time increases.

- *Fill density:* Infill parameter describes the density which the outer shell of material is filled with. This parameter can be changed from 0% to 100%. 0 indicates the outer shell and 100 is a solid block. By increasing the infill density, the mechanical properties and printing time will be increased.

- *Printing speed:* The velocity at which the printer extrudes material is known as printing speed. This parameter inversely effects the quality of the final product.

- *Extrusion temperature:* It is a temperature at which material is extruded on the platform. Too hot or too cold extrusion temperatures result in poor quality of the final print [158].

1.3.3.1.1 Fused Deposition Modeling

In fused deposition modeling (FDM) technology, polymer filaments are guided to the nozzle and heated to the point that they convert to a semi-liquid phase. The liquid is extruded through a nozzle to the platform, and they make 3D structure by layer-on-layer method. The critical point in this method is the thermoplasticity of the material. Due to this feature, filaments fuse together in printing and then solidify at room temperature. Some parameters are influencing the mechanical properties of the final product e.g., layer thickness, the void between the layers or in the same layer, and filament orientation and post-modification [159]–[161]. Sood et al., found that the main reason for the low mechanical strength is the distortion between the layers [162]. FDM is an easy way of manufacturing, the production cost is low, and it is an eco-friendly and rapid method. While the final product has a layered appearance, its surface quality is low and it is mechanically weak [163], and the thermoplastic polymers are limited [159]. Constructing fiber-reinforced composites using the fused deposition method is proved to enhance mechanical strength [164].

PLA, PCL, and PLGA and their composites are the preferred plastics for FDM [32]. FDM is the most frequently used AM technique to print 3D PLA scaffolds. It was indicated by Chen et al., that FDM does not impose a cytotoxic effect on PLA properties [100]. Large segmental bone defects can be treated using geometric variety and feasibility to print with FDM [165]. FDM method was utilized to 3D printed PLA scaffolds by Grémare and colleagues, and it was shown, FDM decreased both degradation temperature and molecular weight of PLA. They did not report any cytotoxic effect of PLA or FDM on bone mesenchymal stem cells and cells proliferated homogeneously regardless of pore size [166]. Naghieh et al., represented that the FDM process is limited to micro size [167]. Composite materials such as PLA/nHA [168], PCL/PEG [169], and CP/PCL, HA/PCL [170] can also be printed using FDM.

Figure 1.14 shows all the steps from a computer-aided design phase to the clinical phase for a scaffold and in a special case, PLA scaffold.
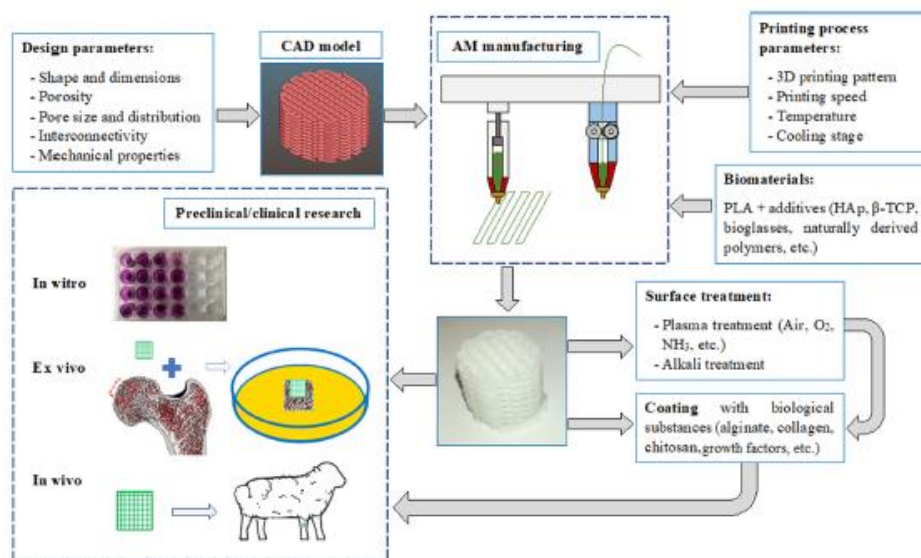
Figure 1.14. Graphical representation of PLA scaffold applications strategies and stages in BTE. Taken from [171].

1.4   Surface Modifications

As important as mechanical properties are controlled surface properties of a biomaterial. These properties include surface free energy, surface roughness and topography, surface charge, wettability, chemical compositions, and reactive functionalities. Surface modification is an approach to control these features [172]. Wettability and surface energy are key factors in cell affinity and cell-like osteoblastic cell spreading. The subsequent events of proliferation and differentiation highly depend on them [173]. For example, surface topography influences osteoblast cell responses, particularly micro-topography [174]. Commonly most polymers have hydrophobic surface which limits their usage in wettable surface demanding applications [175]. PLA does not have any reactive side chains and it is a relatively hydrophobic thermoplastic with a water contact angle between 75˚-85˚, which leads to low cell affinity.

On the other hand, it has a vast area of applications in industrial and biomedical fields [172]. Therefore, it is highly demanded to regulate its properties according to the field of use. There are four principal ways to change the wettability of a surface, surface roughening, surface cleaning, hydrophilic layer coating of the surface, and finally, formation of functional or hydrophilic groups (Figure 1.15).

It was claimed in the literature that the surface wettability increases by introducing roughness [175]. However, this may not be the case for a hydrophobic material like PLA. Roughness extends the surface area, hydrophobic surface trapped the air, hence, increasing the roughness causes more hydrophobicity. Yet, introducing surface roughness has some benefits which will be described in detail later.

Next method to increase wettability is the elimination of the contaminants and impurities such as oil vapors and grease. The first two methods have some constraints since the elevated surface energy cannot be acquired through them.

The third method is the hydrophilic layer coating, in which the success of wettable improvement depends on the hydrophilicity of the coating. It will be described in the next section.

The fourth method is the foundation of hydrophilic groups on the surface. The last two approaches can increase the surface energy of the material to a value higher than its intrinsic one [175].
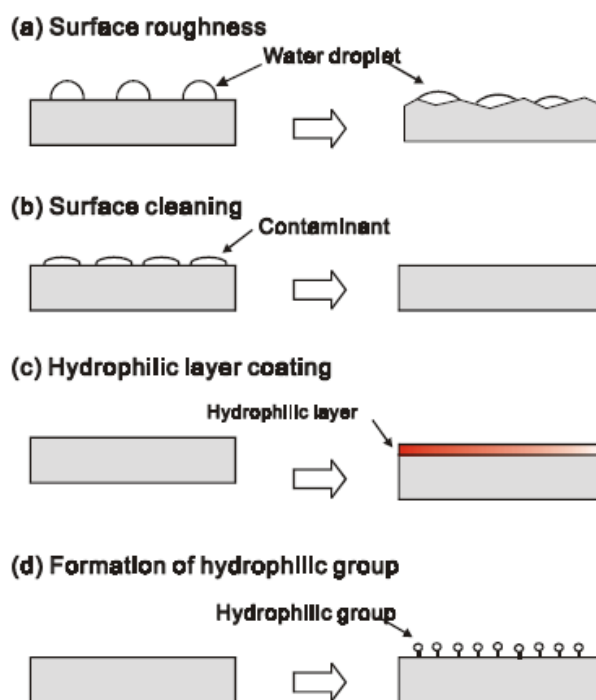
Figure 1.15. Schematic representative of surface wettability improvement. Taken from [175].

Although surface roughening of hydrophobic materials results in more hydrophobicity, imposing nano-roughness has some benefits. The positive correlation between hydrophobic interactions and protein adsorption is a plausible incident [176], [177]. It should not be disregarded that the electrostatic interaction between protein molecule charge and substrate surface assists the adsorption [178]. However, for hydrophobic surfaces with high or moderate ionic bonds the hydrophobic interactions come into the picture. The hydrophobic interactions are qualified by their high entropy and low enthalpy effect [177]. Despite the weak individual hydrophobic interactions and Van der Waals forces, their sum generates

immense driving force for adsorption of proteins to hydrophobic surfaces considering that the surface of a protein is partially nonpolar [179].

It was shown that alkali (NaOH) treatment and surface etching to increase nano-roughness are favorable since they are simple and not expensive [180]. Furthermore, NaOH etching method neither changes the electrostatic charge nor the terminal chemical groups [178]. It was demonstrated that the water contact angle was increased by enhancing the surface's nano-roughness, and increasing these two factors improved the cell morphology, proliferation, and immunophenotype of osteoblasts [176].

1.5   Cell-Surface Interactions

Cell adhesion depends on various parameters related to the substrate surface. These parameters can be categorized as surface topography (porosity and roughness), physical properties of the surface (mechanical properties and wettability), and chemical properties of the substrate surface (surface energy, surface charge and bioactive molecules present on the surface) [181]. The roughness, wettability, and porosity were discussed in previous sections, and in this section, the presence of bioactive molecules will be addressed. The final goal of a successful scaffold implant is to improve cell adhesion, proliferation, and differentiation (Figure 1.16).
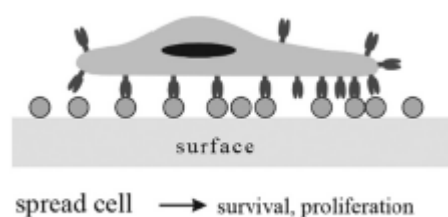
Figure 1.16. Cell adhesion and proliferation on the substrate. Taken from [181].

1.5.1   Surface Modification Techniques

There are several major techniques to enhance and facilitate the cell adhesion. These methods are self-assembled monolayers (SAMs) and polymer brush, layer-by-layer assembly, photolithography, electrospun fibers, 3D bio-printing, and coating.

Coating is a method to improve cell interactions with the substrate surface, which can be inexpensive and straightforward depending on a method which is applied for coating.

Hydrophilic surface modifications or coatings of scaffolds are widely applied to elevate adhesion, proliferation, differentiation, and overall activity of the cells compared to hydrophobic surfaces [179]. The thin coating layer will impose favorable changes in surface properties, while its bulk characteristics will remain intact [182]. The surface coating by collagen [147], [148], [183] and HA [184] are popular ways of improving hydrophilicity of the surfaces and osteogenic differentiation since they are two most important metrices of the bone. Collagen modification presented by Holmes et al., showed great adhesion of mesenchymal stem cells and other cellular function [183]. In research by Martin and colleagues, the PLA scaffolds' surface was functionalized by collagen, minocycline (MH) and citrate hydroxyapatite (cHA). The results showed the combined influence of MH and cHA facilitate the cell adhesion, proliferation and differentiation of hMSCs [148]. Bioglass coating are also applied in the literature to increase HA layer formation in the presence of SBF [185].

Surface coating methods are categorized into several major headlines: vapor deposition (chemical and physical vapor depositions), chemical and electrochemical techniques, spraying, roll-to-roll processes, and finally, physical coating processes. These classes can be classified into different sunsets as well. Conversion coating and ion beam mixing are examples of chemical and electrochemical techniques, plasma spraying, and thermal spraying are the samples of spraying techniques. Langmuir-Blodgett, spin coating and dip coating can be instances for physical coating processes. The coating method selection depends on, nature of the substrate material,

the coater's nature, substrate and coater's level of interaction, the desired accuracy of the end product, and production cost [186].

1.5.2   Dip Coating

Dip coating is a popular way of creating a thin layer on a material's surface. It is composed of few steps in the following order, 1) immersion of a material or a substrate into a coating solution, 2) start-up in which the material is kept in the solution for some time, 3) deposition of a thin layer of coating solution on the substrate and 4) withdrawal of the substrate (Figure 1.17). It is a simple a simple and reproducible method. This method can be done mechanically with a device or simply by immersion with a hand.
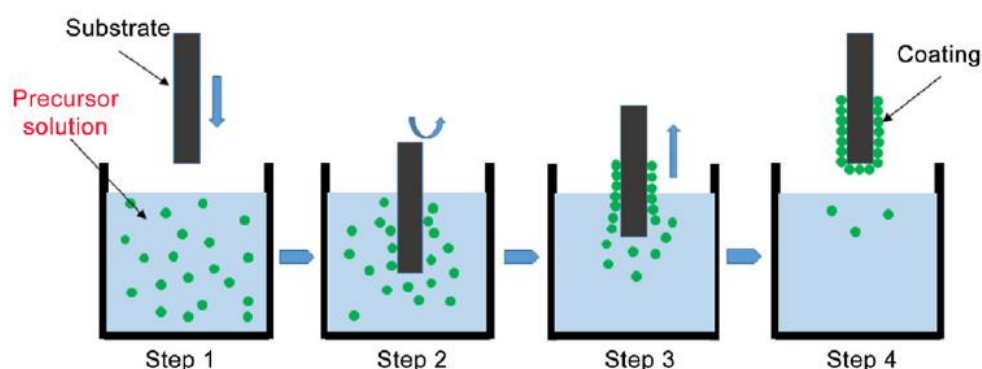
Figure 1.17. Simple graphical representative of steps followed by dip coating. Taken from [187].

In a study, 3D printed PLA microneedles were fabricated and coated with different drug formulations with different formulations and compositions using dip coating to study transdermal drug delivery. They demonstrated that dip coating is an effective and easy method to create uniform drug load on PLA microneedles [188]. Zhu et al., applied dip coating method to coat 3D printed ABS products using coatings based on water. It was shown that dip coating is an efficient method to improve the quality of the surface by decreasing the surface roughness and sealing the gaps without any

damage to the structure of the parts. The effect of number of coating layers of water-based coatings, coating speed and drying states on surface roughness of 3D printed parts were assessed. The coating solutions with larger amount of solids resulted in smother surfaces. The number of the coating layer has the same effect as solid amount [189]. In a research, chitosan/calcium nitrate tetrahydrate or gelatin/calcium nitrate tetrahydrate hybrids were used as coating solution and 3D printed PLA scaffolds were dipped into these solutions. The results demonstrated calcium phosphate deposition is facilitated by gelatin and chitosan [190].

1.5.3   Protein Adsorption

A common method for surface coating is the protein adsorption method [182]. Protein adsorption (hydrophilic layer) which can be enhanced by introducing surface hydrophobicity, is a convenient method to increase the surface wettability and hydrophilicity. Electrostatic interactions between the adsorbent (surface) and the amino acid side chains with the opposite charge result in high free energy change, which favors the protein adsorption [191]. Protein structure is stable due to the hydrogen boned, electrostatic, Van der Waals and Coulomb interactions. On the other hand, the surface may compete for the same attractions by minimizing the total free energy of the system through protein unfolding. So, protein adsorption has the potential to induce protein denaturation [192]. Depending on the protein, the structural deformations may cause cell adhesion. Protein induced cellular activities, are highly dependent on two factors. First, on the whole, adsorption process of proteins on an implanted surface and protein amounts and types are absorbed. Second, the protein's bioactivity can be defined as protein's capacity to activate cell adhesion, differentiation, or other responses [179].

Protein structure variation is another factor contributing to the entropy increasing. Therefore, the larger molecules have higher hydrophobic interactions than smaller rigid ones [177]. Figure 1.18 shows the size effect on the interactions.
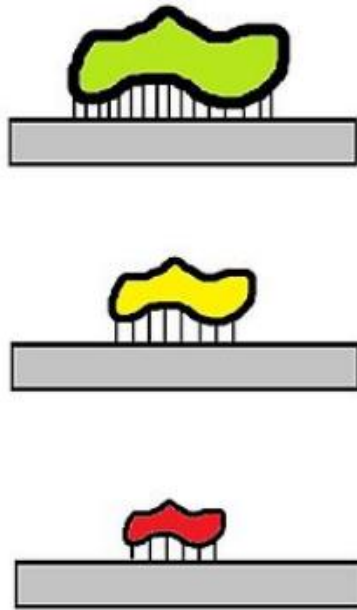
Figure 1.18. Size effect on protein-surface hydrophobic interactions.

Moreover, the diffusion coefficient of protein and its affinity of it for the surface are among the top properties determining the quality of the protein adsorption. The reversibility of the adsorption, in a simple description, the tightness that a protein sticks to the surface, influences the capability of the cells to bind and act properly in contact with a surface [179]. In fact, protein adsorption is a very dynamic process and the immobilization of the proteins on the surface may not be permanent [173]. There are some attempts in the literature using extracellular matrix proteins such as, collagen type I [182], [193], RGD [194], fibronectin and vitronectin [195], albumin [196], etc., as a surface coating to enhance cell adhesion, proliferation and differentiation. Collagen is shown to be one of the widely considered coatings to enhance cell adhesion and proliferation and osteogenic differentiation [182], [197]–[199]. The osteoconductive effect of type I collagen coating on 3D PLA scaffolds was shown by Teixeira et al. [15].

36

1.6   Mechanical Characterization

Bone tissue is classified as a brittle material in terms of mechanical properties, yet, it has good mechanical strength in terms of load bearing. Compact and cancellous bones are two types of human bone tissue. While compact bone has a porosity of 5-10%, trabecular bone shows 50-90% porosity. Human skeleton weight is mainly composed of cortical bone (80%), and 20% accounts for cancellous bone. The compressive strength and elastic modulus of compact bone is enormously higher than that of trabecular bone. To avoid or reduce stress shielding and have adequate mechanical strength, mechanical properties of the scaffolds should resemble the native bone tissues for load-bearing and no-load bearing bone repair [200]. Porosity, pore size, architecture, and degradation rate of the scaffold in aqueous solutions like SBF and in the presence of enzymes are the factors that influence the mechanical strength in a reverse direction. Porosity and pore size are the factors that have a significant impact on cell proliferation and bone ingrowth. Apart from porosity, layer thickness, fill density, printing orientation, printing speed and extrusion temperature are the other critical factors that directly affect the mechanical strength of the 3D printed scaffolds [158]. The effect of pore size [201], build orientation [202], layer height, fill density, extrusion temperature and printing speed [158], manufacturing direction and superimposed static stresses [203], application of the load according to the layering axis [204]. The study accomplished by Murugan et al, demonstrated that layer height affects mostly the built time and ultimate tensile strength. However, extrusion temperature is responsible for elastic modulus [158]. Mechanical strength and balancing all these parameters to achieve the final goal is a big challenge in scaffold fabrications for the purpose of bone tissue engineering and bone regeneration [30].

Tension, compression, bending, strength and elastic modulus are some parameters that can be tested for scaffold purposes [205]. Tension and compression test are among the most common ways to measure the mechanical properties of a design. There are some terms associated with these tests,

Stress:

Stress is the ratio of external forces to the cross-sectional area. It can be calculated via,

$$\text{Stress } (\sigma) = \frac{F}{A}, \tag{1.1}$$

where, σ is stress, F is force and A is the cross-sectional area. Stress has a unit of N/m^2 or Pa.

Strain:

Strain is the deformation under stress and defined as the ratio of change in length to the original length. Strain is dimensionless and can be calculated as,

$$\text{Strain } (\varepsilon) = \frac{\Delta L}{L_0}, \tag{1.2}$$

where, ε is strain, ΔL is change in length and L_0 is the original length.

Elastic modulus:

Elastic modulus, or it can be referred to as Young's modulus, is the relationship between tensile stress and strain or stress/strain. In the linear region, the elastic modulus is calculated by Hook's law ($\sigma = E\varepsilon$),

$$E = \sigma / \varepsilon, \tag{1.3}$$

in which σ is stress, ε is strain, and E is elastic modulus. Elastic modulus has the unit same as stress (Pa). The elastic modulus of a polymer is a function of several factors, e. g., its molecular weight, production technique, temperature and crosslinking density. Their tensile strength and modulus increase to a limiting value [206].

Tangent modulus:

The tangent modulus is the slope of stress-strain curve in compression, and it is equal to Young's modulus in the elastic (linear) region.

Flexural modulus:

Flexural modulus is the stress-strain relation in the bending.

Tensile or compression strength:

Tensile strength can be defined as the uppermost stress a scaffold can tolerate before failing [205].

Some of these terms are graphically represented in the Figure 1.19.
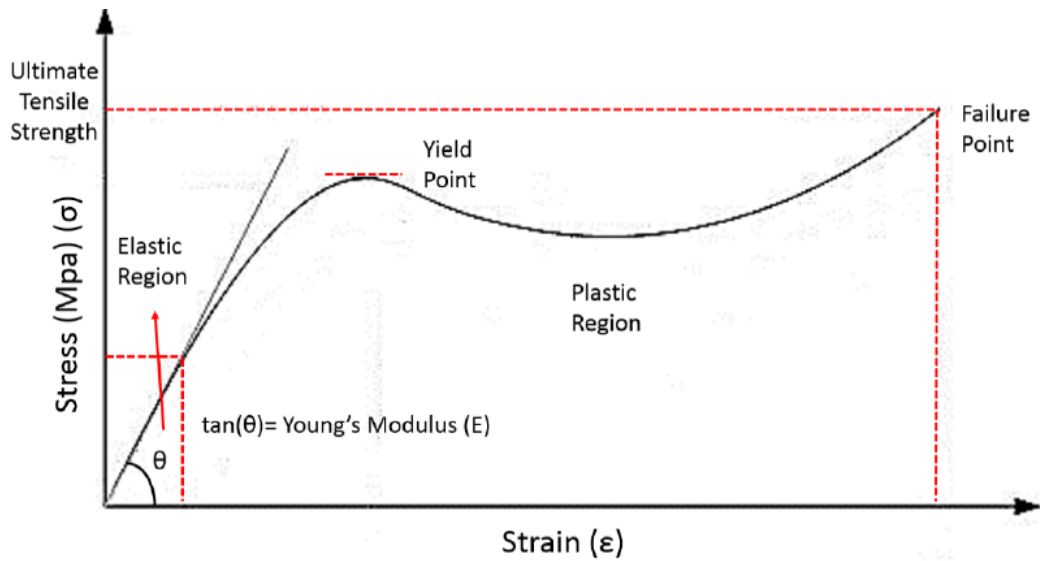
Figure 1.19. The representative stress-strain curve for a thermoplastic polymer.

The parameters affecting the mechanical strength of the scaffold were considered and argued in detail. Here we will survey some of the works accomplished to characterize the scaffolds, chiefly 3D printed and PLA material.

The mechanical properties of the AM parts can be affected not only by manufacturing methods, parameters and conditions but also the material properties before printing [207].

The results can be summarized as,

- The yield strength, ultimate strength, elasticity, and strain at break were the parameters analyzed in most of the studies [207].
- Rapid prototyping has superiority over other conventional fabrication methods such as solvent casting, particle leaching, gas foaming, TIPS in terms of mechanical properties [208].
- Scaffolds based on circumferential fiber structure had more equilibrium modulus than straight fibers [209].
- The mechanical properties of lactic acid-based polymers vary from soft and elastoplastic to stiff with higher strength. Therefore, for higher mechanical properties applications semi crystalline PLA is favored [80].

- The ultimate strength of PLA depends on many parameters such as layer height, printing orientation and speed, extrusion temperature, infill density and pattern, and nozzle diameter [203].
- Increasing in porosity leads to lower mechanical strength [107].

1.7 Thesis Objectives

This study is expected to produce a bone tissue engineering scaffold that can balance mechanical strength and cell biocompatibility in a single design. The scaffold was enhanced for its osteogenic capacity by collagen-bioglass coating, which can mimic bone extracellular matrix (ECM). The specific objectives can be summarized as follow,

- Fabrication of biocompatible and biodegradable bone scaffolds with different geometries using rapid prototyping and mimicking the human bone in terms of structural properties (especially Voronoi structure) that can resemble the microstructure of the trabecular bone.
- Synthesis of the bioglass nanoparticles (BG-NPs) and coating them onto the scaffolds together with collagen to enhance the similarity of the scaffold surface to the organic and mineral composition of the bone and thus, to increase its osteogenic potency.
- Showing cell migration, proliferation, and osteogenic properties of the hFOB cells on the scaffolds.
- Demonstrating the in-vitro degradation, mechanical and other important properties of the scaffolds for BTE purpose
- Providing interconnected network through human osteoblast encapsulated gelatin methacryloyl (GelMA) filling inside the porous PLA scaffolds and in vitro investigating its further contribution to bone regenerative properties

1.8 Thesis Novelty

Considering state-of-the-art, the current study aimed at filling the existing research gap for bone tissue engineering scaffolds in terms of conducting a comprehensive study on the effect of internal architecture of 3D printed polylactic acid (PLA) scaffolds. The generated different design scaffolds were improved BTE properties

with collagen and bioglass coating. Specifically, at the first step, this study proposed at least 20 different geometries to infer the effect of internal design on mechanical properties through experimental tests. For this purpose, it was observed that most studies in the literature have focused on investigating a limited number of geometries. Moreover, in vitro tests were done on the 3D printed, mechanically characterized geometries. In particular, in vitro tests on Voronoi type collagen-bioglass coated PLA scaffolds were conducted for the first time to the best of our knowledge.

Another novel aspect of this thesis is the usage of collagen-bioglass for coating 3D printed PLA. The collagen-bioglass composite coating is expected to enhance the osteogenic properties of the scaffolds. Combining 3D printing of biodegradable biomaterials and surface modification with composites introduces a new bi-component composite bone tissue engineering purpose.

The combination of GelMA hydrogel, bioglass 58S nanoparticles, collagen type I and PLA was used for the first time. Filling the porous scaffolds with collagen, BG, and cell laden GelMA hydrogel to provide the interconnected network and facilitate cell migration is another innovative study feature.

CHAPTER 2

MATERIALS AND METHODS

2.1   Materials

List of the materials used to complete the thesis are provided in alphabetic sequences in Table 2.1.

Table 2.1 List of materials and companies in alphabetic Sequences.

Material	Company (Country)
4',6-diamidino-2-phenylindole (DAPI)	Invitrogen (USA)
Acetic acid (Glacial)	Merck (USA)
Alamar Blue^{TM} Cell Viability Reagent	Invitrogen (USA)
Alexa Fluor 488 Goat-Anti-Mouse	Invitrogen (USA)
Alexa Fluor 555 Goat-Anti-Rabbit	Invitrogen (USA)
Alexa Fluor 488 phalloidin	Invitrogen (USA)
Alexa Fluor 647 phalloidin	Invitrogen (USA)
Alizarin red solution	Cyagen Bioscience (USA)
Ammonia	Merck (USA)
Anti-collagen type I antibody (ab138492)	Abcam (UK)
Anti-osteocalcin antibody (ab13418)	Abcam (UK)
Anti-osteonectin antibody (33-5500)	Invitrogen (USA)
Anti-osteopontin antibody (ab 8448)	Abcam (UK)
Calcium nitrate tetrahydrate	Merck (USA)
Collagenase Type II	Gibco (USA)
Dexamethasone	Sigma-Aldrich (USA)
Dipotassium phosphate (K_2HPO_4)	Merck (USA)
Direct Red 80	Fluka (Switzerland)
DMEM/F-12 (Dulbecco's Modified Eagle Medium)	Gibco (USA)
Ethanol	Sigma-Aldrich (USA)

Table 2.1 (cont'd) List of materials and companies in alphabetic Sequences.

Ethylenediamine tetra acetic acid (EDTA)	Sigma-Aldrich (USA)
Fetal Bovine Serum (FBS) (Heat Inactivated European Grade)	Sartorius (Israel)
G418 (Geneticin®)	Gibco (USA)
Gelatin type A from porcine skin	Sigma-Aldrich (USA)
Hydrochloric acid (HCl)	Merck (USA)
Irgacure 2959 (2-Hydroxy-4′-(2-hydroxyethoxy)-2-methylpropiophenone 98%)	Sigma-Aldrich (USA)
L-Ascorbic acid	Sigma-Aldrich (USA)
Live/Dead^{TM} Viability/Cytotoxicity Reagent	Invitrogen (USA)
Magnesium chloride (MgCl$_2$)	Merck (USA)
Methacrylic Anhydride	Sigma-Aldrich (USA)
Monopotassium phosphate (KH$_2$PO$_4$)	Merck (USA)
Nitric acid	Isolab (Germany)
Paraformaldehyde	Santa Cruz Biotechnology (USA)
Penicillin-Streptomycin (Pen-Strep) solution	Sartorius (Israel)
Piperazine-N, N'-Bis (ethanesulfonic acid) (PIPES)	Sigma-Aldrich (USA)
P-nitrophenyl phosphate liquid substrate system	Sigma-Aldrich (USA)
Poly-Lactic Acid (PLA)	FormFutura (The Netherlands)
Potassium hydroxide (KOH)	Merck (USA)
Proteinase K from Tritirachium album	Sigma-Aldrich (USA)
QuantiT^{TM} Picogreen Reagent^{TM} ds DNA Assay Kit	Invitrogen (USA)
Sodium azide	Sigma-Aldrich (USA)
Sodium bicarbonate (NaHCO$_3$)	Merck (USA)
Sodium carbonate (Na$_2$CO$_3$)	Merck (USA)
Sodium chloride (NaCl)	Merck (USA)
Sodium hydroxide (NaOH)	Merck (USA)
Sylgard^{TM} 184 Silicon Elastomer Base	Dow (USA)
Sylgard^{TM} 184 Silicon Elastomer Curing Agent	Dow (USA)
Tetraethyl orthosilicate (TEOS)	Merck (USA)
Triethyl phosphate (TEP)	Merck (USA)
Tris(hydroxymethyl)aminomethane (Tris)	Merck (USA)
Triton X-100 solution	Acros Organics (Belgium)
Trypsin EDTA solution B	Sartorius (Israel)
β-glycerophosphate disodium salt hydrate	Sigma-Aldrich (USA)

2.2   Methods

2.2.1   Designing PLA Scaffolds

The scaffolds design comprises three main structures: regular geometries, Voronoi geometries, and minimal surfaces.

The regular geometries, i.e., geometries with at least two axes of symmetry, were designed using SolidWorks as a computer-aided design (CAD) software. Features such as the Boss-Extrude, Cut-Extrude, Circular Pattern, and Mirror were used to generate the geometries shown in Figures 2.1 and 2.2. Particularly, cubical, parallelepipedal, cylindrical solid shapes, and porous shapes were chosen. Among the porous shapes, the porosity (%) and the cubical pores' size were varied. Moreover, cubical and cylindrical shapes composed of "filaments" of square or circular cross-section were generated.
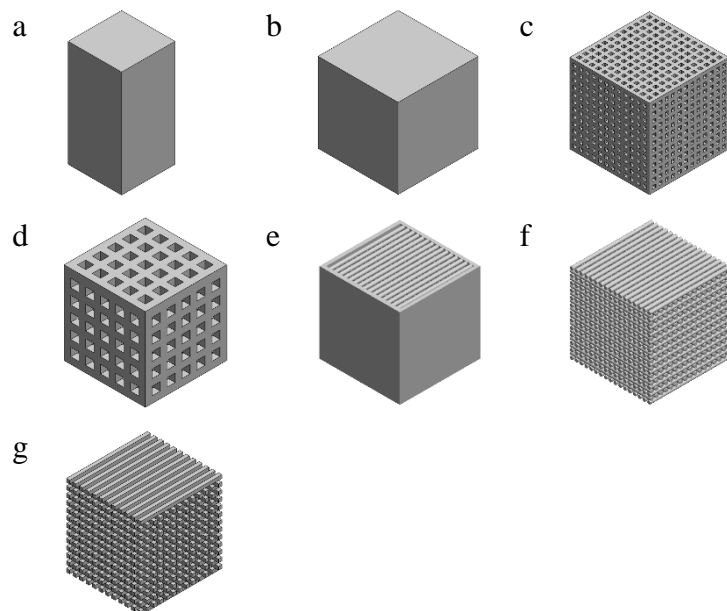
Figure 2.1. Regular cubical designs. a) parallelepipedal ($12.7\ mm \times 12.7\ mm \times 25.4\ mm$) and 100% infill, b) cube with 100% infill, c) cube with 47% porosity and pore size of 0.4 mm, d) cube with 51% porosity and pore size of 1mm, e) cube with

38% porosity and pore size of 0.2 mm, f) cube with 45% porosity and pore size of 0.2 mm, and g) cube with 52% porosity and pore size of 0.4 mm. The dimensions from b-g are $(10\ mm \times 10\ mm \times 10\ mm)$.
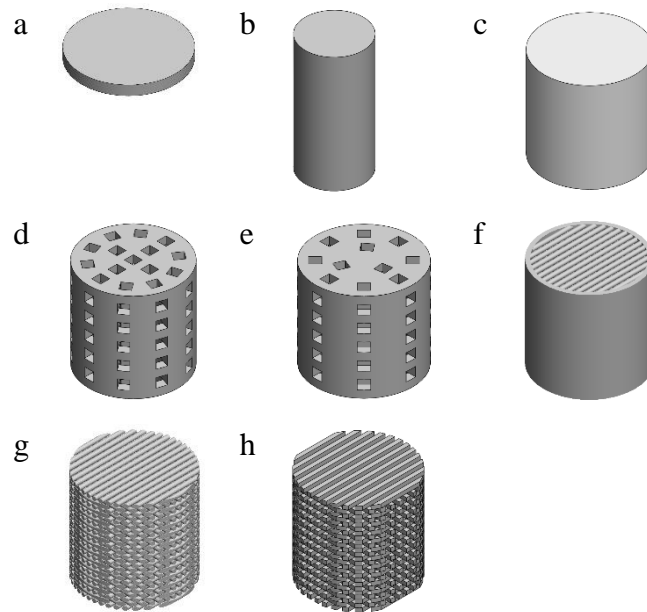
Figure 2.2. Regular cylindrical designs. a) cylinder with 100% infill and diameter of 10mm and height of 1 mm (disk-shaped), b) cylinder with 100% infill and diameter of 12.7 mm and height of 25.4 mm, c) cylinder with 100% infill, d) cylinder with 38% porosity and pore size of 1 mm, e) cylinder with 31% porosity and pore size of 1 mm, f) cylinder with 39% porosity and pore size of 0.2 mm, g) cylinder with 45% porosity and pore size of 0.2 mm and h) cylinder with 50% porosity and pore size of 0.4 mm. The diameter from c-h is 10 mm and the height is also 10 mm.

The Voronoi scaffolds were designed using the concept of the Voronoi diagram [210]. In summary, a Voronoi diagram consists of a plane separated into regions or Voronoi cells. In the most straightforward formulation, each cell contains a certain point called a seed. The region of the cell is defined as the region containing all the points that are closer to the seed of that cell than to any other seed in the remaining

cells of the diagram. Moreover, the vertices of each cell are the points equidistant to at least three seed points.

The CAD software Rhinoceros 3D was used to generate the Voronoi structures. Particularly, the Grasshopper visual programming language, was chosen due to its versatility and robustness to create and visualize complex geometries in the environment of Rhinoceros. The Voronoi structures were generated through the following steps: (1) the dimensions of the bounding box are defined; (2) the 3D bounded box is populated with Voronoi seeds (25, 50, or 75 points); (3) the Voronoi cells are created using the seed points; (4) the structure is generated by means of Bezier curves to generate a smooth trabecular structure, and three different radii multipliers are chosen (0.8, 1.0, or 1.2); (5) the volume of the trabecular structure and the volume of the bounding box are computed and the porosity (%) was calculated. Voronoi designs are shown in Figure 2.3.

The minimal surface structures were also generated using Rhinoceros 3D with Grasshopper. A minimal surface is a surface that minimizes its area locally. Herein, triply periodic minimal surfaces were chosen. Namely, Schwarz-G (Gyroid), Schwarz-P, Schwarz-D (Diamond), and Neovius. Each can be approximated by $F(x,y,z)$ equations using trigonometric functions (cos, sin), as listed in Table 2.2. The block diagram is used to generate the minimal surface structures [211], and minimal surfaces structures are shown in Figure 2.4.
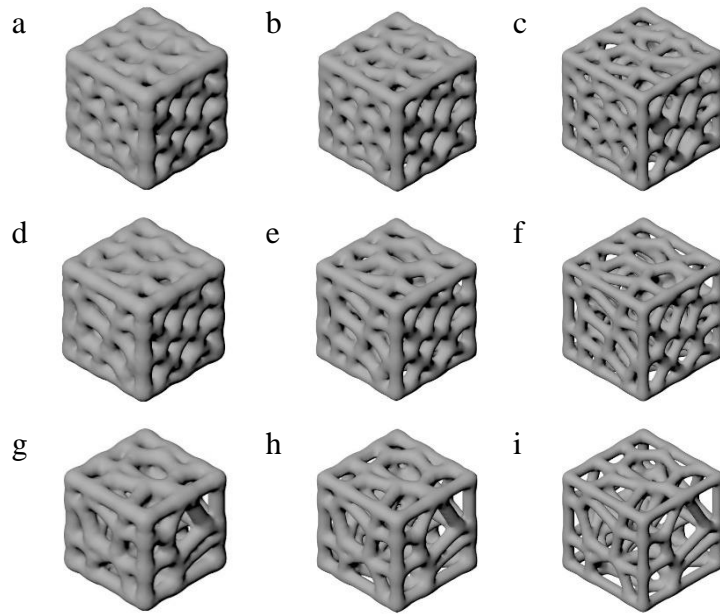
Figure 2.3. Voronoi structures. a-c are Voronoi with 75 seeds or points, a) distance or radius multiplier is 1.2, b) distance is 1 and in c distance is 0.8. d-f) 50 points with distances 1.2, 1 and 0.8 respectively. g-i) 25 points with distances 1.2, 1 and 0.8 respectively.

Table 2.2 Equations used to define the triply periodic minimal surfaces [212].

Schwarz-G (Gyroid)	$cos(x) * sin(y) + cos(y) * sin(z) + cos(z)$ $* sin(x) = 0$
Schwarz-P	$cos(x) + cos(y) + cos(z) = 0$
Schwarz-D (Diamond)	$sin(x) * sin(y) * sin(z) + sin(x) * cos(y) * cos(z)$ $+ cos(x) * sin(y) * cos(z) + cos(x)$ $* cos(y) * sin(z) = 0$
Neovius	$3 * (cos(x) + cos(y) + cos(z)) + 4 * cos(x)$ $* cos(y) * cos(z) = 0$

Figure 2.4. Triply periodic minimal surfaces. a-c) Gyroid structures with 76%, 80% and 85% porosities respectively. d-e) Schwarz-P with 76% and 83% porosities respectively. f) Diamond 76% with porosity. g and h are Neovius structures with 75% and 82% porosities.

2.2.2 Three-Dimensional Printing of PLA Scaffolds

The CAD designs (Standard Triangulate Language or STL files) generated from SolidWorks and Rhinoceros were imported to Ultimaker Cura 4.5. The printing parameters such as layer height (usually 0.1 mm), wall thickness, top/bottom thickness, layer pattern, infill density (100%), printing speed (usually 15 mm/s), travel speed (usually 50 mm/s), and mesh fixes were defined. After slicing, it was exported as a G-Code file to the ULTIMAKER 2+ (The Netherlands) SD card. Premium PLA filaments were printed in different designed geometries according to the exported G-Code file with the 3D printer (ULTIMAKER 2+) around 210℃.

2.2.3   Modification and Characterization of PLA Scaffolds

2.2.3.1   Degradation Analysis of 3D Printed PLA Scaffolds in PBS

Phosphatase Buffered Saline (PBS, 0.01 M) was prepared by adding NaCl (8.7 g) to phosphate buffer (0.5 M, PB) (20 mL) with pH 7.4 and completing the volume to 1000 mL with dH2O.

To make 0.5 M PB buffer, 8.7g dipotassium phosphate (K_2HPO_4) and 6.7 g monopotassium phosphate (KH_2PO_4) were dissolved in distilled water (80 mL). pH was adjusted to 7.4 with KOH pellets and completed to 100 mL. PB buffer was sterilized and used to prepare PBS. Six groups of scaffolds (Figure 2.5) with five replicas per group were placed in well plates individually and immersed in 4 mL of PBS for 120 days, and the PBS was replaced every week. This experiment was carried out at room temperature. The samples were taken out from PBS every 7 days, washed, air dried overnight and weighed. The weight loss is calculated through equation 2.1.

2.2.3.2   Enzymatic Degradation Analysis of 3D Printed PLA Scaffolds

Five groups (Figure 2.6) with three replicas per group were placed in well plates and immersed in 2 mL of enzymatic solution which is made of 0.05 M Tris-HCl buffer solution with pH 8.6 containing sodium azide (0.2 mg/mL) and proteinase K from Tritirachium album (0.2 mg/mL). This study was carried out at 37℃ for 5 days and 10 days. The buffer was replaced every day in order to keep high enzymatic activity. The scaffolds incubated in solution without enzyme (proteinase K) were considered as control groups [92]. The samples were taken out from solution on 5th and 10th days, washed, air dried overnight and weighed. The weight loss is calculated through,

$$\text{Weight loss}\,(\%)\ = \frac{W_2 - W_1}{W_1} \times 100, \qquad\qquad (2.1)$$

50

W_1 is the weight of the sample at day zero before starting the degradation and W_2 indicates the weight of the dried sample at the end of the degradation period.
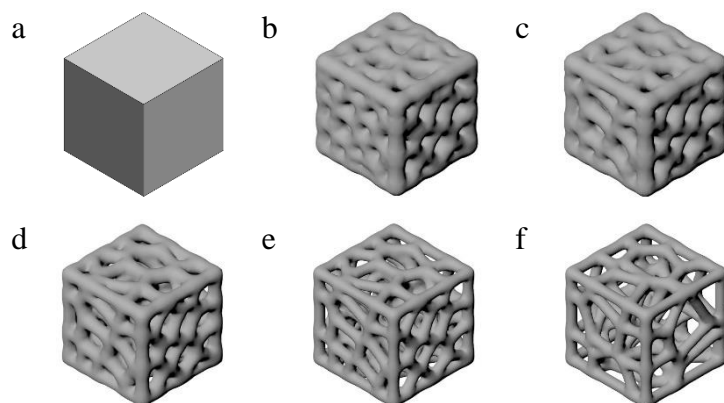
Figure 2.5. Geometries used for degradation in PBS. a) Cube with 100% infill, b) Voronoi 75 points with distance 1.2, c) Voronoi 50 points with distance 1.2, d) Voronoi 50 points with distance 1, e) Voronoi 50 points with distance 0.8, f) Voronoi 25 points with distance 0.8.
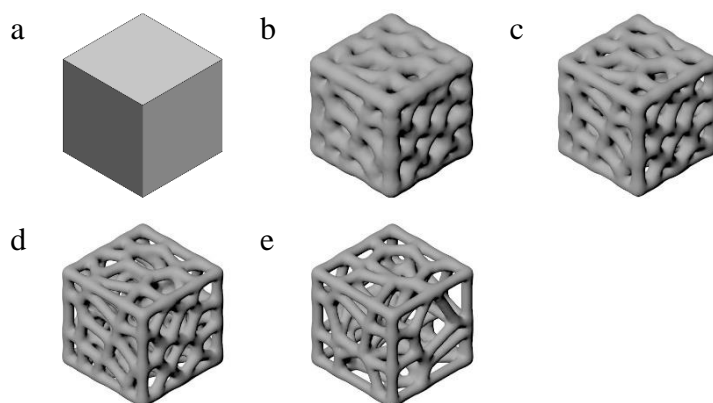
Figure 2.6. Geometries used for enzymatic degradation. a) Cube with 100% infill, b) Voronoi 50 points with distance 1.2, c) Voronoi 50 points with distance 1, d) Voronoi 50 points with distance 0.8, e) Voronoi 25 points with distance 0.8.

2.2.3.3   Porosity Analysis of 3D Printed PLA Scaffolds

The porosity of the samples was calculated theoretically through CAD designs. The formula below was used,

$$\text{Porosity } (\%) = \frac{V_t - V_p}{V_t} \times 100,$$

(2.2)

In which the V_t is the volume of the sample 100% infilled and V_p is the volume of the porous sample [213].

2.2.3.4   Surface Modification of PLA Scaffolds

The disk-shaped PLA scaffolds were immersed in 0.05, 0.5, and 5 M NaOH solution and placed on the magnetic stirrer for half an hour. 3D scaffolds were immersed in 0.05 M NaOH and vacuumed. All samples were rinsed 3 times with distilled water for 15 minutes each time to obtain the alkaline-modified scaffolds and change the hydrophilicity.

2.2.3.5   Water Contact Angle Measurements

The contact angle of the surface treated scaffolds with different molarities of NaOH (0.05M, 0.5M and 5M) were measured with contact angle goniometer (Attension, Biolin Scientific, Sweden). The droplet of dH_2O (7µL) was placed on a sample, and the contact angle between water and sample was measured through static sessile drop method. Average contacts angles were calculated from repeated measurements (n=3). Figure 2.7 represents a three-phase system and water contact angle (θ).
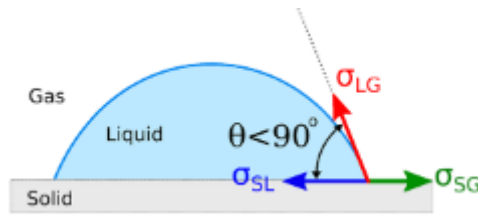
Figure 2.7. Three-phase system and water contact angle (θ). Taken from [214].

2.2.4   Bioglass Synthesis and Characterization

Bioglass 58S was synthesized in order to mimic the inorganic bone matrix. It was used to coat the PLA scaffolds after alkali treatment. BG is added to collagen - 5% acetic acid solution (0.5% (w/v)) in different concentrations. Quick alkali-mediated sol-gel technique used to synthesize the BG 58S is described below.

2.2.4.1   Quick Alkali-Mediated Sol-Gel Method

The 58S bioglass nanoparticles (BGNPs) ($SiO_2:CaO:P_2O_5$) (58:38:4 wt%) were prepared using methodology given in literature [215], [216], [130]. Briefly, Tetraethyl orthosilicate (TEOS) (20 mL) was added to pure ethanol (50 mL), then distilled water (13.9 mL) and nitric acid (2 M, 2.8 mL) were mixed with ethanol and TEOS and stirred for 30 min. Triethyl phosphate (TEP) (2.15 mL) was added and stirred for 20 min more. Calcium nitrate tetrahydrate (14.04 g) was added and after dissolving completely, 1M ammonia solution was also added dropwise under aggressive stirring to obtain a clear acid sol. After rapid gelation of sol, a muddler was used to mix the gel. The gel was dried in the oven at 60°C overnight and subsequently, it was calcined at 600°C in a muffle furnace and sieved (212 μm) to obtain BG nanoparticles.

2.2.4.2   Bioglass NP Characterization

2.2.4.2.1   X-Ray Diffraction (XRD) Analysis

X-ray diffraction method was used to assess the crystal structure and existing phases in bioglass particles. The diffractometer was run at 2θ angle of $10 - 80°$ using step size of $0.02°\!/S$ at 40 kV and 30 mA [217]. The XRD analysis was conducted in Middle East Technical University, Central Laboratory.

2.2.4.2.2   Particle Size Analysis

Particle size and size distribution of BG partices were analyzed using a zeta sizer (Malvern, UK) device in Center of Excelence in Biomaterials and Tissue Engineering (BIOMATEN), METU. Bioglass particles were diluted in dispersant (distilled water). Three concentrations (0.01, 0.1 and 1 mg/mL) of the BG in dH_2O were used. The reflection index was set as 1.55 (commercial BG reflection index) and absorption as 0.001. 1 mL of each concentration was used to measure the particle size.

2.2.4.2.3   Transmission Electron Microscopy (TEM) Analysis

To further investigate the BG particles' size, shape and other morphological properties, transmission electron microscopy analysis was applied. The STEM module of the SEM (FEI Quanta Feg 450) was used for the analysis. The samples were suspended in water and the suspension was added on the TEM meshes dropwise. The samples were air dried and imaged using the STEM detector of the SEM.

2.2.4.2.4 Inductively Coupled Plasma Optical Emission Spectrometer (ICP-OES) Analysis

ICP analytical method was used to determine the chemical elements of the BG 58S nanoparticles. This test is done in Middle East Technical University central laboratory. The particles are dissolved in 2% NO_3 and the sample was sent to argon plasma at a temperature of $6000°K$-$10000°K$. The bonds were broken in the plasma, and atoms and ions were formed. The formed atoms and ions were immediately excited in the plasma and radiate at characteristic wavelengths and returned to their former energy levels. Emission signals were measured by Echelle polychromator and S-CCD (charge-coupled device) array detector system. Observation limits were at the level of µg/L. The oxidation formula can be achieved through the oxide conversion factor.

2.2.5 Coating of 3D Printed PLA Scaffolds

2.2.5.1 Collagen Coating of 3D Printed PLA Scaffolds

The disk-shaped scaffolds and selected 3D designs (Figure 2.8) were used for coating. The scaffolds are selected according to irregularity of pores, size of the pores, porosity and mechanical strength. Rat tail Collagen Type I was offered by a colleague (Collagen type I was isolated from male Sprague-Dawley rat tails and kindly provided by Dr. Gözde Eke, BIOMATEN, Turkey). After treating with NaOH solution, the printed PLA scaffolds were rinsed with distilled water several times to remove the NaOH. Then, the selected group of scaffolds were immersed in 0.5% (w/v) collagen type I dissolved in 5% acetic acid solution (filtered with 0.45 µm filter) and then freeze-dried.
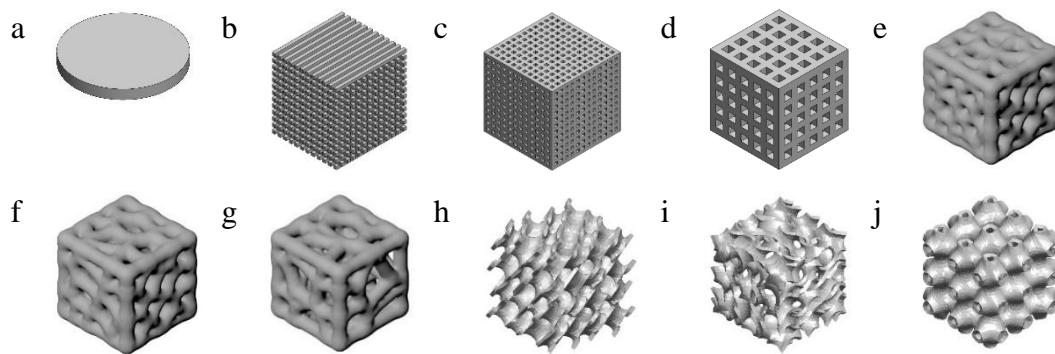
Figure 2.8. Structures used for collagen coating. a) Disk-shaped, b) cube with filaments (52% porosity), c) cube with small regular pores (47% porosity), d) cube with large regular pores (51% porosity), e) Voronoi 75 points, 1.2, f) Voronoi 50 points, 1.2, g) Voronoi 25 points, 1.2, h) Diamond (76% porosity), i) Gyroid (76% porosity) and j) Schwarz-P (76% porosity).

2.2.5.2   Collagen-Bioglass Composite Coating of 3D Printed PLA Scaffolds

The composite for coating scaffolds consisted of 1, 5, 10 and 15% (w/v) inorganic (bioglass) and 99, 95, 90 and 85% organic component (Collagen type I) respectively. The bioglass particles were gradually added to the collagen solution and stirred aggressively. Disk-shaped sample is selected due to its simplicity and considered as 2D and two groups with regular and irregular pore structures with proper mechanical properties are selected for this analysis (Figure 2.9). The samples were immersed in collagen-BG composite, the disk-shaped samples were placed on the stirrer and the 3D ones were vacuumed for 15-30 minutes. Finally, they were lyophilized.

56
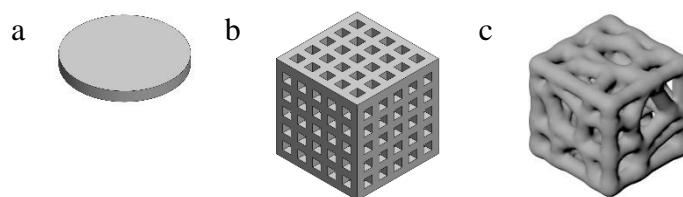
Figure 2.9. Structures used for collagen-BG coating. a) Disk-shaped used for collagen-BG (1%, 5%, 10% & 15%) coating, b) cube with large regular pores (used for collagen-1% BG coating) and c) Voronoi 25 points, 1.2 (used for collagen-1% BG coating).

2.2.5.3   Characterization of Coating

2.2.5.3.1   Attenuated Total Reflectance-Fourier Transform Infrared Spectroscopy (FTIR/ATR)

The composite coating was analyzed using FTIR-ATR to show the chemical interaction between the coating and PLA scaffolds. The samples were scanned in wavenumber range 4000-400 cm^{-1} with the resolution of 4 cm^{-1} [218]. BG nanoparticles, collagen, NaOH surface modified PLA scaffolds) and coated PLA scaffolds (collagen-coated, and collagen/15% (w/v) BG coated) were analyzed with FTIR (Frontier, Perkin Elmer, USA). The FTIR analysis was done in BIOMATEN, METU.

2.2.5.3.2   Direct Red Staining of Collagen Coated Scaffolds

The disk-shaped samples, i) without any treatments, ii) with 0.05, 0.5 and 5 M NaOH treatments, iii) with 0.05 M NaOH-Collagen type I treatment and iv) with collagen-BG (1%, 5%, 10% and 15% (w/v)) treatments were selected to observe their differences. The Direct Red 80 (100 mg/mL) was dissolved in aqueous picric acid in this procedure. The solution was added to the samples in well plates, shacked slowly for 5 min. Finally, the samples were rinsed with HCl until all dye came out. The

samples were imaged with a light microscope. The red staining was applied to evaluate the presence and distribution of collagen on the sample.

2.2.6 Preparation and Characterization of Gelatin Methacryloyl (GelMA) Hydrogels for Coating PLA Scaffolds

In order to provide interconnective network for cell proliferation and migration, GelMA hydrogel was synthesized and characterized. To achieve this goal, the cell-loaded hydrogel was injected with thick and thin needles to the 3D porous scaffolds.

2.2.6.1 Gelatin-Methacryloyl (GelMA) Synthesis

In orderto synthesize GelMA 0.25 M Carbonate-bicarbonate (CB) buffer was used. CB buffer was prepared as; 0.075 M sodium carbonate (Na_2CO_3) and 0.175 M sodium bicarbonate ($NaHCO_3$)) were dissolved in distilled water (900 mL), pH was adjusted to 9 and then volume was completed to 1L.

In the next step, gelatin type A from porcine skin (20 g) was added to CB buffer (100 mL) on a magnetic stirrer. At $50℃ - 60℃$, methacrylic anhydride (2 mL) was added dropwise. The reaction has proceeded for 3 hours. After stopping the reaction, the pH was adjusted to 7.4 with HCl and NaOH. The reaction product was filtered using standard filter paper and transferred to a dialysis tube and dialyzed against distilled water for 2 days. After filtering the dialyzed GelMA with filter paper, the product was poured into polydimethylsiloxane (PDMS) (PDMS+10% curing agent) covered plastic Petri dishes and lyophilized.

2.2.6.2 Curing of GelMA Based Hydrogels

Three types of hydrogels, GelMA, GelMA-collagen and GelMA-Collagen-BG 58S were prepared as:. Irgacure (0.9%, w/v), a photo-initiator for UV curing, was added to Dulbecco's Modified Eagle Medium (DMEM/F-12 1:1). After dissolving

completely at 60°C, 0.5% (w/v) purified Collagen type I and 15% (w/v) GelMA were added to the same medium. Finally, BG was added in different concentrations (0.05, 0.1, 0.5 and 1% w/v). For the swelling test 200 µL of the hydrogel mixture and for mechanical test 500 mL of it were poured to PDMS covered 96 well plates and 48 well plates respectively. They were cured with 0.120J intensity and 365 nm UV wavelength for 1 min using BIO-LINK UV Crosslinker BLX-365 (Vilber Lourmat, France).

2.2.6.3 GelMA Swelling Experiments

GelMA, GelMA-collagen, and GelMA-collagen-BG (1, 0.5, 0.1 and 0.05% (w/v)) samples as a total of 6 groups and 4-6 repeats per group were placed in distilled water, incubated in 37°C and their weight was measured before and after 30 min, 1h, 2h, 3h, and 24h incubations. The swelling ratio was calculated with the formula:

$$\text{Swelling Ratio} \ (\%) \ = \frac{w_2 - w_1}{w_1} \times 100, \tag{2.3}$$

in which w_1 is the dry weight of sample before swelling and w_2 is the wet weight of sample after swelling.

2.2.6.4 GelMA Scanning Electron Microscopy (SEM) Analysis

In all SEM characterizations, samples were placed on aluminum pins and coated with Au/Pd. They were observed with SEM, which is functioned at the voltage of 20 kV and high vacuum [219].
GelMA hydrogels were observed with SEM (FEI Quanta Feg 450) in BIOMATEN, METU.

2.2.7   Mechanical Analysis of Scaffolds

The compression tests were done on samples with different geometries and enzymatically degraded scaffolds using a mechanical test machine (Shimadzu AGS-X Universal Test Machine, Japan) with a 5 kN load cell and constant speed of 0.5 mm/min for most samples and 250 kN load cell for the few of them. The samples were placed between compression plates. The elastic modulus and yield strength was calculated via 3 repetitions. 3D samples and enzymatically degraded scaffolds were compressed up to 90% strain displacement.

Additionaly, GelMA, GelMA-collagen, and GelMA-collagen-BG (1, 0.5, 0.1 and 0.05% (w/v)) samples were tested under compression with 5 N load cell.

The results were obtained as force-displacement data. With the formulas below (2.4 and 2.5), the corresponding stress and strain results were obtained,

$$\text{Stress } (\sigma) = \frac{F}{A}, \tag{2.4}$$

where, σ is stress, F is force, and A is a cross-sectional area. Stress has a unit of N/m^2 or Pa and,

$$\text{Strain } (\varepsilon) = \frac{\Delta L}{L_0}, \tag{2.5}$$

where, ε is strain, ΔL is the change in length and L_0 is the original length.

Since the stress-strain curve for PLA has plastic region and is not linear in the whole plot, the sample's elastic modulus (E) was calculated as the slope of the linear part of the stress-strain curve. According to the Hook's law, stress is proportional to strain multiplied by the elastic modulus $\sigma = E\varepsilon$, so the elastic modulus is,

$$E = \sigma/\varepsilon, \tag{2.6}$$

where, σ is stress and ε is strain.

The yield strength is the region where the elastic response of the polymer changes to plastic response with a short peak. In polymers such as PLA this region cannot be

detected easily, so the 0.2% offset strain method was applied. In this approach, a line parallel to the slop of the elastic region of the stress-strain curve intercepts the strain axis at 0.2%.

Finally, the mean of Young's modulus and yield point and their standard deviation was calculated.

2.2.8   In Vitro Experiments

2.2.8.1   Cell Culture Conditions

Human fetal osteoblast cells, hFOB 1.19 cell line, were cultured in DMEM/F-12 1:1 colorless growth medium with 10% fetal bovine serum, 0.3 mg/mL Gentamicin (G418) and 0.01% Penicillin-Streptomycin (Pen-Strep) solution, at 37 °C in a CO_2 incubator (Panasonic, Japan). Passage 6-8 were used for the experiments.

To observe the osteogenic differentiation, the osteogenic medium was prepared with 10% foetal bovine serum, 0.3 mg/mL G418 and 0.01% Penicillin-Streptomycin (Pen-Strep) solution in DMEM/F-12 growth media and supplemented with 100 nM dexamethasone, 10 mM β-glycerophosphate and 50 μg/mL L-ascorbic acid.

2.2.8.2   Cell Seeding

Samples were sterilized with UV light before cell seeding. Each side of the samples were exposed to the UV light. Cells after proliferation in T175 flasks were washed with PBS and removed with Trypsin EDTA solution B. The number of cells (cells/mL) was calculated using NucleoCounter (Chemometec, Denmark). For cell culture experiments, 35×10^4 cells were seeded on disk-shaped PLA scaffolds i) non-treated, ii) surface modified scaffolds (0.05, 0.5, 5 M NaOH treated), iii) surface modified (0.05 M NaOH treated) and collagen coated scaffolds and iv) surface modified (0.05 M NaOH treated) and collagen-BG (1, 5, 10, 15% (w/v)) coated scaffolds (Figure 2.8a).Cells grown in 48 well plates were used as control group. For

cell culture experiments on special 3D form scaffolds, cells were seeded on i) surface modified (0.05 M NaOH treated) and collagen coated scaffolds (97×10^4 cells/scaffold) (Figure 2.8b-2.8j), ii) surface modified (0.05 M NaOH treated) and collagen-1% BG coated scaffolds (Figure 2.9b & 2.9c) (97×10^4 cells/scaffold). For scaffolds with hydrogel experiments, first GelMA based hydrogel parts were tested; 3×10^5 cells were suspended in 70 μL of GelMA, GelMA-collagen and GelMA-collagen-BG (1, 0.5, 0.1 and 0.05% (w/v)) in 96 well plates and UV cured with 0.120 J intensity for 1 min. Then, 3D-printed PLA scaffolds filled with cell-laden GelMA-collagen (Figure 2.10) and GelMA-collagen-0.5% (w/v) BG (Figure 2.11) were investigated.
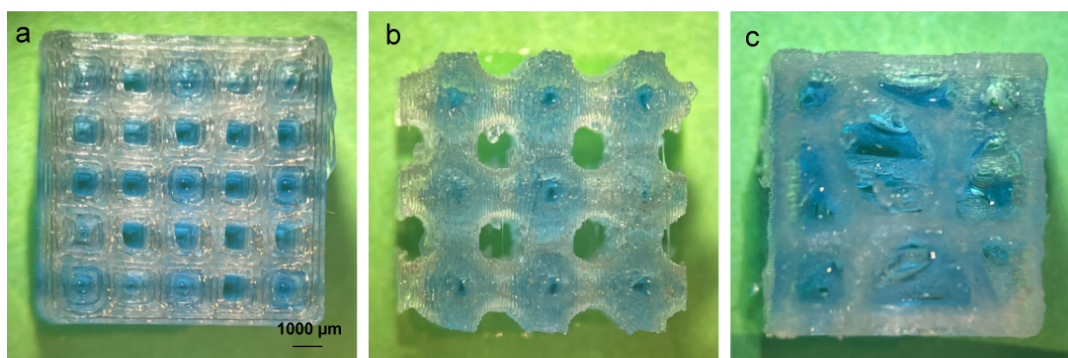
Figure 2.10. 3D-printed PLA scaffolds for hydrogel filling. a) Cube with regular pores, b) Schwarz p 5, c) Voronoi 25 points distance 0.8. Samples in the picture are filled with blue dyed alginate for the purpose of showing.
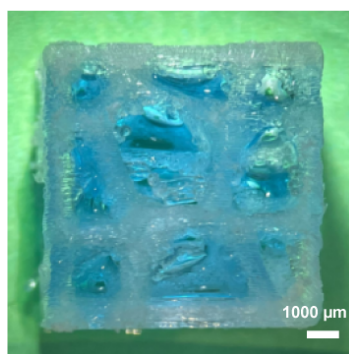
Figure 2.11. Voronoi 25 points distance 0.8 used for filling GelMA-collagen-0.5% BG. Sample in the picture are filled with blue dyed alginate for the purpose of showing.

2.2.8.3   Sample Fixation

The hFOB cells seeded 3D PLA scaffolds and hydrogels, were fixed with 4% (w/v) paraformaldehyde at room temperature for 15min, rinsed with PBS,

In order to SEM analysis the fixed samples are kept in Piperazine-N, N'-Bis (ethanesulfonic acid) (PIPES) buffer for at least one day, rinsed three times with distilled water and dried at 37 ºC overnight.

2.2.8.4   In vitro Cell Viability

2.2.8.4.1   Live-dead assay

The PLA scaffolds with cells were transferred to clean wells, and 500 μL of live/dead assay solution in DMEM/F-12 growth medium (Calcein 0.5 μL, Ethidium homodimer 2 μL in 1 mL of medium (according to the protocol provided by the manufacturer company)) was added to the plates with disk-shaped scaffolds, 250 μL for hydrogels and 2 mL for 3D printed scaffolds. The samples were incubated for 15 min (hydrogels for 30 min in dye and 10 min in PBS to remove the excess dye) and imaged by Confocal laser scanning microscopy (CLSM) (Zeiss LSM800, Germany).

This assay was done on days 1, 7, 14 for disk-shaped scaffolds and on days 1, 4, 7, 14, and 21 of culturing for hydrogels.

2.2.8.4.2 Alamar Blue Assay

Viability of hFOB cells on the scaffolds was determined by Alamar blue assay. Pen-Strep solution (1%) and Alamar blue (10%) were added to DMEM/F-12 DMEM without phenol red free media to prepare Alamar blue solution. The solution was filtered with 0.22 μm filters. The samples were placed in Alamar blue solution (1 mL) and incubated for 90 minutes at 37°C. Reduced solution was transferred (250 μL) into black bottom 96 well plates. The color change was detected at excitation of 545 nm and emission of 590 nm using Elisa microplate reader (Molecular Devices, USA) at room temperature. The fluorescence intensity was measured on days 1, 7, 14 and 21 for disk-shaped scaffolds and on days 1, 4, 7, 14, and 21 for hydrogels. The data were normalized to blank PLA in growth media and blank GelMA in growth media, and the results were expressed as fluorescence intensity versus time (days) for six repeats (n=6) [3].

2.2.8.4.3 Phalloidin-DAPI Staining

Adhesion of cells to the scaffold was analyzed by phalloidin-dapi staining. Phalloidin dyes the actin cytoskeleton and 4',6-diamidino-2-phenylindole (DAPI) dyes nucleus. Samples were fixed with 4% (w/v) paraformaldehyde previously. Following fixation, the cell membranes were permeabilized with Triton X-100 solution (1% v/v in PBS, pH 7.4) for 5 min and incubated at 37°C for 30 min in immunocytochemistry (ICC) blocking buffer to prevent non-specific binding. The samples were washed with dH_2O and incubated with Alexa Fluor 488 phalloidin (1:200 in dilution buffer) for 1h at 37°C and then incubated with DAPI (1:1000 in PBS) for 10 min at 37°C.

2.2.8.5   Osteogenic Characterization

2.2.8.5.1   Alizarin Red Staining

Alizarin red staining is a low-cost common method to detect Ca deposition and mineralization in cellular matrix. Four sets of experiments with nine groups of samples were designed for disk-shaped samples. In the first set, no cells were seeded on the samples, but they were kept in the growth medium. In the second set, cells were seeded on the samples and until day 21 they were cultured in growth media. In the third set of experiments, the cells were seeded on the specimens and cultured in the osteogenic medium. After seeding 1×10^5 cells/sample on the disk-shaped samples and culturing them for two days in the growth medium, the medium was replaced with the osteogenic medium and cultured for 21 days. After switching to the osteogenic medium, on days 1 and 21, the specimens were fixed and stained with Alizarin red solution for 5 min, and finally washed with 0.01 M PBS before imaging. Finally, in the last set the 35×10^4 cells/samples are seeded. Images were obtained using Stereo CL 1500 ECO (Zeiss, Germany) in BIOMATEN, METU.

For cube-shaped (3D) samples totally 97×10^4 cells/sample were seeded on five faces of the cube (except the bottom face). They were cultured for days in growth media and fixed and stained as explained above.

For the gels, 3×10^5 cells/70 µL gel were seeded, and at days 1, 14, and 21 they were analyzed for alizarin red staining. The images were taken by fluorescence microscope Image.M2 (Zeiss, Germany) in BIOMATEN, METU.

2.2.8.5.2   Alkaline Phosphatase (ALP) activity

The alkaline phosphatase activity of the hFOB cells was determined by ALP experiment by changing p-nitrophenyl phosphate (pNPP) to p-nitrophenol. The hFOB seeded scaffolds were placed into the lysis buffer. After freeze-thaw at -80°C, cells on the samples were resuspended and transferred to the eppendorf tubes,

centrifuged at 8000 rpm. for 2 min. Then 100 μL of pNpp working solution was added to the 50 μL of supernatant and incubated for 1h at 37°C. The absorbance was evaluated with UV-Vis spectrophotometry at 405 nm. Different concentrations of 4-nitrophenol in distilled water were used as the calibration curve (Appendix B). The amount of enzyme activity was calculated from a calibration curve provided with given concentrations of p-nitrophenol.

To evaluate DNA concentration in the solution, 50 μL of supernatant was mixed with 50 μL of Picogreen reagent in TE (Tris-EDTA) buffer by 500x dilution. It was Shaked under 120 rpm on an orbital shaker for 10 min. The device was set on fluorescence reading and read under 485 nm excitation and 538 nm emission. 0, 50, 75, 100, 25, 500, 750, and 1000 ng/mL of λ DNA standard was used as the calibration curve (Appendix C). The DNA concentration in the samples was measured via calibration curve and ALP level was normalized to DNA concentration. ALP activity test was performed for cell-laden disk-shaped samples in growth media.

Lysis buffer: To make lysis buffer 1% Triton X-100 was added to CB buffer, which is 0.2 M sodium carbonate mixed with 0.2 M sodium bicarbonate in 2:1 volume ratio and pH set to 10.2.

PNPP working solution: pNPP working solution is a 10% cofactor buffer $(100\ mM\ MgCl_2.6H_2O)$ in P-nitrophenyl phosphate liquid substrate system and diluted by 1 vol:2 vol water.

TE buffer: 10 mM Tris(hydroxymethyl)aminomethane (Tris) and 1mM Ethylenediamine tetra acetic acid (EDTA) were dissolved in distilled water and pH was set to 7.5 with 1M HCl.

ALP Activity for GelMA:

In this case, before putting lysis buffer, gels were treated with collagenase type II (4 mg/mL) in PBS in eppendorf tubes, and they were kept at 37°C for 30 min to dissolve the gels and take out the cells. After centrifuging at 13000 rpm. for 2 min, the supernatant was discarded, and lysis buffer was put on the pellet. The rest of the procedure is the same as disk-shaped samples described in previous section.

All the results were normalized by GelMA and PLA blank samples and the ALP activity is calculated through concentrations of (p-nitrophenol/60* DNA concentration)×1000.

2.2.8.5.3 Immunofluorescence

In this process, samples were fixed with 4% (w/v) paraformaldehyde solution. They were permeabilized with Triton X-100 solution (1% v/v in PBS, pH 7.4) for 5 min. Then, incubated at 37°C for 30 min in immunocytochemistry (ICC) blocking buffer to prevent non-specific binding. Samples were stained for confocal microscopy. For osteocalcin, osteopontin, collagen type I and osteonectin imaging, antibodies specific to these proteins (anti-osteocalcin ab13418 antibodies anti-osteopontin ab8448, anti-collagen type I ab138492, Abcam, UK and anti-osteonectin 335500, Invitrogen, USA) were used with 1:2, 1:10, 1:1000 and 7 μg/mL dilutions, respectively, at 4°C overnight. The first set of samples were incubated with anti-osteocalcin and anti-osteopontin and the second set of samples were incubated with anti-osteonectin and anti-collagen type I.

These primary antibodies were tagged with Alexa Fluor 488 goat anti-mouse (first set) and Alexa Fluor 555 goat anti-rabbit (second set) at 1:200 dilutions, for 1 h at 37°C. Samples were, finally, stained with DAPI (1:1000, 15 min, RT) at 37°C. Samples were imaged with Zeiss LSM 800 Confocal microscope with 405 nm, 488 nm, and 555 nm lasers.

Intensity analysis was measured using Image J FIJI and the signal was normalized to area. Two Way ANOVA and Sidak post hoc comparison tests were performed for statistical analysis.

2.2.8.5.4 Energy-Dispersive Spectroscopy (EDS)

EDS is an analytical method to characterize the elements and chemical compositions. This technique is based on the interaction between electron beam excitation and sample. The elements such as Calcium, Phosphate, and Silica present on the samples can be determined using this method. The disk-shaped nontreated, treated with NaOH (0.05, 0.5, and 5 M), and treated with collagen and collagen-BG (1%, 5%, 10%, and 15% (w/v)) samples with hFOB cells were fixed on days 1 and 21. They were coated with a layer of carbon and EDX was analyzed during SEM characterization by QUANTA 400F Field Emission SEM in Central Laboratory, METU.

2.2.9 Statistical Analysis of the Data

The whole quantitative data in this thesis were represented as mean ± standard deviations with $n \geq 3$. Ordinary one-way ANOVA and two-way ANOVA tests were done. P value is considered as difference between means and P<0.05 assessed as statistically significant.

CHAPTER 3

RESULTS AND DISCUSSION

3.1   Scaffold Preparation and Characterization

3.1.1   3D printed PLA Scaffold Design and its Effects on Structural and Mechanical Properties

The designed geometries for the scaffolds through CAD are presented in this section. The stereo images of printed geometries from the top and side view are presented in Figure 3.1.

For the mechanical properties, first the force-displacement data obtained from the mechanical compression test were converted to stress-strain and then Young's modulus and yield point are calculated via the method explained in the methods chapter. Figures 3.2a and 3.2b show the force-displacement and stress-strain curves for the specific geometry.
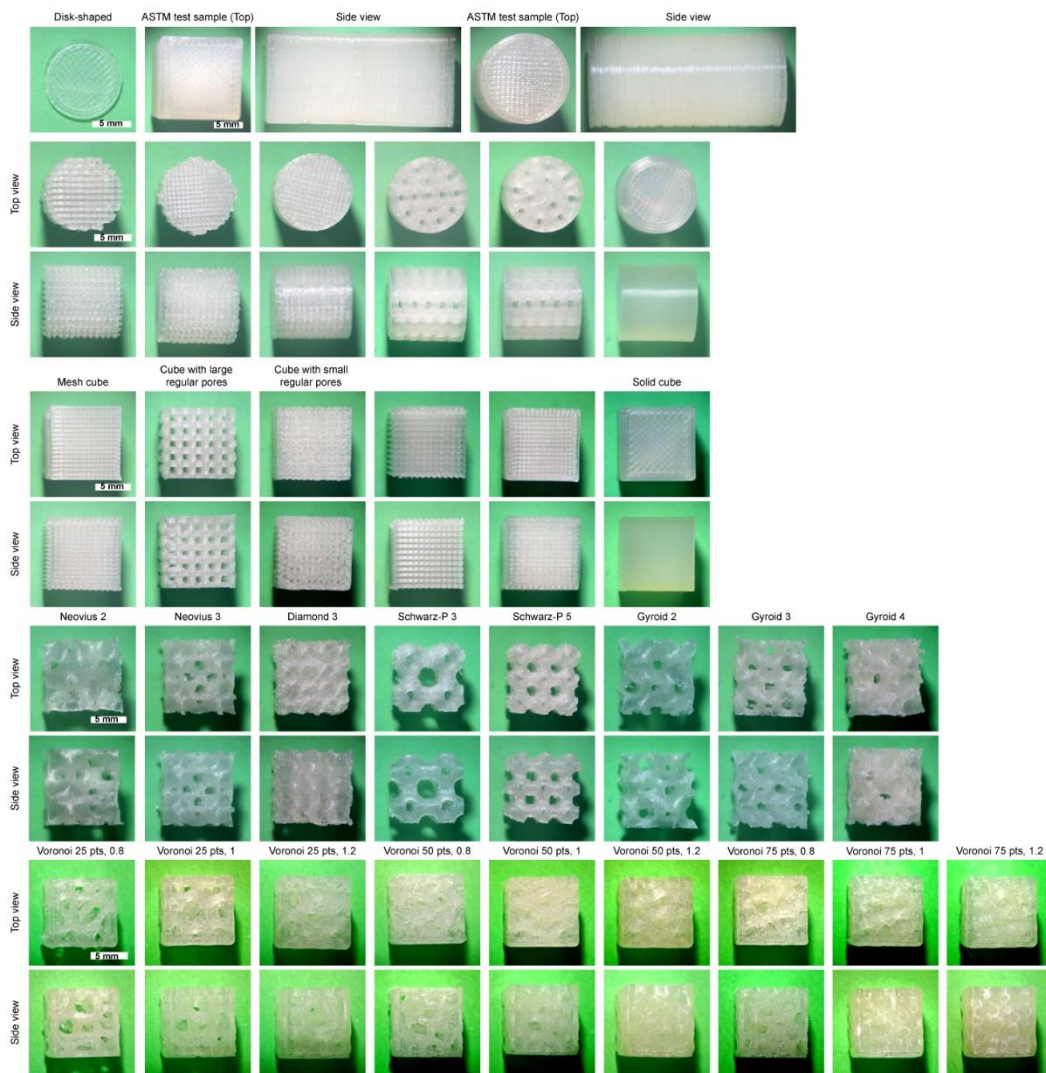
Figure 3.1. Stereo photos of printed geometries from PLA.
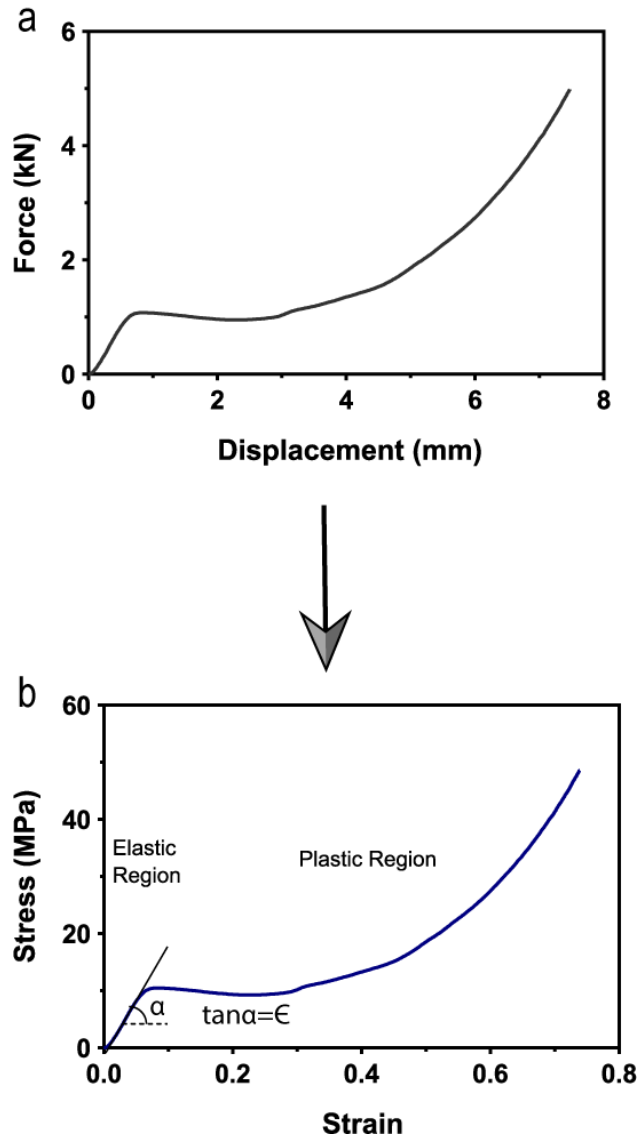
Figure 3.2. Force-displacement (a) and corresponding stress-strain curve (b) of mechanical compression test for Voronoi 50 points 0.8 distance.

Table 3.1 summarizes the geometries, their theoretical porosity and pore size, Young's modulus, and yield strength for different geometries designed for this study. For some of the structures, calculating theoretical pore size was impossible since they have irregular shapes (no. 16-32).

The results are shown as mean elastic modulus and yield strength for three repeats of each geometry. Table 3.1 shows 32 different geometries of which 28 were designed specifically for bone scaffold purpose. Four of them (Number 2-5) were

designed just for mechanical characterization as ASTM standard requirements for compression test. Numbers 1-5 has 0 pore size and 100% infill density. The effect of porosity represented a major factor in mechanical strength. Also, two different nozzle sizes (0.25 and 0.4 mm) were used to 3D print the scaffold by the fused deposition method. For some of the designs, 0.4 mm nozzle was not possible for printing. Therefore only 0.25 mm one was used (no. 6, 10-15, and 25-32). The results showed that the porosity and pore size are inversely, and the nozzle size is directly proportional to the mechanical properties. However, for some geometries (no. 7, 16 and 21) by decreasing the nozzle size, the Young's modulus increased, which is not a significant difference with larger nozzle size. This can be due to experimental errors. Cylindrical geometries showed higher elastic modulus than cubic ones with the same nozzle size, pore size, and almost the same porosity. Examples are no. 10 and 11, 12 and 13, 14 and 15. It was also observed that the fibrous structures have poorer mechanical properties than almost solid shapes (no. 10-15). Voronoi structures (no. 16-24) resembling the natural trabecular bone showed good mechanical strength. By increasing the seeding point and radius multiplier, the mechanical parameters increase significantly as expected due to decreased porosity. However, triply periodic minimal surfaces (no. 25-32) were weak in the compression test. Number 7, 22, 24, and 31 were used mainly for the in vitro tests since 7, 22 and 24 showed acceptable strength compared to native trabecular bone. Number 1 is used frequently, due to ease of fabrication and lower culture and production costs. The compression test was not done on this sample since it was 1 mm in height and not appropriate for compression test. Number 2-5 showed excellent strength, but lack of porosity was not suitable for bone scaffold purposes.

Table 3.1 Computer aided 3D designs, their porosity, pore size and mechanical properties.
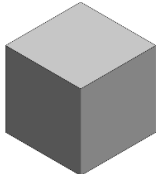
Number	Geometry	Name of the Geometry	Pore size (mm)	Porosity (%)	Nozzle size (mm)	Experimental Compressive Modulus Average (MPa) (SD)	Experimental Yield Stress Average (MPa) (SD)
1		Disk-shaped	0	0	0.4	-	-
2		Cube	0	0	0.4	1390.93 (34.37)	80.25 (1.46)
3		Cylinder	0	0	0.4	1807.5 (115.5)	87.6 (0.38)
4			0	0	0.4	1414.92 (544.7)	64.82 (19.1)
5			0	0	0.4	1291.06 (3.65)	54.8 (0.6)

Table 3.1 (cont'd) Computer aided 3D designs, their porosity, pore size and mechanical properties.
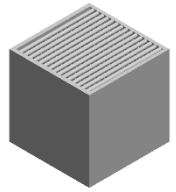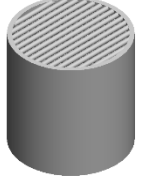
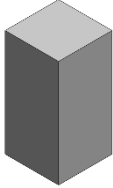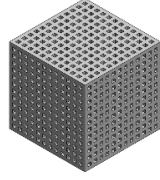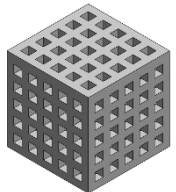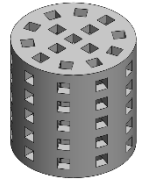|							
6		Cube with small regular pores	0.4	47.2	0.25	109.23 (21.08)	5.5 (0.82)
7		Cube with large regular pores	1	51	0.25	244.3 (12.14)	13.85 (0.52)
					0.4	237.72 (11.04)	13.12 (0.56)
8			1	37.9	0.25	308.43 (13.79)	17.5 (0.92)
					0.4	387.12 (12.67)	24.36 (0.81)
9			1	31	0.25	378.16 (5.45)	22.42 (0.92)
					0.4	425.49 (15)	26.89 (0.43)
10			0.2	37.9	0.25	222.77 (21.31)	14.53 (1.36)
11			0.2	39.2	0.25	287.26 (17.23)	15.35 (0.54)

Table 3.1 (cont'd) Computer aided 3D designs, their porosity, pore size and mechanical properties.
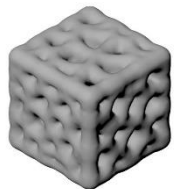
12			0.2	44.6	0.25	207.61 (20.17)	12.78 (1.18)
13			0.2	45.3	0.25	239.33 (34.45)	13.24 (0.42)
14		Mesh Cube	0.4	52	0.25	134.93 (4.65)	8.56 (0.47)
15			0.4	49.6	0.25	208.80 (12.17)	10.04 (1.01)
16		Voronoi 75pts Dist.1.2	-	17.2	0.25	504.5 (13.22)	44.1 (1.82)
					0.4	497.64 (5.40)	47.33 (0.28)

Table 3.1 (cont'd) Computer aided 3D designs, their porosity, pore size and mechanical properties.
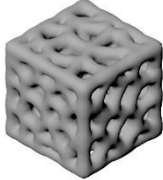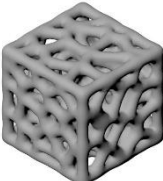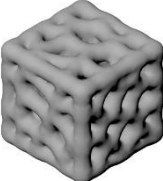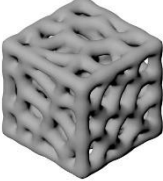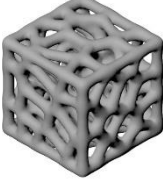
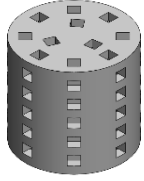|						
17		Voronoi 75pts Dist.1	-	28.5	0.25	359.04 (18.93)	28.28 (0.79)
					0.4	441.25 (25.46)	34.97 (0.2)
18		Voronoi 75pts Dist.0.8	-	45.1	0.25	237.67 (12.86)	15.41 (0.77)
					0.4	274.96 (6.99)	16.7 (0.23)
19		Voronoi 50pts Dist.1.2	-	26	0.25	325.34 (4.59)	29.38 (0.51)
					0.4	416.73 (14.44)	37.73 (0.66)
20		Voronoi 50pts Dist.1	-	39.2	0.25	296.62 (10.09)	20.16 (0.34)
					0.4	306.85 (12.02)	20.83 (0.46)
21		Voronoi 50pts Dist.0.8	-	55.3	0.25	196.9 (1.67)	10.55 (0.95)
					0.4	178.06 (5.33)	10.22 (0.26)

Table 3.1 (cont'd) Computer aided 3D designs, their porosity, pore size and mechanical properties.
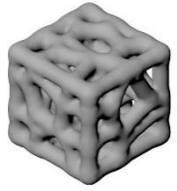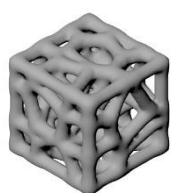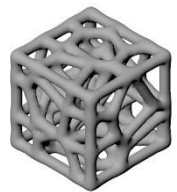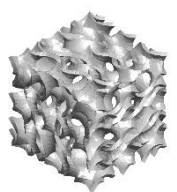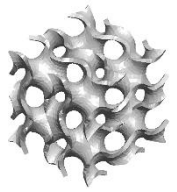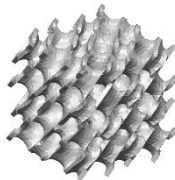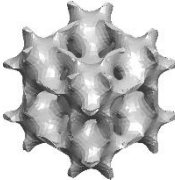
22		Voronoi 25pts Dist.1.2	-	42.8	0.25	258.29 (5.43)	16.84 (0.56)
					0.4	291.77 (7.52)	19.47 (0.31)
23		Voronoi 25pts Dist.1	-	55.5	0.25	200.07 (6.03)	10.73 (0.55)
					0.4	202.83 (16.13)	11.48 (0.28)
24		Voronoi 25pts Dist.0.8	-	70.6	0.25	118.32 (5.52)	4.38 (0.08)
					0.4	127.37 (11.71)	4.79 (0.07)
25		Gyroid 4	-	76.1	0.25	113.83 (14.65)	7.11 (0.39)
26		Gyroid 3	-	80.3	0.25	55,68 (1.15)	2.84 (0.05)

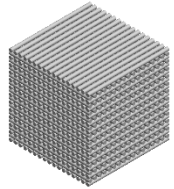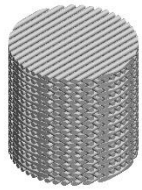Table 3.1 (cont'd) Computer aided 3D designs, their porosity, pore size and mechanical properties.

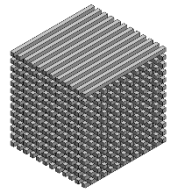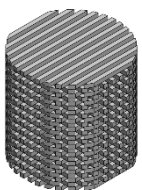| 27		Gyroid 2	-	84.7	0.25	39.36 (8.63)	2.4 (0.09)
28		Diamond 3	-	75.9	0.25	87.59 (1.3)	4.91 (0.59)
29		Neovius 3	-	75.4	0.25	112.8 (1.35)	4.73 (0.14)
30		Neovius 2	-	81.7	0.25	66.34 (5.22)	3.17 (0.19)
31		Schwarz-P 5	-	76.4	0.25	104.04 (4.20)	4.54 (0.25)
32		Schwarz-P 3	-	82.5	0.25	48.68 (11.74)	1.84 (0.45)

3.1.2 Scaffold Degradation Experiment

3.1.2.1 Weight Loss of PLA Scaffolds in PBS

The first set of samples was placed in PBS as a degradation medium. Six different geometries (no.2, 16, 19, 20, 21 and 24) due to their porosities were selected. Five replications per group were tested for PBS degradation for 120 days. The results showed no significant difference in weight after four months. Figure 3.3 represents the weight loss (%) for different days. The slightly negative value here indicates measurement errors due to not drying completely. However, these results were predictable due to known slow degradation and previous reports on PLA in the literature [220], [221]. It was reported in these studies that the degradation rate of PLA in PBS is very low, and it takes more than six months to observe a considerable loss in weight.
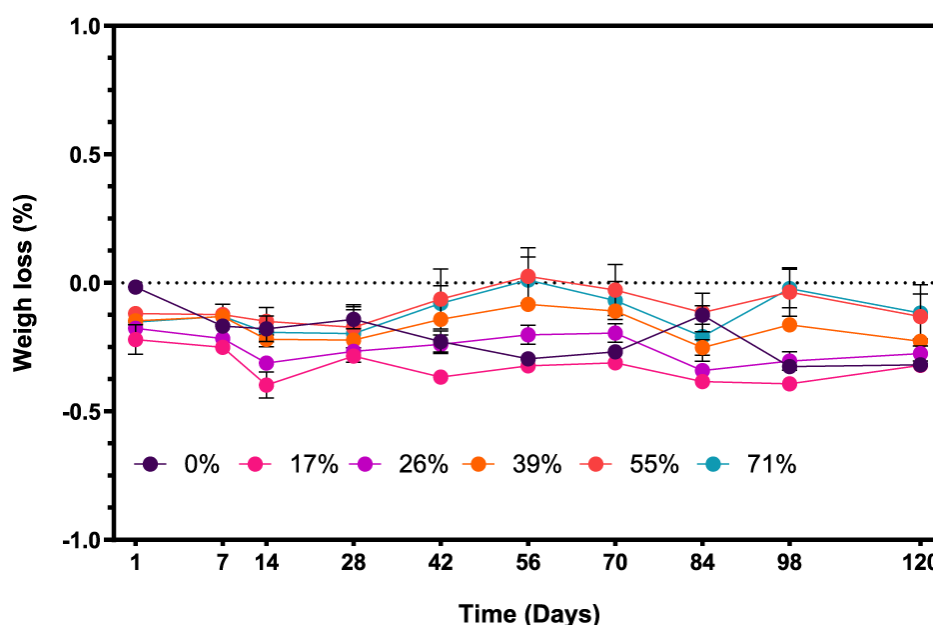
Figure 3.3. Wight loss of PLA scaffolds in PBS as a degradation media. 0%, 17%, 26%, 38% and 71% porosities represent cube, Voronoi 75 points distance 1.2, Voronoi 50 points distance 1.2, Voronoi 50 points distance 1, Voronoi 50 points distance 0.8 and Voronoi 25 points distance 0.8 respectively.

3.1.2.2   Weight Loss of PLA Scaffolds in Enzymatic Degradation Media

Enzymatic degradation is an accelerated way of degradation which is carried out by the proteinase K enzyme. For this experiment set, two-time points of 5 and 10 days and 5 groups of designs (no.2, 19, 20, 21 and 24) (3 replica/group) were assigned. The geometries were chosen according to their porosities. Also, the control groups (medium without enzyme) were added to the set. The results are depicted below (Figure 3.4a & 3.4b). Figure 3.4a shows the weight loss for different groups and compares them with control groups. The ordinary two-way ANOVA test (Tukey's multiple comparisons) reported no significant difference between 5- and 10-days control groups for each set of data (porosity). However, the difference between data for all other groups in each structure was statistically significant (∗∗∗∗) with P≤0.0001. P≤0.05 is considered as statistically significant. So, the weight loss between enzymatic degradations and their control counterparts and between 5 and 10 days of the enzymatic experiment is considerable. Figure 3.4b shows the increasing degradation trend by increasing the porosity and differences between 5 and 10 days of degradation with the enzyme. The influence of proteinase K is significantly high when we compare degradation of PLA in 10 days in enzyme with 120 days in PBS. Since there are also enzymes in the human body, it is expected that the PLA scaffolds can be expected to degrade by time and substituted by new tissue. According to literature its degradation debris is absorbed and excreted without leaving any trace [80].
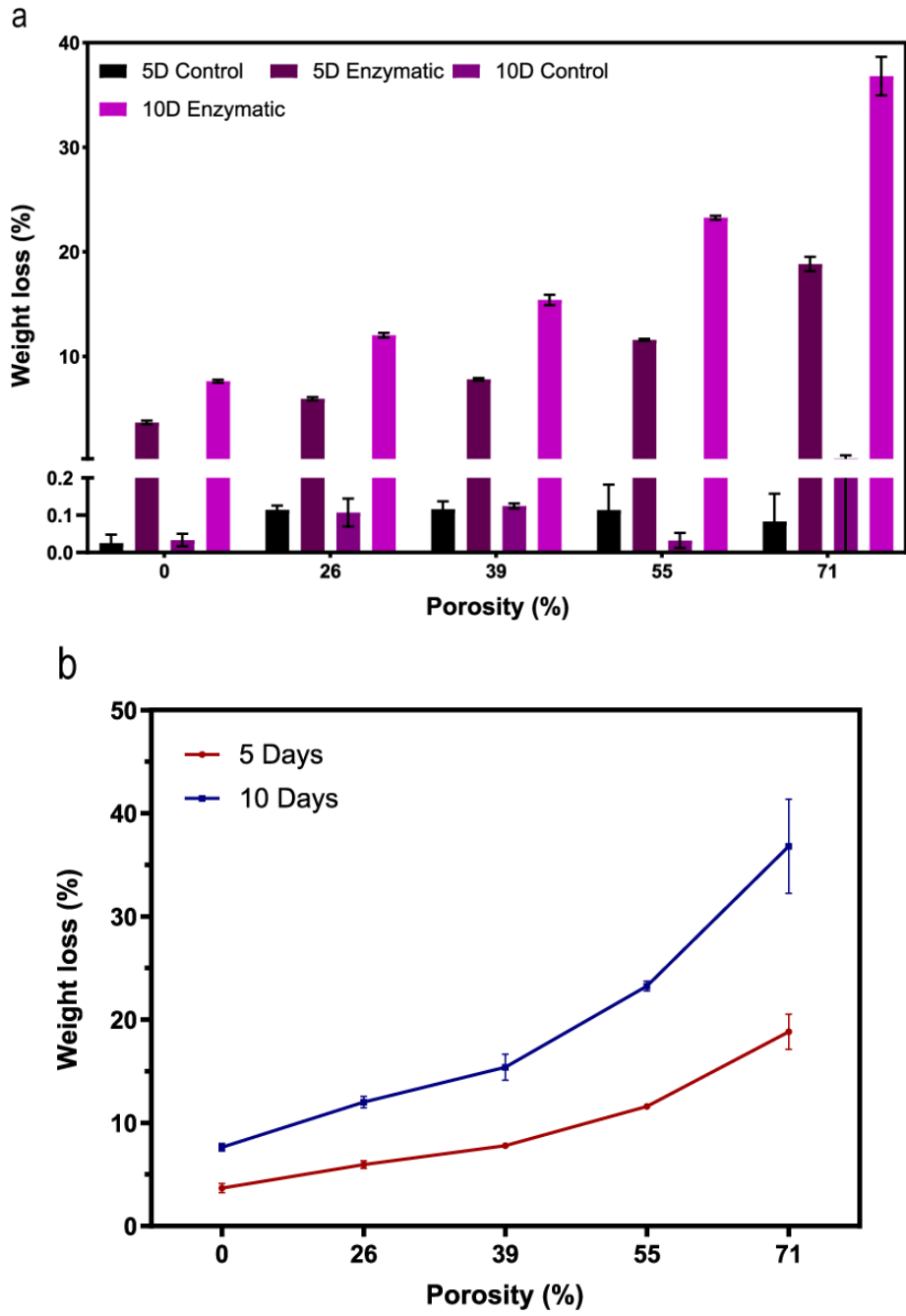
Figure 3.4. Weight loss of enzymatically degraded scaffolds. a) Shows the weight loss (%) for and 5 groups of samples in 5 days of control and enzymatic media and 10 days of control and enzymatic media. The SD differences were significant for all the groups with each other and inside each set for except control groups. b) Presents the weight loss (%) vs. porosity (%) for 5 and 10 days in an enzymatic degradation.

3.1.2.3 Mechanical Characterization of Enzymatically Degraded Scaffolds

The mechanical characterization was done for degraded groups and their control ones and compared with their non-treated counterparts. Figures 3.5a and 3.5b are the graphical statistics showing the elastic modulus and yield points, respectively. Despite the significant weight loss for each group of porosity, the compression test results showed no considerable variation for Young's modulus and yield strength. For the Young's modulus (Figure 3.5a) of 26% to 71% porosity except for the ones indicated in the figure, the statistical data showed no significant variation. For 0% the non-treated versus 5 days and 10 days of control and also 5 days versus 10 days control showed less variation and except these groups and 5 days and 10 days of enzymatic treatment (∗), the rest were significant with a P value less than 0.0001 (∗∗∗∗).

The yield stress measurement differences were non-significant except for the groups, as shown in Figure 3.5b. Calculation of yield point for 0% porosity was not possible since the load cell of the mechanical test device was not suitable for testing 100% infill solid cube. Furthermore, Table 3.2 summarizes the weight loss (%), elastic modulus (MPa), and yield strength (MPa) before and after degradation of 5 and 10 days for various porous scaffolds. The results show that by increasing the porosity, the degradation effect on the mechanical properties becomes less sensible.

Clearly, by increasing the incubation time in the enzymatic medium, porosity will become more apparent.
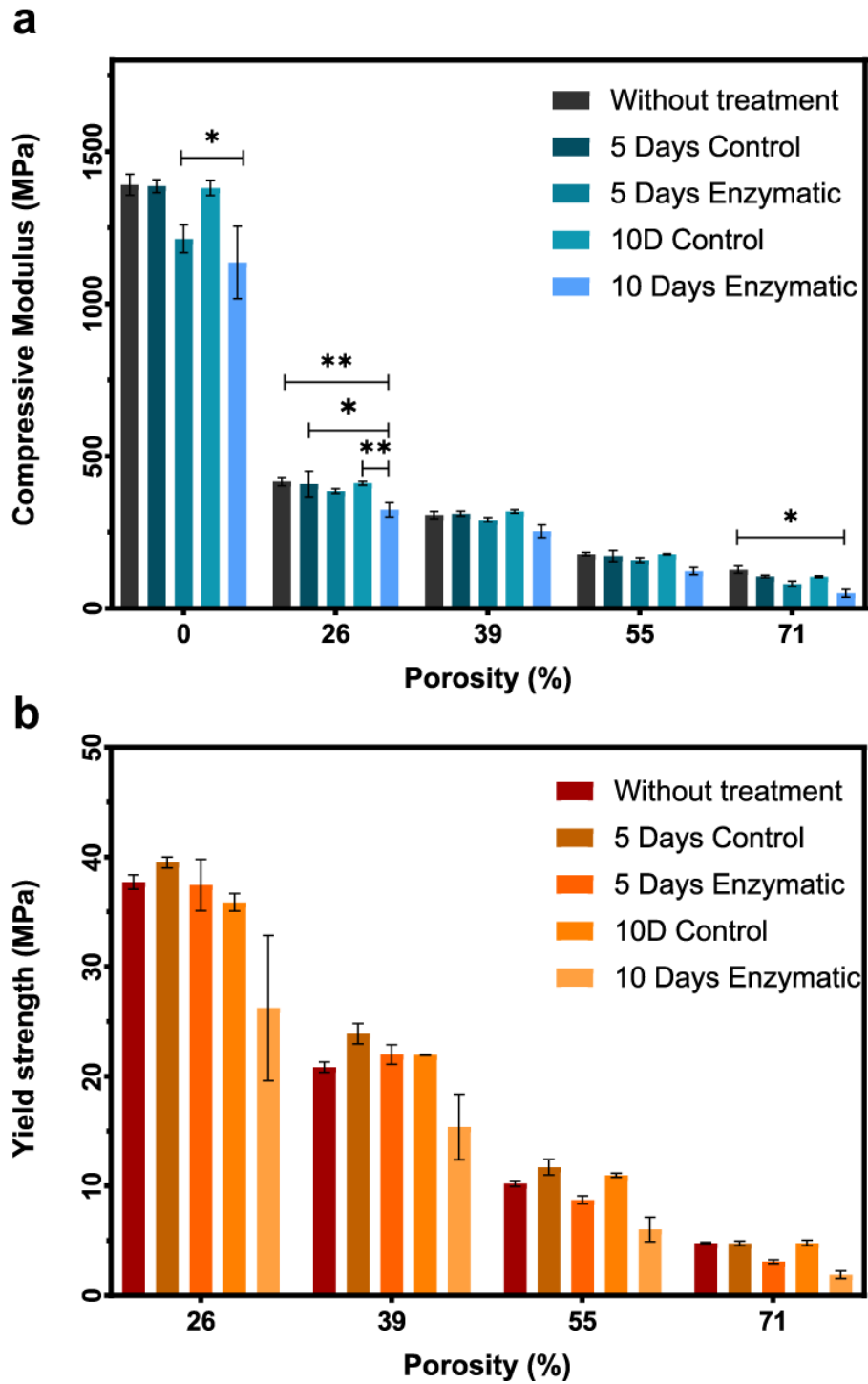
Figure 3.5. Mechanical characterization of degraded scaffolds. a) Compressive modulus and b) Yield point for different porosities of PLA scaffolds before and after weight loss for 5 and 10 days and their control groups. ∗∗∗∗ indicates P≤0.0001, ∗∗∗ means P≤0.001. ∗∗ shows P≤0.01 and finally ∗ means P≤0.05.

Table 3.2 Porosity, weight loss and mechanical properties for PLA scaffolds after enzymatic degradation.

Porosity (%)	Weight loss (%) after 5 days of ED (SD)	Weight loss (%) after 10 days of ED (SD)	CM before ED (MPa) (SD)	CM after 5 days of ED (MPa) (SD)	CM after 10 days of ED (MPa) (SD)	YS before ED (MPa) (SD)	YS after 5 days of ED (MPa) (SD)	YS after 10 days of ED (MPa) (SD)
0	3.68 (0.18)	7.63 (0.15)	1390.93 (34.37)	1213.66 (46.04)	1135.66 (119.09)	80.25 (1.46)	-	-
26	5.95 (0.15)	12.02 (0.23)	416.73 (14.44)	385.52 (7.69)	323.77 (22.74)	37.73 (0.66)	37.44 (2.35)	26.22 (6.62)
39	7.81 (0.19)	15.4 (0.5)	306.85 (12.02)	291.543 (6.82)	253.31 (21.04)	20.83 (0.46)	21.98 (0.887)	15.37 (2.99)
55	11.59 (0.09)	23.26 (0.2)	178.06 (5.33)	158.75 (7.42)	122.45 (11.96)	10.22 (0.26)	8.72 (0.35)	6.03 (1.12)
71	18.84 (0.69)	36.81 (1.84)	127.37 (11.71)	80.87 (9)	50.12 (12.95)	4.79 (0.07)	3.1 (0.18)	1.9 (0.35)

ED: Enzymatic Degradation, CM: Compressive Modulus, YS: Yield Stress.

3.1.2.4 Surface Characterization of Degraded Scaffolds

The Figures 3.6a and 3.6b are the scanning electron microscopy of the degraded scaffold and their control groups and before degradation for five groups of porosities. It can be observed that the surface morphology of the scaffolds changed notably. Figure 3.6a shows 1000 times magnification and 3.6b is composed of two different magnifications; small images 200× and larger ones are with 8000× magnifications. Some nano and microstructures appeared on the surface due to degradation when we compared the 5- and 10-days enzymatic degradation with their control counterparts and non-treated scaffolds. However, the difference is not negligible. Missing parts and also voids can be seen in porous structures after 10 days in an enzymatic medium, such as 71% porosity (Figure 3.6a). Comparing control groups with non-

treated surfaces also reveals some morphological changes on the surface, although it is not comparable with enzymatic degradation. This change in morphology eventually leads to weight loss and change in mechanical properties, as discussed before.
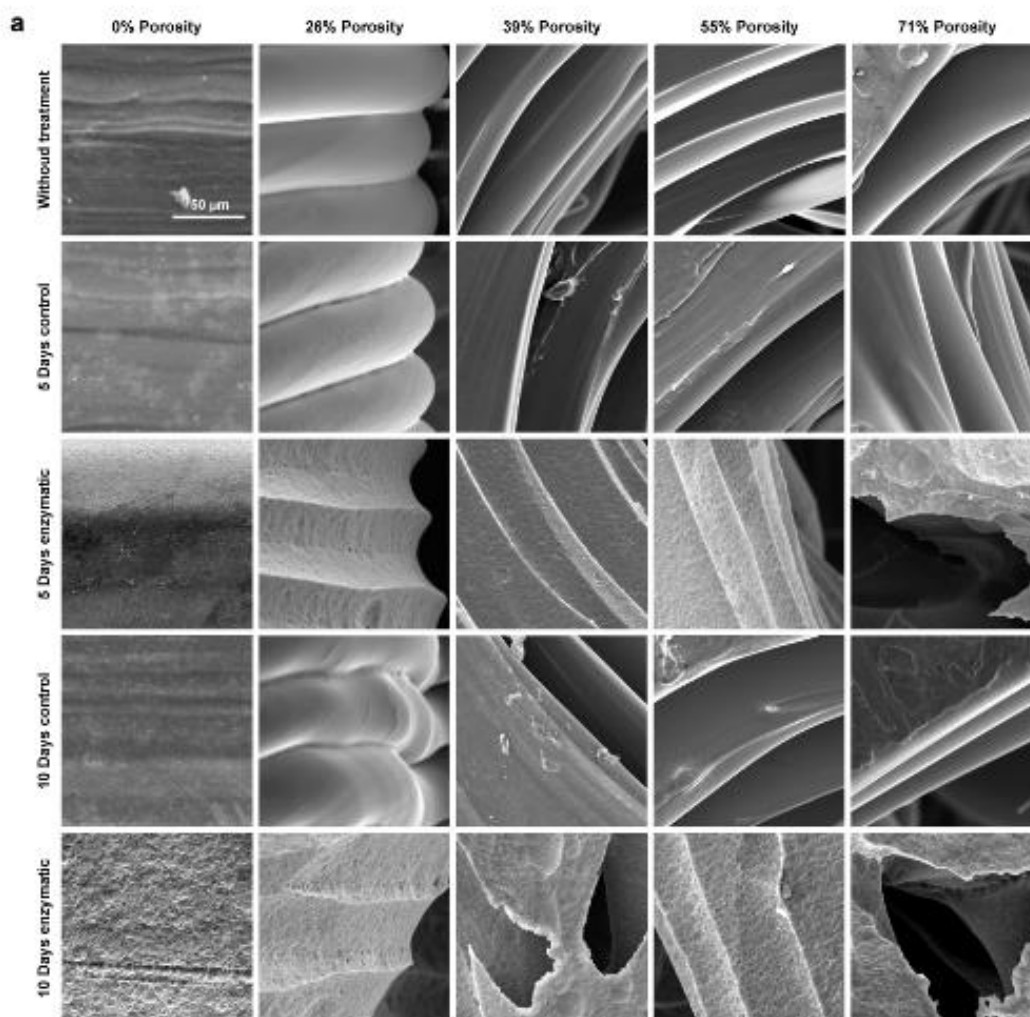
Figure 3.6. The SEM analysis of the degraded scaffold vs. their control groups and non-treated ones. a) Shows 1000× magnification and b) shows 200× for small images and 8000× for larger ones. Scale bar is the same for all images with the same magnification.
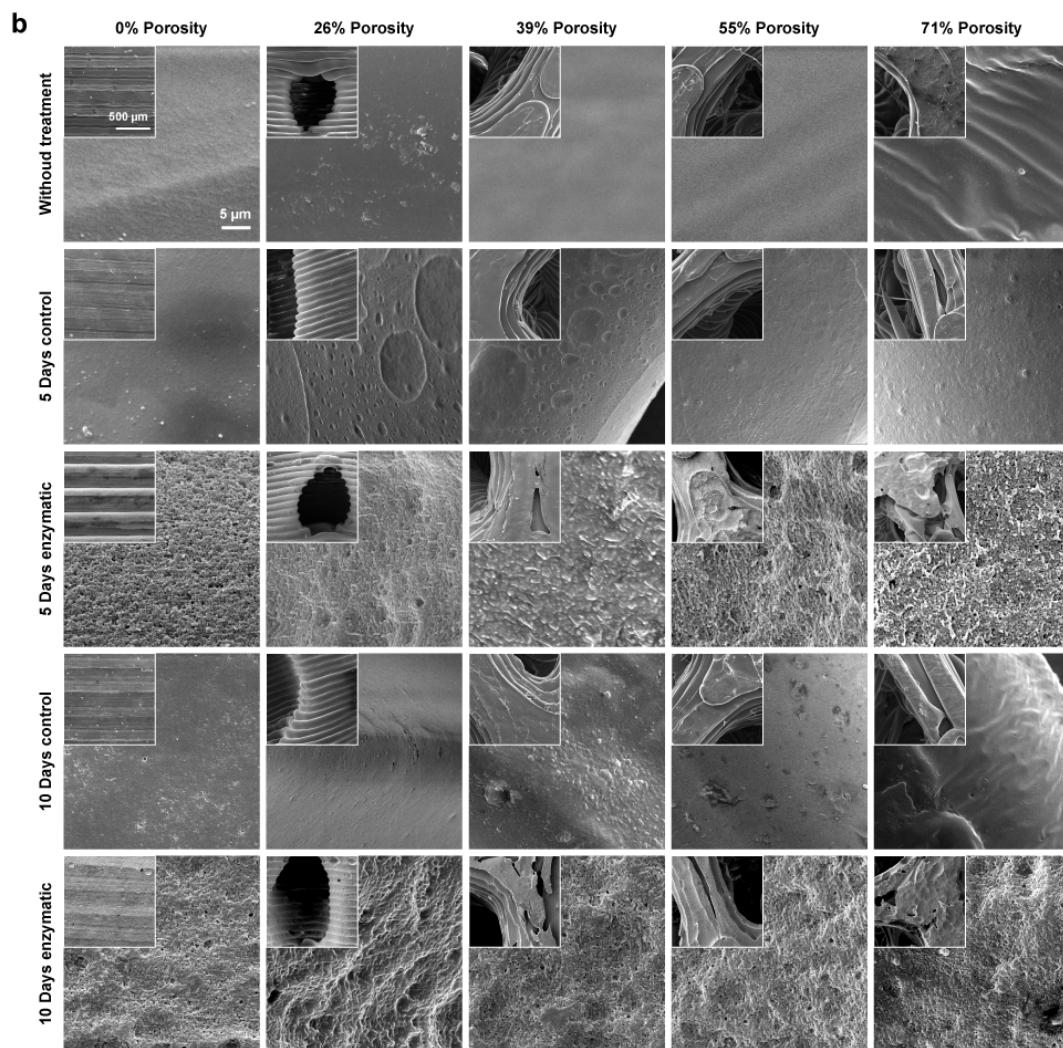
Figure 3.6. (cont'd) The SEM analysis of the degraded scaffold vs. their control groups and non-treated ones. a) Shows 1000× magnification and b) shows 200× for small images and 8000× for larger ones. Scale bar is the same for all images with the same magnification.

3.2 Bioglass Characterization

3.2.1 ICP-OES Results

The table below (Table 3.3) presents the inductively coupled plasma (ICP) - optical emission spectrometry (OES) results for bioglass 58S as weight %. The results show successful synthesis of bioglass 58S. However, slight variation between nominal values ($58SiO_2$-38 CaO-$4P_2O_5$(wt%)) [216], and synthesized one in the composition of Ca, Si, and P components, and subsequently, their oxidized version was observed. This deviation ($54SiO_2$-29 CaO-$7P_2O_5$ (wt%)) from theoretical values is inevitable in lab-scale synthesis due to conditions and some impurities that may influence the synthesis [222] and/or rapid gelation and precipitation [223].

Table 3.3 Theoretical and experimental values for the elements of bioglass 58S.

Elements	Si (wt%)	SiO_2 (wt%)	Ca (wt%)	CaO (wt%)	P (w%)	P_2O_5 (wt%)
Theoretical	27.07	58	27.17	38	1.74	4
Experimental	25.25±1	54	20.5±1	29	3.15±0.3	7

3.2.2 XRD Results

The X-ray diffraction pattern below (Figure 3.7) shows the glassy nature of the bioglass 58S. A widespread band illustrates the amorphous phase. A similar pattern can be seen in a study by Xia and Chang for the quick alkali-mediated synthesis of bioglass 58S [130]. Calcium silicate shows diffraction in XRD pattern with a maximum at 32˚ [224], [225]. The sharper peak was observed at 2θ=32˚ (shown by ∗) which can be due to partially crystallized calcium silicate (Ca_2SiO_2). Amorphous calcium silicate can crystalize at temperature around 800℃ or above [226]. Meiszterics et al. have reported similar peaks at lower temperatures [227]. Reheating

the BG to dry can be the reason of these broad peaks which appear similar to the amorphous glasses' classical behavior [228].
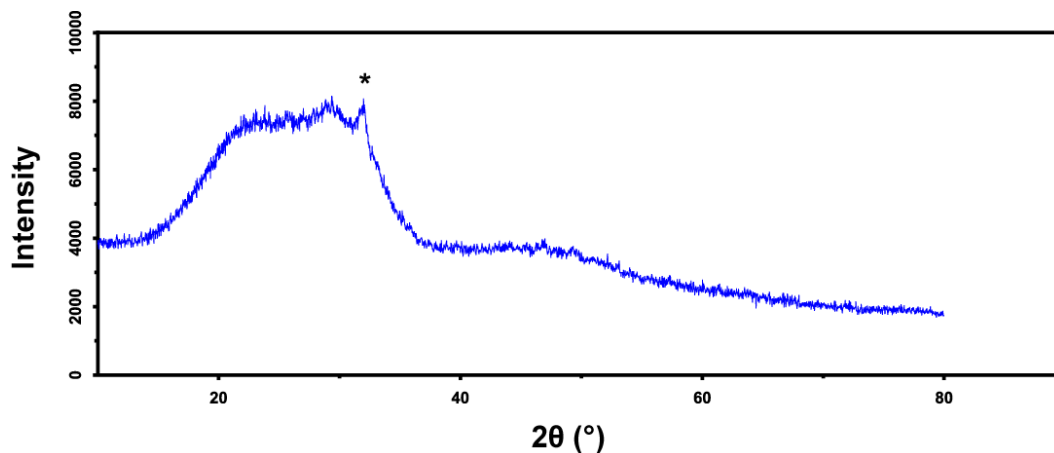
Figure 3.7. XRD pattern for bioglass 58S. * shows a sharp peak at $2\theta=32˚$.

3.2.3   TEM, SEM, and Particle Size Analysis

Transmission electron microscopy (Figure 3.8A) and scanning electron microscopy (Figure 3.8B-C) enlighten the spherical and amorphous morphology of the BG [215]. Accordingly, mostly round and homogeneous size particles were obtained. They tended to aggregate and form clumps in the dry state. The particle size (Figure 3.8D) of synthesized BGs obtained from the Zeta sizer demonstrated size distribution with an average particle size value as 120.2 ± 1.4 nm in a wet condition. The particle size for sol-gel derived powder is a function of many factors. The primary concentration of water and ammonia, alkoxide, and alcohol type are major factors influencing the size of the final product [229].

88
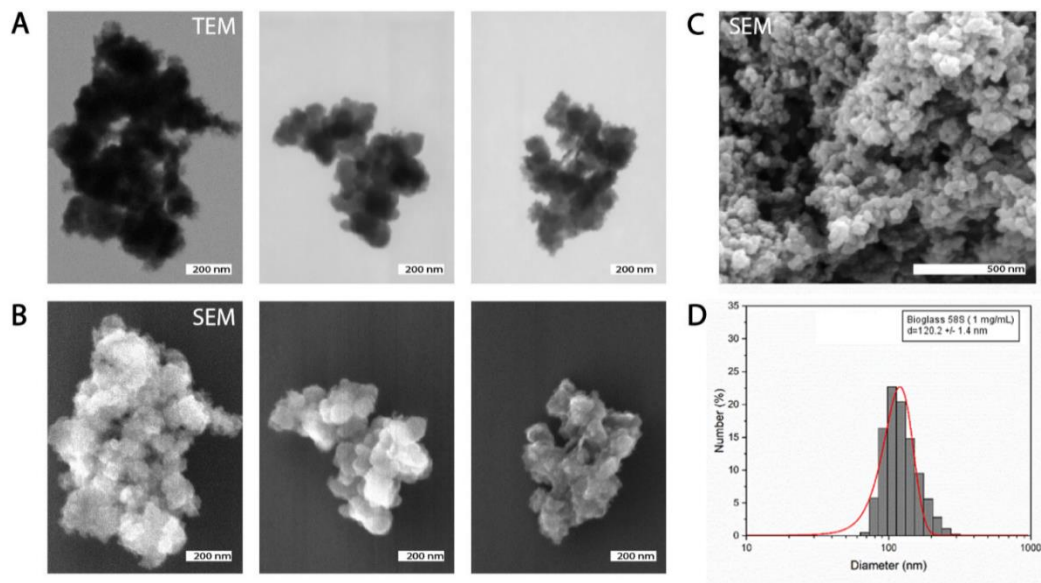
Figure 3.8. Characterization of BG. A) TEM, B and C) SEM, D) particle size analysis for BG 58S with zeta sizer.

3.3 Surface Characterization of Functionalized Scaffolds

3.3.1 Water Contact Angle and SEM Characterization for Alkali Treated Scaffolds

Figure 3.9a is a graphical representation for the water contact angle test for PLA without treatment, and for 0.05 M, 0.5 M and 5 M NaOH treated surfaces. The contact angle for PLA was $74.68°\pm7.1$, for 0.05 M treated PLA it was $96°\pm9.3$ and for 0.5 M treated it was obtained as $82°\pm8$ and finally for 5 M, the contact angle was $78.94°\pm11.5$. The one-way ANOVA results show a significant difference between PLA and 0.05 M treated PLA and between 0.05 M treated PLA and 5 M treated one. It can be concluded that the 0.05 M NaOH treated PLA is the most hydrophobic one among all. Alkali treatment imposes surface roughness, as it can be observed in Figure 3.9b (SEM results for the alkali-treated surfaces) [230]. For a hydrophobic polymer like PLA, increasing the surface roughness results in increasing the hydrophobicity [231], [232]. Nanoscale roughness can be seen in the first row of

Figure 3.9b for 0.05 M NaOH treated PLA, and by increasing the NaOH concentration, this roughness reaches detectable microscale roughness for 5 M treated one. Hydrophobicity is a requirement for protein adsorption through hydrophobic interactions between protein and surface [191].
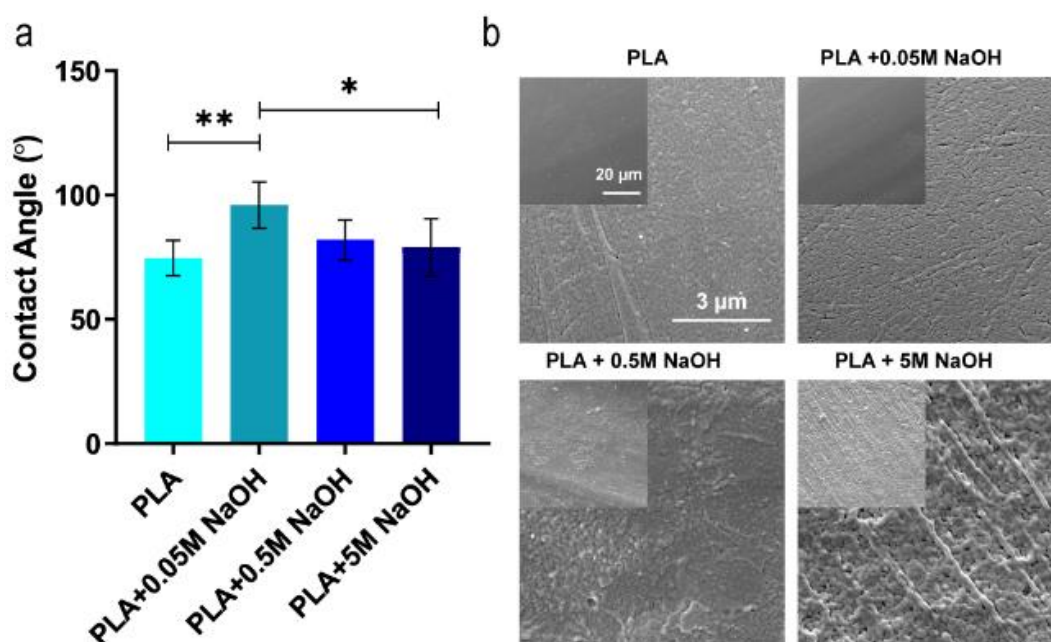
Figure 3.9. Water contact angle and SEM analysis for alkali treated scaffolds. a) Water contact angle for treated PLA scaffolds. b) SEM results for modifies surfaces. ∗∗ shows P≤0.01 and ∗ means P≤0.05. Small images are 4000× and larger ones are 30000× magnification.

3.4 Surface Characterization of Coated Scaffolds

3.4.1 FTIR-ATR Analysis of Collagen and Collagen-BG Coated PLA Scaffolds

FTIR analysis of PLA films with and without collagen as a coating shows that collagen was successfully coated on the PLA films (Figure 3.10a). Amide A. I, II,

and III bands which are dedicated to collagen did not exist on neat PLA films. However, these bands can be observed in collagen coated PLA films. Amide A band, the region between 3300-3400 cm^{-1} corresponds to N-H stretching. Amide I (1650-1660 cm^{-1}) is related to C=O peptide group. C-N stretching vibration and N-H bending contribute to the amide II band, which ranges between 1540-1555 cm^{-1}. Finally, the amide III is dedicated to stretching and bending vibrations of C-O and N-H at 1235 cm^{-1} absorption band [233], [234].

The intensity of the amide bands and sharper peaks, particularly amide I and II in 0.05 M NaOH treated PLA films indicates better and more collagen coating on this type.

The FTIR spectra for BG and collagen-BG coated PLA is represented in Figure 3.10b. The BG 58S powder FTIR pattern in this Figure shows the presence of Si-O-Si symmetric bending vibration in 450-470 cm^{-1}, and it is due to Si-O amorphous glass phase [235].

Another asymmetric Si-O-Si stretching band can be assigned to the region of 1000-1200 cm^{-1} [236]. Stretching vibration of Si-O group is detected in the absorbance range of 725-810 cm^{-1} [235]. Shoulder at 958 cm^{-1} Si-O-Ca [237]. The stretching around 1180 cm^{-1} belongs to P-O bond [238]. These bands can be seen in collagen-BG coated PLA rather than neat PLA or collagen-coated one. The amide bonds described above also exist in collagen and collagen-BG coated PLA. These results show the successful coating of collagen and Col-BG on PLA scaffolds.

a
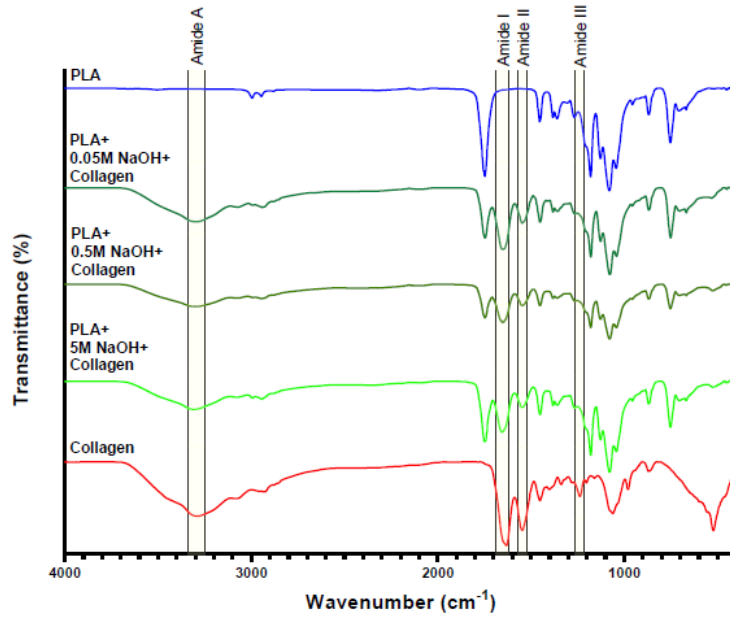
b
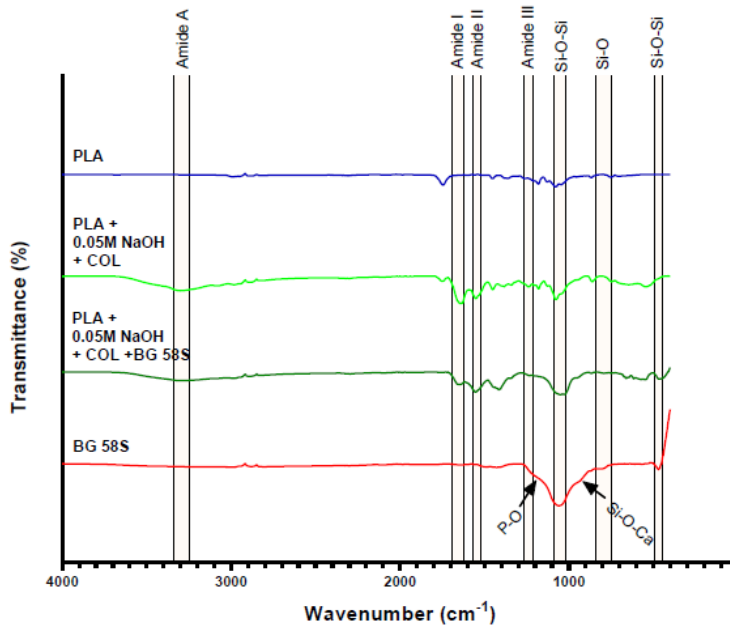
Figure 3.10. FTIR spectra. a) Alkali treated PLA with collagen coating. b) FTIR Spectra for BG and Col-BG coated PLA.

3.4.2 SEM Analysis of Alkali Treated, Collagen and Collagen-BG Coated Scaffolds

The SEM results are shown in Figure 3.11. As it is discussed before, alkali treatment changes the surface morphology by adding roughness which can be seen in the first row, by increasing the concentration of NaOH the surface roughness changes from the nanoscale to microscale.

The second row of the Figure shows the collagen coating on different alkali-treated PLA scaffolds.. The SEM results match the FTIR results in better coating of collagen on 0.05 M NaOH treated PLA scaffolds compared to 0.5 M and 5 M treated ones.
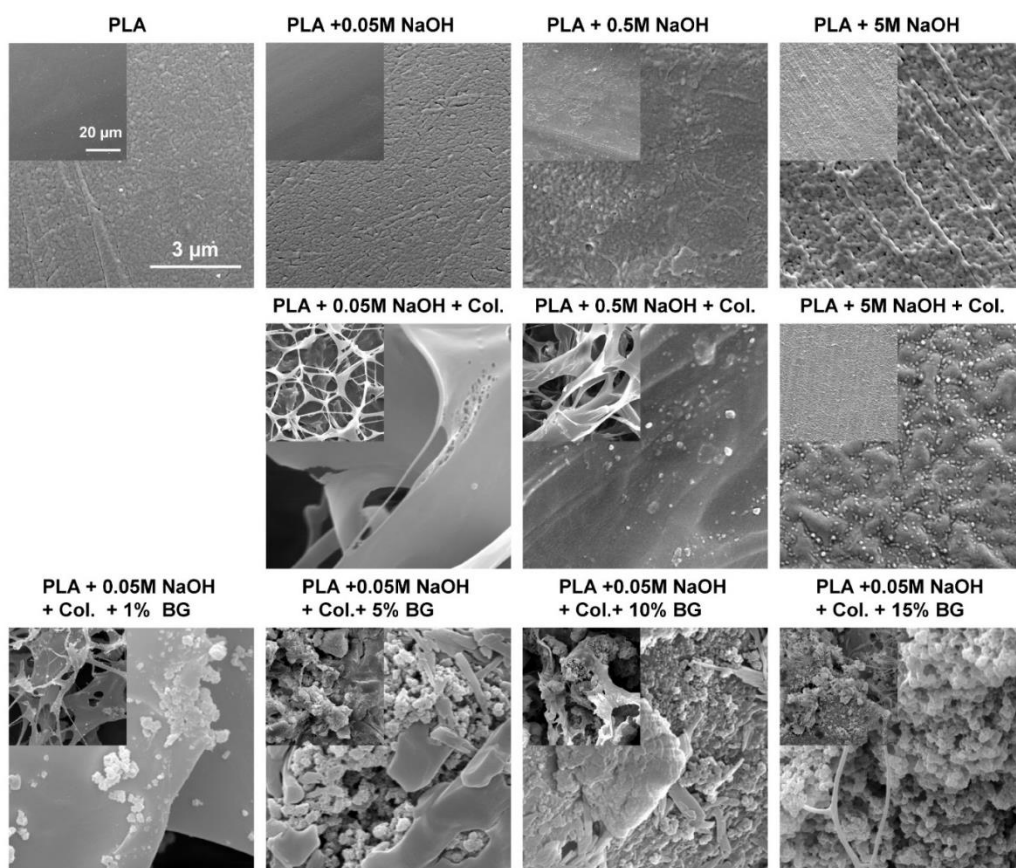
Figure 3.11. SEM analysis of alkali treated, collagen and collagen-BG coated PLA scaffolds. The scale bar is the same for images of the same size. Small images are 4000× and larger ones are 30000× magnification.

The third row of the Figure 3.11 characterizes the collagen-BG coated 0.05 M NaOH modified PLA. The spherical irregular particles are bioglasses. From left to right, the concentration of BG is increasing, which can be seen explicitly. Presence of BG in the coat decreased the smooth film-like coating appearance of the collagen.

3.4.3   Direct Red Staining of Coated Scaffolds for Collagen

The direct red staining for the presence of collagen as a coating on PLA scaffolds shows the successful coating of collagen. From Figure 3.12e to 3.12i are collagen-coated scaffolds. From a to d are PLA, 0.05 M NaOH modified, 0.5 M NaOH treated and 5 M alkali-treated PLA. From e to i all of the scaffolds are modified with 0.05 M NaOH. Images e to i show collagen-coated, Col.-1% BG, Col.-5% BG, Col.-10% BG, and Col.-15% BG coated PLA scaffolds. The red color proves the presence of collagen on the scaffolds. Accordingly coating of scaffolds in Figure 3.12 e -i suggests more intense and homogeneous distribution of collagen in the groups; 3.12 e and i. Thus, collagen coating could be considered as more effective either without or with high amounts of BG.
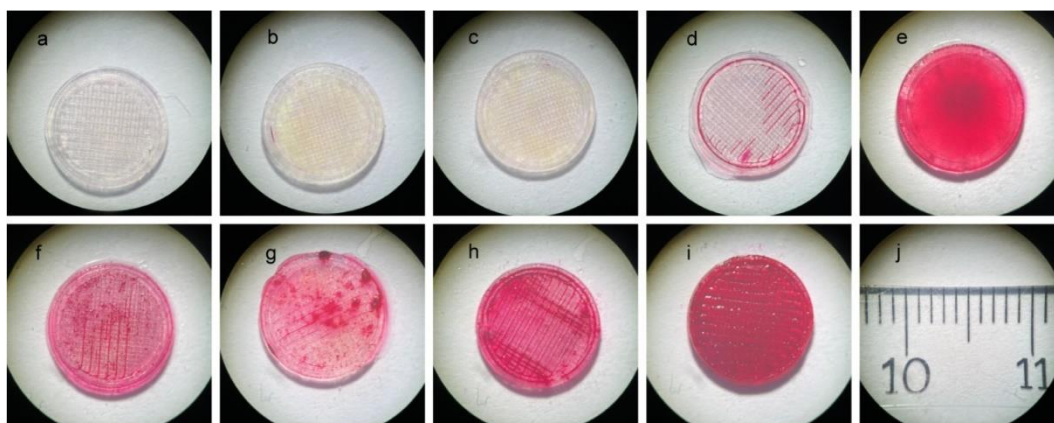
Figure 3.12. Direct Red Staining for Collagen. PLA (a), PLA + 0.05M NaOH (b), PLA + 0. 5M NaOH (c), PLA + 5M NaOH (d), PLA + 0.05M NaOH + Col. (e), PLA + 0.05M NaOH + Col. +1%BG (f), PLA + 0.05M NaOH + Col. 5%BG (g), PLA +

0.05M NaOH + Col. 10%BG (h), PLA + 0.05M NaOH + Col. 15%BG (i), Image scale (j).

3.5 Hydrogel Characterization Results

3.5.1 Mechanical Characterization of the Hydrogels

The mechanical test is done on the GelMA hydrogels. GelMA, GelMA with collagen, and GelMA with collagen and different concentrations of BG are tested under uniaxial compression. The stress-strain result for one of these groups is presented in Figure 3.13a. All the stress-strain curves were similar. The stress and strain are calculated from force and displacements results as described in the methodology chapter. The results of compressive modulus are shown in the Figure 3.13b. The results roughly match the literature [56]. The one-way ANOVA analysis shows no significant difference between the groups. This indicates that the mechanical strength of GelMA is independent of BG presence, at least in low concentrations. However, the concentration of GelMA [65], photo-initiator [66], the intensity of UV light, and crosslinking conditions [67] are the factors influencing the mechanical and swelling properties of the GelMA hydrogels.
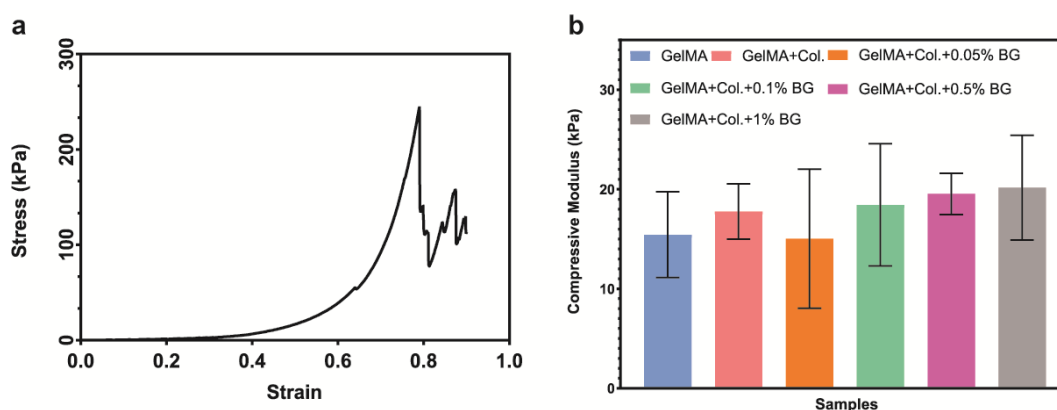
Figure 3.13. Mechanical characterization of GelMA. a) Representative stress-strain curve for GelMA b) Compressive modulus (kPa) for different hydrogel groups.

3.5.2 Hydrogel Swelling

The swelling ratio (%) of different hydrogels is represented as a time function (Figure 3.14). The hydrogel weights are measured after immersion in distilled water for 24 hours. GelMA without any additive represents the highest swelling ratio. The results show the dramatic increase in swelling during the first 3 hours. However, the swelling rate reaches almost steady state and saturated level in 24 hours. The swelling ratio decreases by increasing the concentration of BG. For the first 3 hours the swelling ratio for GelMA is approximately 2.5 times the GelMA with collagen and/or Col.-BG. A similar trend can be seen in Zuo et al. [239]. The difference between GelMA with other groups and GelMA/Col. with 0.05% BG and 1% BG are significant ($P<0.0001$). The difference between 0.1% BG and 1% BG is also significant with $P<0.05$. The others have no significant difference.
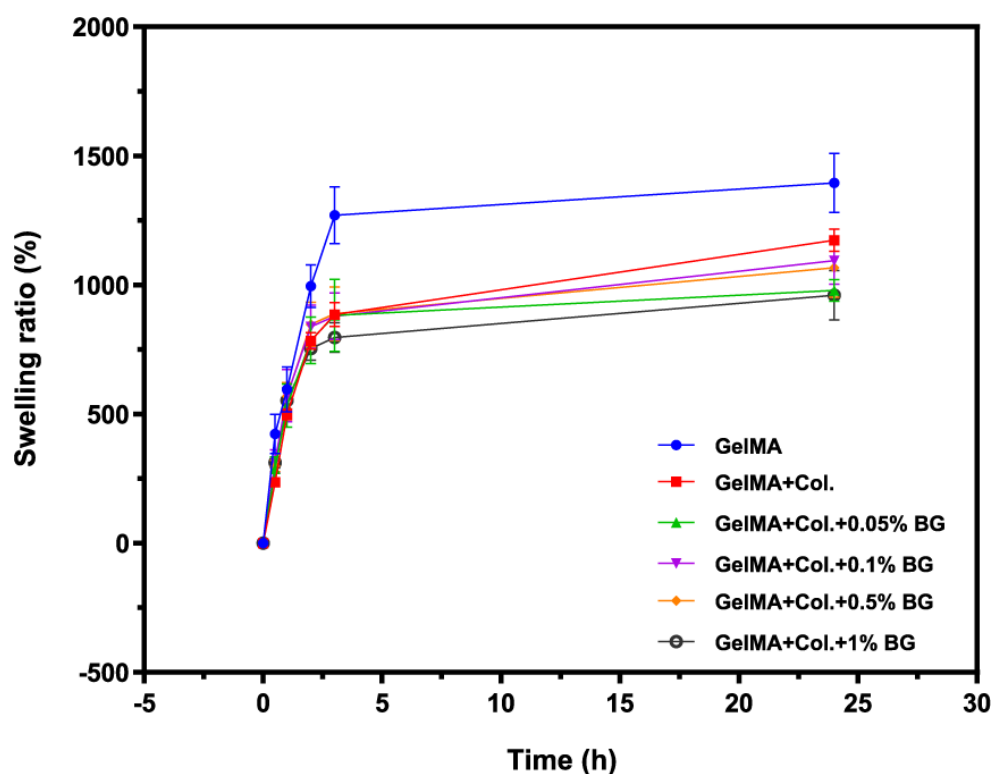
Figure 3.14. Swelling ratio (%) calculated for different time points during 24 hours.

3.5.3 SEM Characterization of Hydrogels

SEM images below show the six different hydrogel groups as described on top of each column. Each row represents different magnifications of 100×, 500× and 80000× from top to bottom. The spongy morphology of GelMA can be seen in all of the images. Some white branched structures on the surface can be detected in the hydrogels with collagen (second to sixth column from the left) in 500× magnification images. These structures are pointed with arrows in the second and third row of the figure. From the third to sixth column BGs are added to the hydrogels. Spherical particles marked with arrows are attributed to the bioglass nano particles. The bioglass concentration in the gel from left to right increases, which can be detected from the SEM images.
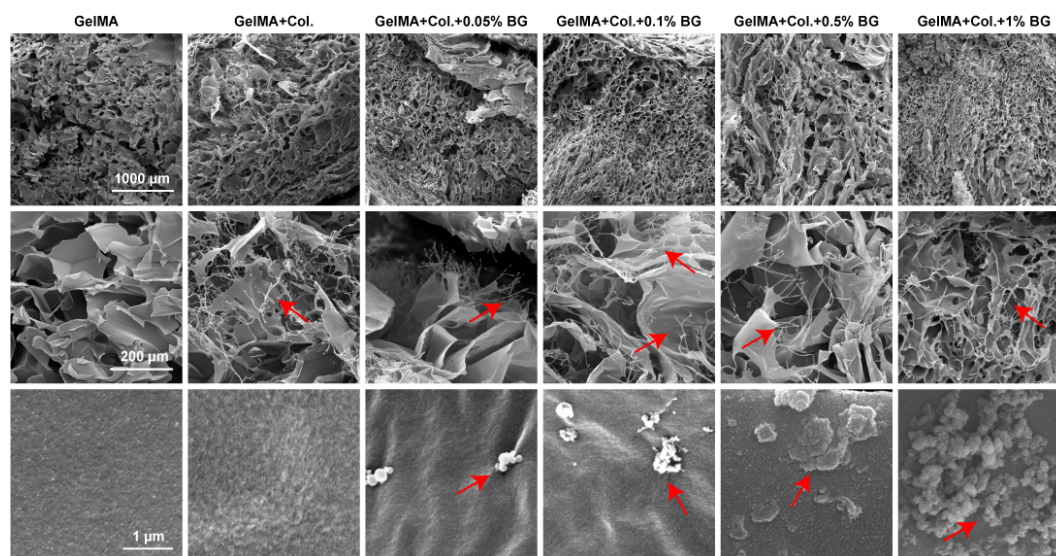
Figure 3.15. SEM characterization of hydrogels with different magnifications. Scale bar is the same for the images of each row. The arrows in the second row are pointing the collagen and in the third row are marking the BG.

3.6 In Vitro Cell Culture Results

3.6.1 Cell Viability

3.6.1.1 Alamar Blue Assay for Disk-Shaped PLA Scaffolds

The attachment and proliferation of hFOB cells on the PLA scaffolds were analyzed by Alamar blue test. Cells were seeded on the scaffolds having different treatments and coatings (Figure 3.16A & B). The results are given by fluorescence intensity (FI) versus time points. For the alkali-modified PLA scaffolds (Figure 3.16A), less cell number viability was observed for high molarity NaOH treated groups in the 1st day, suggesting lower attachment potency of these groups. However, no considerable difference was observed among the groups; and viability levels were similar at the other time points (7, 14 and 21 days). In Figure 3.16A, the cell viability of each group, changes significantly from day 1 to 7 and day 7 to 14, while, from day 14 to 21 the changes are not significant.

For the second set of analysis 0.05 M NaOH treated PLA scaffolds are selected to coat (Figure 3.16B). The high percentages of BG (5, 10 and 15 %) resulted in lower 1st day viability outcomes. However, this effect was seen with 10 % BG involving coating groups on 7th and 14th days as well. Groups were statistically similar at 21st day. Yet, all the results for the different groups have shown no considerable variation between 14th and 21st days. This might be due to inability for detecting viability of cells that proliferated towards inside the scaffold.

3.6.1.2 Alamar Blue Assay for Hydrogels

Figure 3.16C shows the Alamar blue assay results for hydrogel groups. Fluorescence intensity indicates that the cell viability from day 1 to 4 did not increase. The reduction in cells on day 4 can be the effect of UV irradiation. However, the study

98

by Bektaş [240], presented the minimum side effect of UV irradiation in 1 min under 0.120 J/s intensity. After the 4th day the cells started to increase in number until day 21. The groups with difference are pointed in the Figure 3.16. Unlike the PLA groups, we can see the significant difference among day 21 for all groups. GelMA with collagen showed the lowest proliferation among all groups. The positive effect of BG can be noticed. For day 21, the difference between GelMA-Col.-0.05% BG, GelMA with Col.-0.1% BG and GelMA with Col.-0.5% BG (selected group) was statistically non-significant. Therefore, GelMA hydrogel containing 0.5% BG was selected for further 3D experiments (3D PLA structures filled with GelMA hydrogel). Two-way ANOVA assessment demonstrates a significant statistical difference (P<0.0001) between days 14 and 21 for all the hydrogel groups.
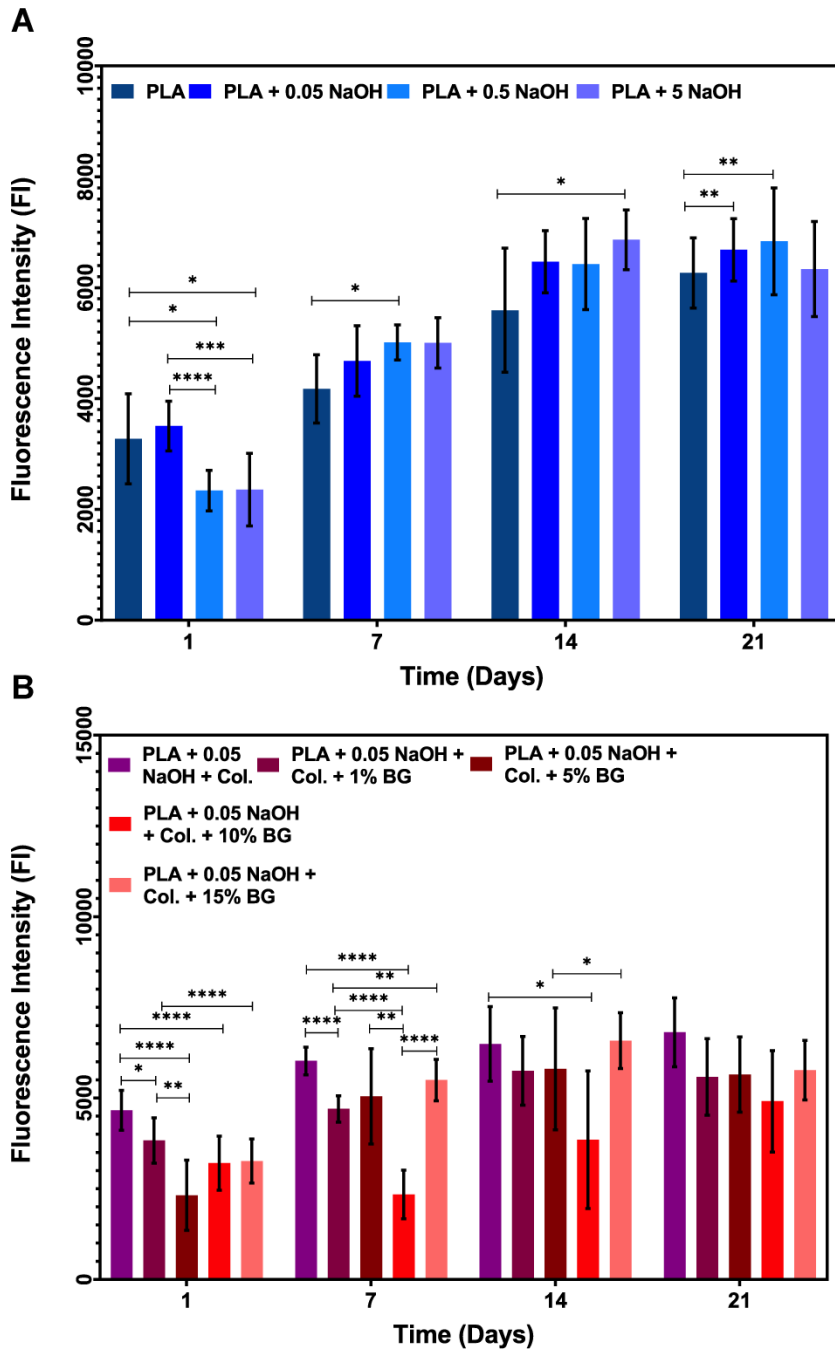
Figure 3.16. Alamar blue results for all groups. A) Alamar blue results for alkali treated PLA scaffolds vs. neat PLA. B) Alamar blue for different coatings of PLA. C) Alamar blue test for GelMA hysdrogels with collagen and different concentrations of BG. $****$ indicates P$\leq$0.0001, $***$ means P$\leq$0.001. $**$ shows P$\leq$0.01 and finally $*$ means P$\leq$0.05.

100
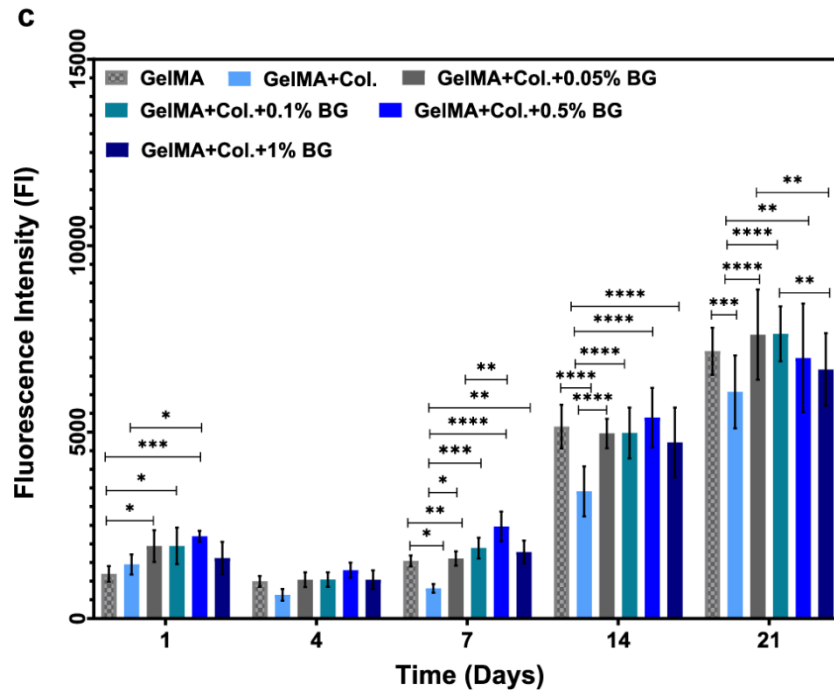
Figure 3.16. (cont'd) Alamar blue results for all groups. A) Alamar blue results for alkali treated PLA scaffolds vs. neat PLA. B) Alamar blue for different coatings of PLA. C) Alamar blue test for GelMA hysdrogels with collagen and different concentrations of BG. **** indicates P≤0.0001, *** means P≤0.001. ** shows P≤0.01 and finally * means P≤0.05.

3.6.2   Live-Dead Assay

3.6.2.1   Live-Dead Assay for Disk-Shaped PLA Scaffolds

Another viability and proliferation test is a live-dead assessment for different groups and time points. Figure 3.17A shows the control group (cells seeded in tissue culture plates) and neat PLA scaffolds. We can see less proliferation of cells in PLA compared to TCPS, which is expected. In Figure 3.17B we can see the proliferation of hFOB cells on alkali-treated scaffolds. Regardless of NaOH concentration, the cells are proliferated on the scaffold in 14 days. Comparing these results with cell

proliferation results on the coated scaffolds (Figure 3.17C), the clear attachment of cells on coated scaffolds for day 1 compared to non-coated and/or neat PLA can be noticed. Cell elongations and extensions is observable in day 1 results for coated PLA scaffolds (Figure 3.17C), which is the reason for coating PLA before cell seeding. It indicates that the cells can proliferate better on a hydrophilic substrate. Collagen and collagen-BG coating provides this hydrophilic environment for the cells. Considering the Alamar blue and live-dead experiment results for disk-shaped scaffolds the collagen coating and collagen-1% BG coating were selected for cell seeding on 3D PLA scaffold experiments.

The viability and proliferation of the cells during 14 days are detected. For all the images, green color shows viability while red indicates dead cells.
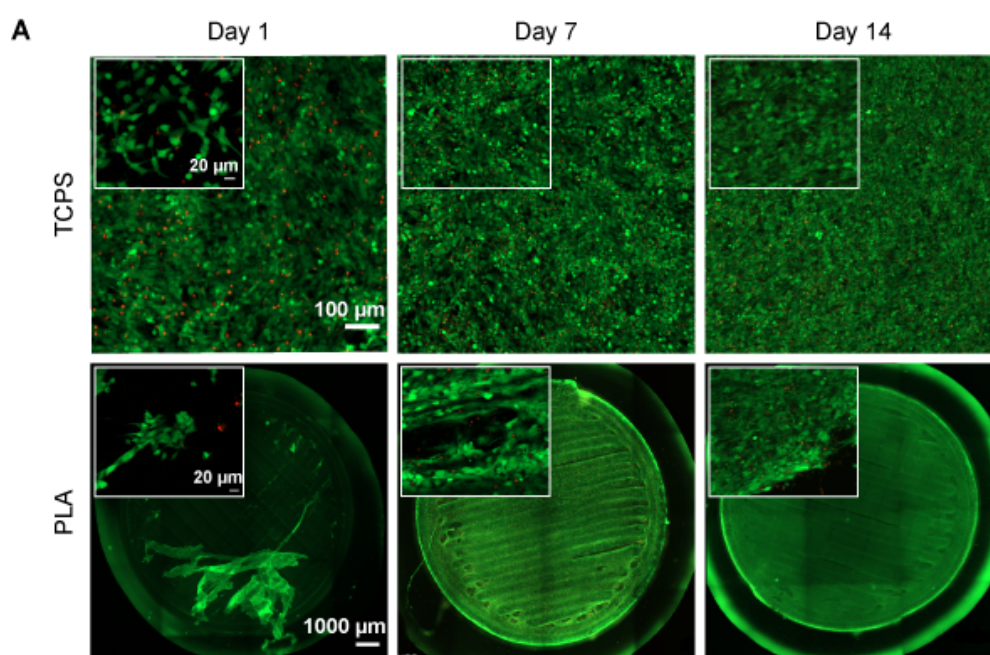
Figure 3.17. Confocal micrographs of live-dead assay for PLA scaffolds. A) Shows the live- dead results for control group and neat PLA (without any treatment). B) Live-dead for alkali treated PLA scaffolds with 0.05, 0.5 and 5 M NaOH. C) Live-dead images for collagen coated and collagen-BG coated PLA scaffolds with different BG concentrations. 20 μm scale bar corresponds to 20× and 100 μm to 5× magnifications. Red color indicates dead cells while the green on means the cells are

alive. Scale bar is the same for the images of same size for each column and row. Except A which the scale bar is repetitive for each row.

Figure 3.17. (cont'd) Confocal micrographs of live-dead assay for PLA scaffolds. A) Shows the live- dead results for control group and neat PLA (without any treatment). B) Live-dead for alkali treated PLA scaffolds with 0.05, 0.5 and 5 M NaOH. C) Live-dead images for collagen coated and collagen-BG coated PLA scaffolds with different BG concentrations. 20 μm scale bar corresponds to 20× and 100 μm to 5× magnifications. Red color indicates dead cells while the green on means the cells are alive. Scale bar is the same for the images of same size for each column and row. Except A which the scale bar is repetitive for each row.

Figure 3.17. (cont'd) Confocal micrographs of live-dead assay for PLA scaffolds. A) Shows the live- dead results for control group and neat PLA (without any treatment). B) Live-dead for alkali treated PLA scaffolds with 0.05, 0.5 and 5 M NaOH. C) Live-dead images for collagen coated and collagen-BG coated PLA scaffolds with different BG concentrations. 20 μm scale bar corresponds to 20× and 100 μm to 5× magnifications. Red color indicates dead cells while the green on

means the cells are alive. Scale bar is the same for the images of same size for each column and row. Except A which the scale bar is repetitive for each row.

3.6.2.2   Live-Dead Assay for Hydrogels

The live-dead assay for gels is presented in the Figure 3.18. The elongation and viability of hFOB cells is obvious on 4th and 7th days. From day 7 cells started to proliferate to reach the confluence. Similar to the Alamar blue results, gels showed a decrease in the number of cells on day 4. GelMA-Col. with 1% BG concentration exhibits less proliferation among the BG groups. The results are in a good match with Alamar blue results at and after day 7. According to the live-dead assay and Alamar blue results the GelMA-Col.-0.05% BG and GelMA-Col.-0.1% BG and GelMA-Col.-0.5% BG displayed better cell proliferation, elongation, and viability. The GelMA-Col.-0.5% BG is selected from the BG containing groups for further 3D assessments.
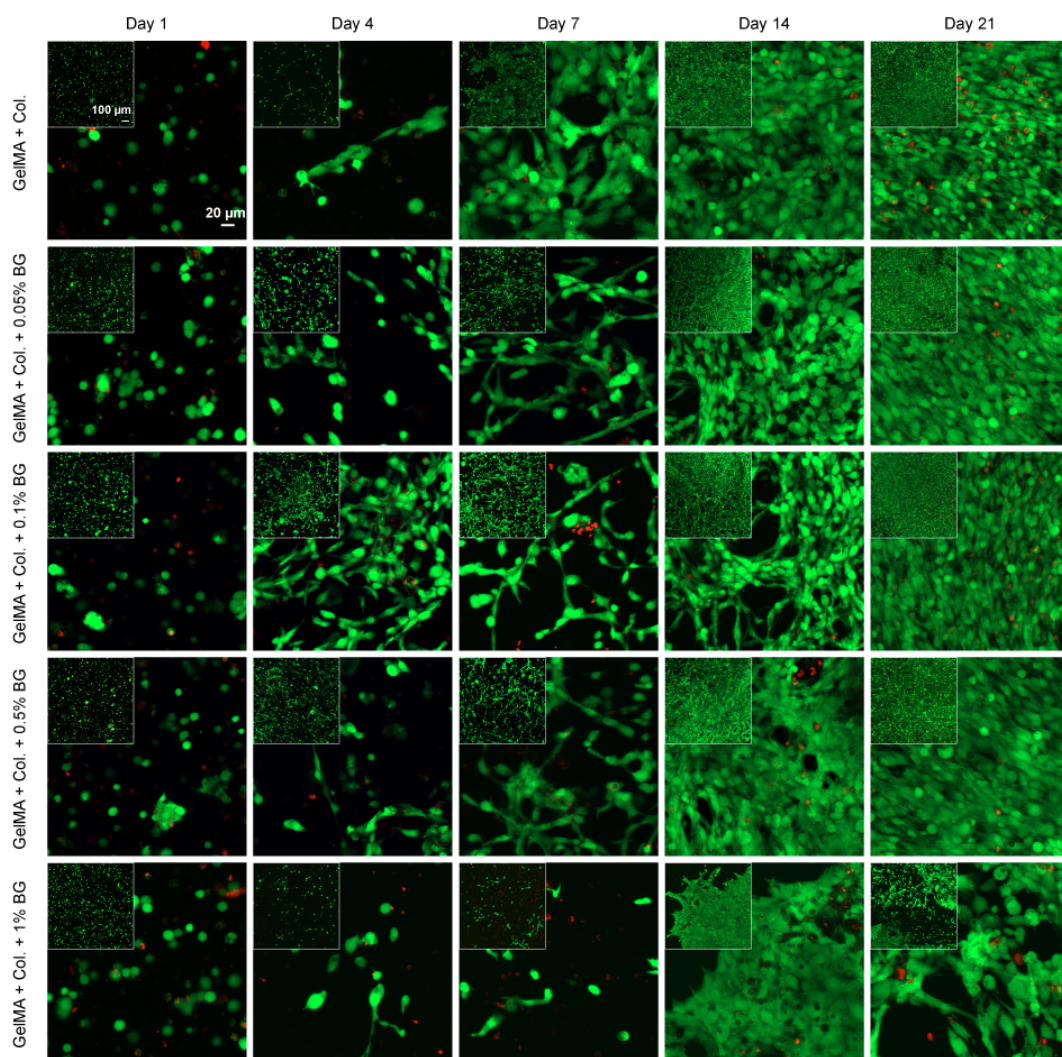
Figure 3.18. Live-dead confocal microscope images for hydrogels. 20 μm scale bar corresponds to 20× and 100 μm to 5× magnifications. Red color indicates dead cells while the green one means the cells are alive. Scale bar is the same for the images of same size for each column and row.

3.6.2.3 Live-Dead Assay for 3D PLA Scaffolds with Hydrogel Filling

Three geometries: i) Schwarz-P5 (Figure 3.19A), ii) Cube with regular pores (Figure 3.19B) and iii) Voronoi 25 points, 0.8 distance (Figure 3.19C) were selected for gel loaded bone tissue scaffold experiments. The structures were selected based on two different porosities (around 50% and 70%) and three different pore shapes. The 3D

cubic scaffolds were filled with cell and collagen laden GelMA. Second row of each belongs to a closer view of the pores. Live-dead test for 3D structures shows the poor proliferation and elongation of the cells for Schwarz group. This phenomenon can be due to the high porosity of Schwarz (76%) among the others. However, the regular porous cubic and Voronoi groups demonstrated better Vibility, proliferation and elongation of cells.

According to the live dead results for collagen and cell loaded GelMA filled 3D structures in the prevoius set of experiments, Voronoi type structure is selected for BG containing group of GelMA hydrogel with 0.5% concentration of BG. The results of BG loaded hydrogel for Voronoi type (Figure 3.19D) show even more cells' viability and proliferation, which is the desired outcome. The control group for this experiment is characterized as thick (regular cube and Voronoi) and thin (for Schwarz) needles used for filling the gels (Figure 3.19E). There can be seen no significant difference between these two types in proliferation and viability of the cells; however, the thicker one showed slightly better elongation than the thin one.
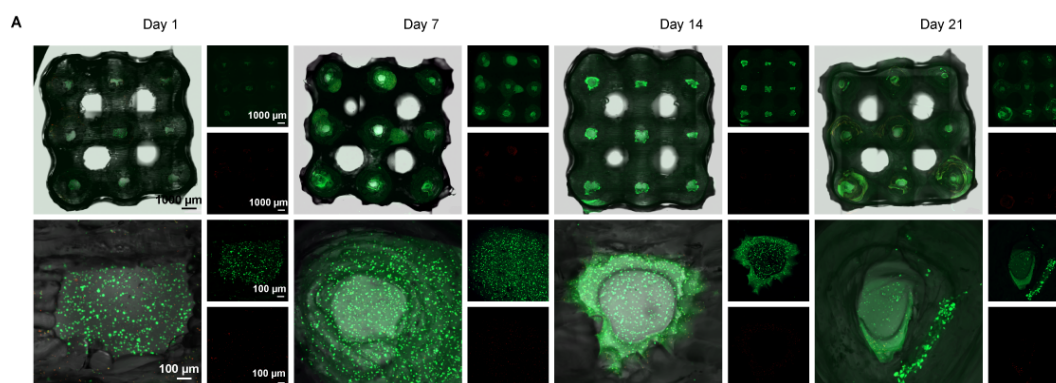
Figure 3.19. Live-dead results for 3D printed PLA+GelMA+Col. (A, B & C), & 3D PLA+ GelMA +Col.+0.5%BG (D). A) Schwarz-P 5 (76% porosity), B) Regular porous cube (51% porosity), C) Voronoi 25 points 0.8 distance, and D) Voronoi 25 points 0.8 distance (71% porosity) with 0.1% BG. E) Live-dead of control group for 3D PLA scaffolds filled with hydrogel. Red color indicates dead cells while the green on means the cells are alive. 100 μm and 1000 μm indicate 5× magnifications.

corresponds to Scale bar is the same for the images of same size for each column and row.

Figure 3.19. (cont'd) Live-dead results for 3D printed PLA+GelMA+Col. (A, B & C), & 3D PLA+ GelMA +Col.+0.5%BG (D). A) Schwarz-P 5 (76% porosity), B) Regular porous cube (51% porosity), C) Voronoi 25 points 0.8 distance, and D) Voronoi 25 points 0.8 distance (71% porosity) with 0.1% BG. E) Live-dead of control group for 3D PLA scaffolds filled with hydrogel. Red color indicates dead cells while the green on means the cells are alive. 100 μm and 1000 μm indicate 5×

Figure 3.19. (cont'd) Live-dead results for 3D printed PLA+GelMA+Col. (A, B & C), & 3D PLA+ GelMA +Col.+0.5%BG (D). A) Schwarz-P 5 (76% porosity), B) Regular porous cube (51% porosity), C) Voronoi 25 points 0.8 distance, and D) Voronoi 25 points 0.8 distance (71% porosity) with 0.1% BG. E) Live-dead of control group for 3D PLA scaffolds filled with hydrogel. Red color indicates dead cells while the green on means the cells are alive. 100 μm and 1000 μm indicate 5× magnifications. corresponds to Scale bar is the same for the images of same size for each column and row.

3.6.3   Cell Culture Results for Analysis of Cell Adhesion and Distribution

3.6.3.1   Analysis of Cell Adhesion on Disk-Shaped PLA Scaffolds

For this set of experiments, 15×10^3 were seeded on the disk-shaped scaffolds, and the experiment continued for 7 days upon reaching confluency. Figure 3.20A shows the phalloidin-DAPI results for PLA and alkali modified PLA and collagen-coated one, and 3.20B shows these results for coated scaffolds with different concentrations of BG. The elongation and attachment of cells can be observed on the first day.
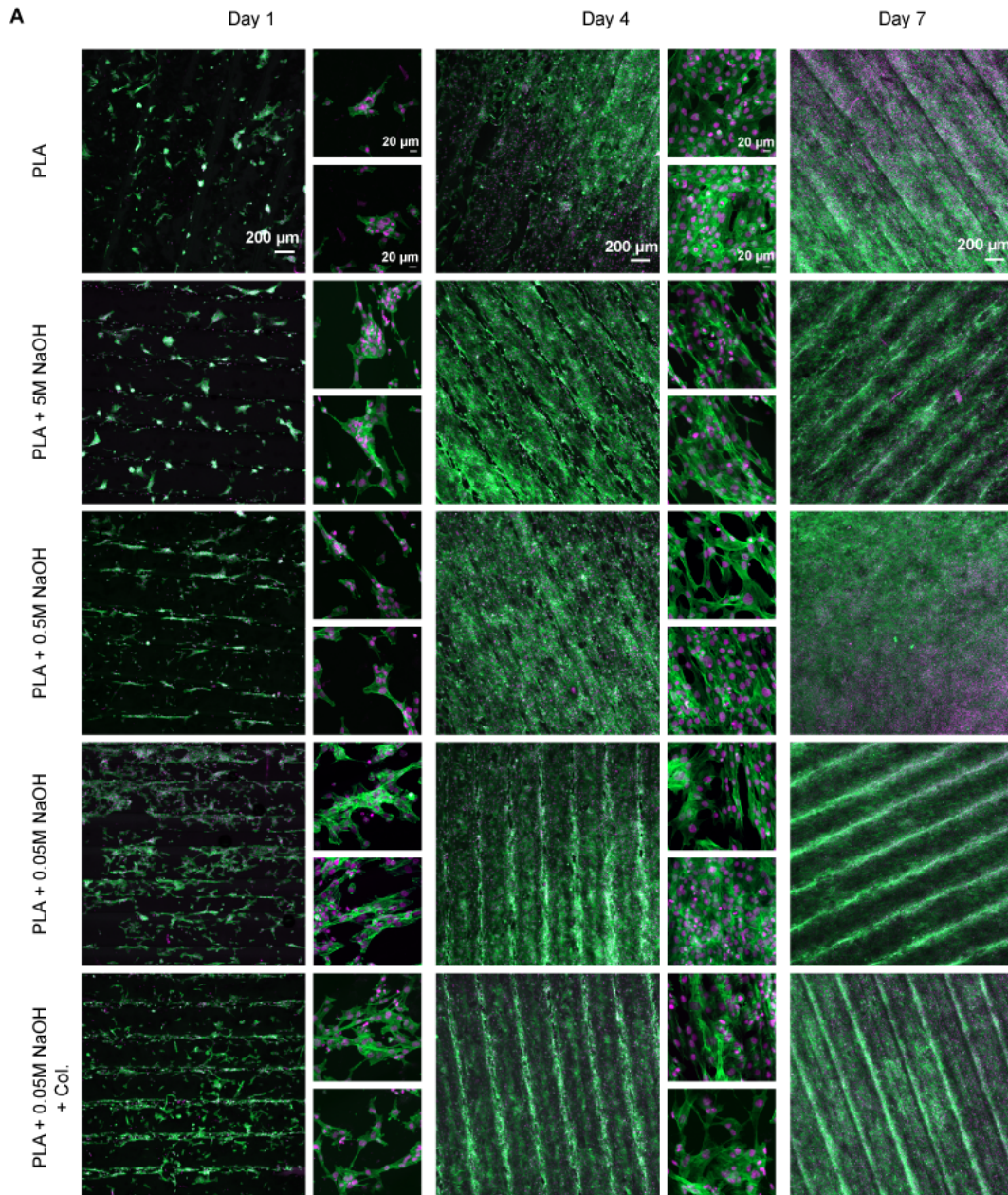
Figure 3.20. Phalloidin-Dapi staining of 15×10^3 cell density seeded on PLA scaffolds. A) PLA without treatment, alkali modified scaffolds and collagen coated one. B) Collagen and BG (1, 5, 10 and 15 (w/v%)) coated PLA scaffolds. The purple color indicates the nucleus and green color shows the actin cytoskeleton. Scale bare is the same for each column.
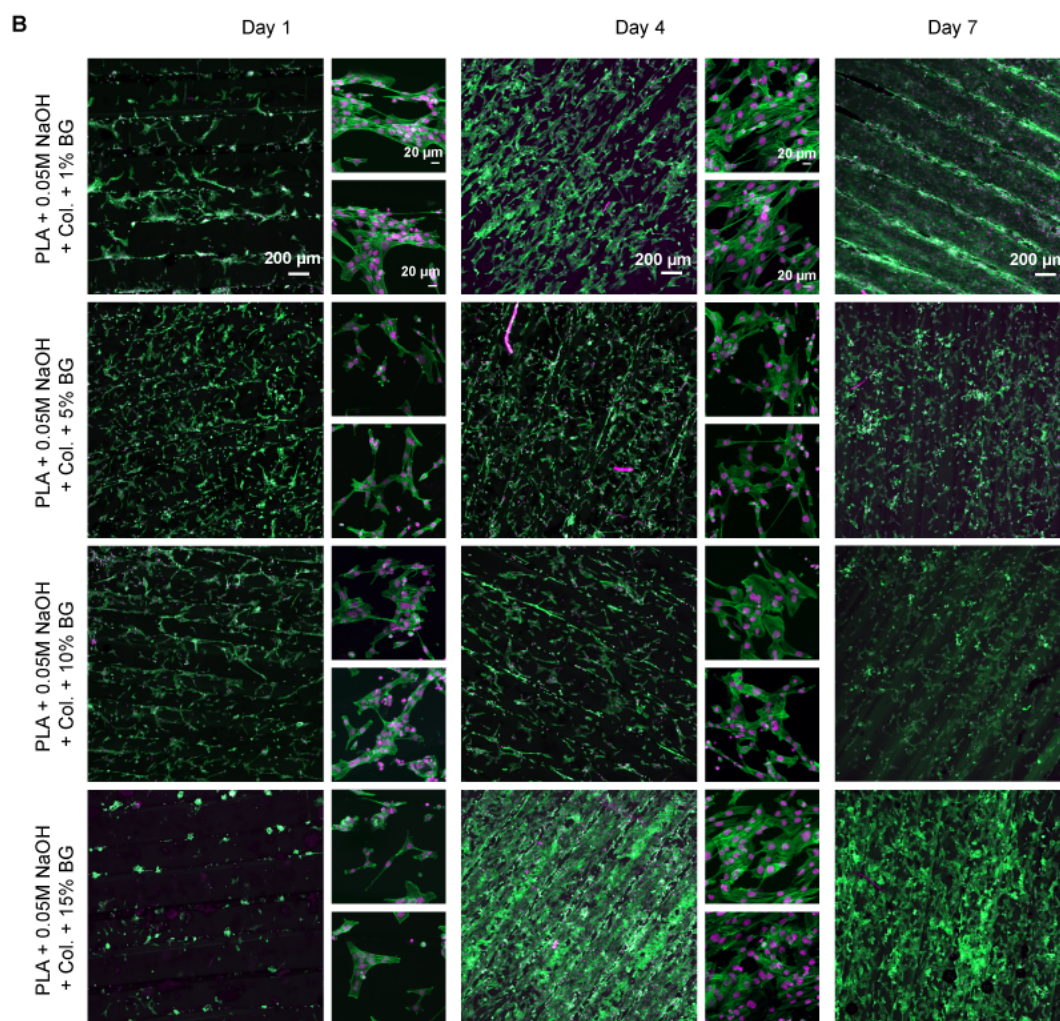
Figure 3.20. (cont'd) Phalloidin-Dapi staining of 15×10^3 cell density seeded on PLA scaffolds. A) PLA without treatment, alkali modified scaffolds and collagen coated one. B) Collagen and BG (1, 5, 10 and 15 (w/v%)) coated PLA scaffolds. The purple color indicates the nucleus and green color shows the actin cytoskeleton. Scale bare is the same for each column.

The confocal micrographs show the flattened overall shape of the cells. The purple color indicates the nucleus, and the green color shows the actin cytoskeleton. Due to the high proliferation rate of hFOB cells the scaffolds are confluent after 7 days of incubation.

The SEM images for the PLA scaffolds mentioned in this section show the supporting results for cell proliferation and elongation (Figure 3.21). The filopodia can be observed in phalloidin-DAPI and SEM images. Some of the cells are marked with arrows.
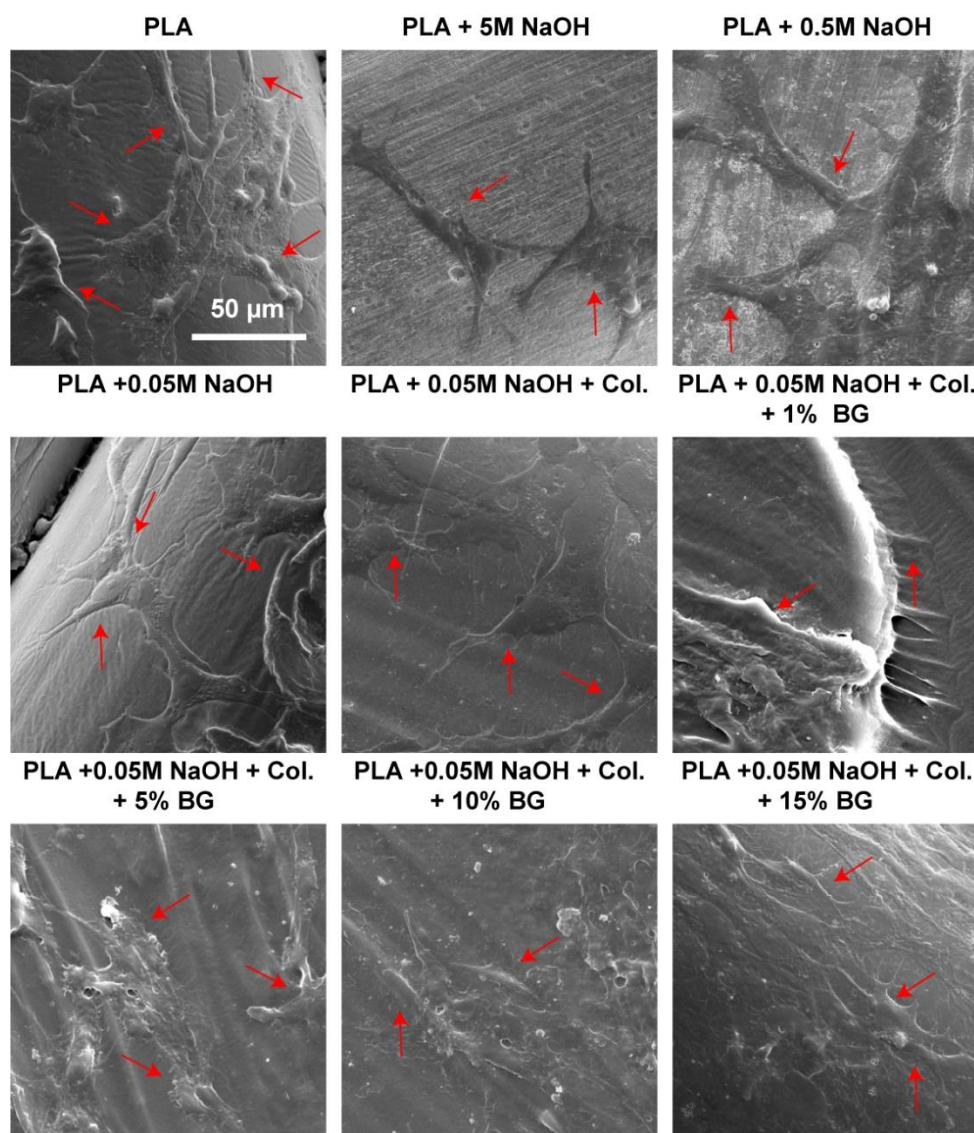
Figure 3.21. SEM images for the first day of cell seeded PLA scaffolds with different modifications and coatings. Red arrows are pointing the cells. Images are magnified 2000 times.

3.6.3.2 Analysis of Cell Adhesion on 3D- PLA Scaffolds

The Figure 3.22 given below shows the phalloidin-DAPI staining for 3D printed, alkali modified, and collagen-coated PLA geometries after 21 days of incubation. These 9 groups of samples are selected due to various porosities (ranging from 17% to 76%), and internal structures. The structure with regular and irregular pore shapes were chosen to observe the effect of pore structure. Despite the different pore sizes and porosities of 9 candidate 3D scaffiolds, full confluency of the cells could be achieved in all of the selected geometries. Figure 3.22 g, h and i have roughly equal porosities with different internal and external structures, this also did not affect the cell proliferation. Here pink color is a representative of DAPI stained nucleus, indicating viability and blue is due to staining of the actin protein in cytoskeleton. The second set of experiments were done with collagen and collagen-1% BG coated forms of two selected types (i) Regular porous cube , (ii) Voronoi 25 points, distance 1.2, of the 3D scaffolds presented above (Figure 3.22) due to their better mechanical properties and porosity and different pore structures. These results showed the good proliferation and migration of the cells in the porous scaffolds (Figure 3.23A & B). Slightly better proliferation of the cells, especially inside the pores for Voronoi types, can be related with its less porosity than regular cube and irregular pore shapes resembling to the native bone. Unfortunately, marked (∗) images were impossible to capture since cell colonization could be observed through the pores for both structures with regular and irregular pore shapes on days 14 and 21.
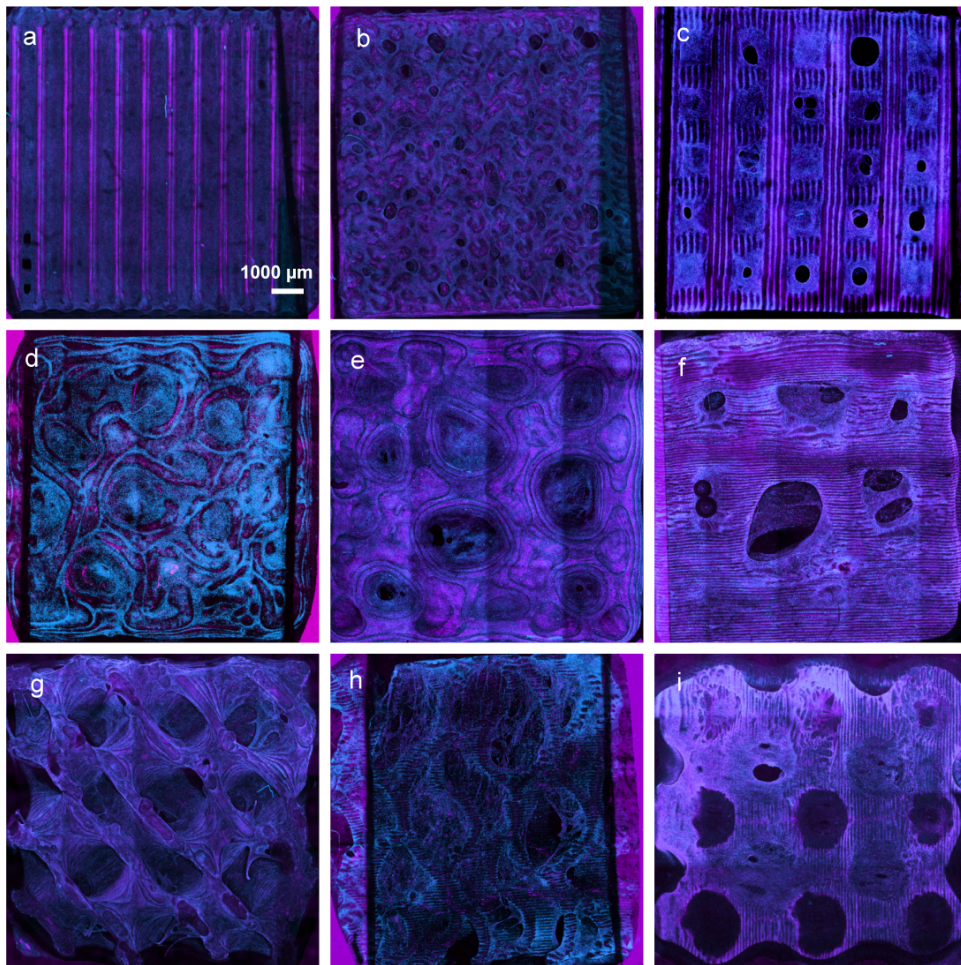
Figure 3.22. Phalloidin-Dapi staining for 3D printed PLA scaffolds. a) mesh cube (52% porosity), b) cube with regular small pores (47% porosity), c) cube with regular large pores (51% porosity), d) Voronoi 75 points, distance 1.2 (17% porosity), e) Voronoi 50 points, distance 1.2 (26% porosity), f) Voronoi 25 points, distance 1.2 (42% porosity), g) Diamond (76% porosity), h) gyroid 4 (76% porosity) and i) Schwarz-P 5 (76% porosity).
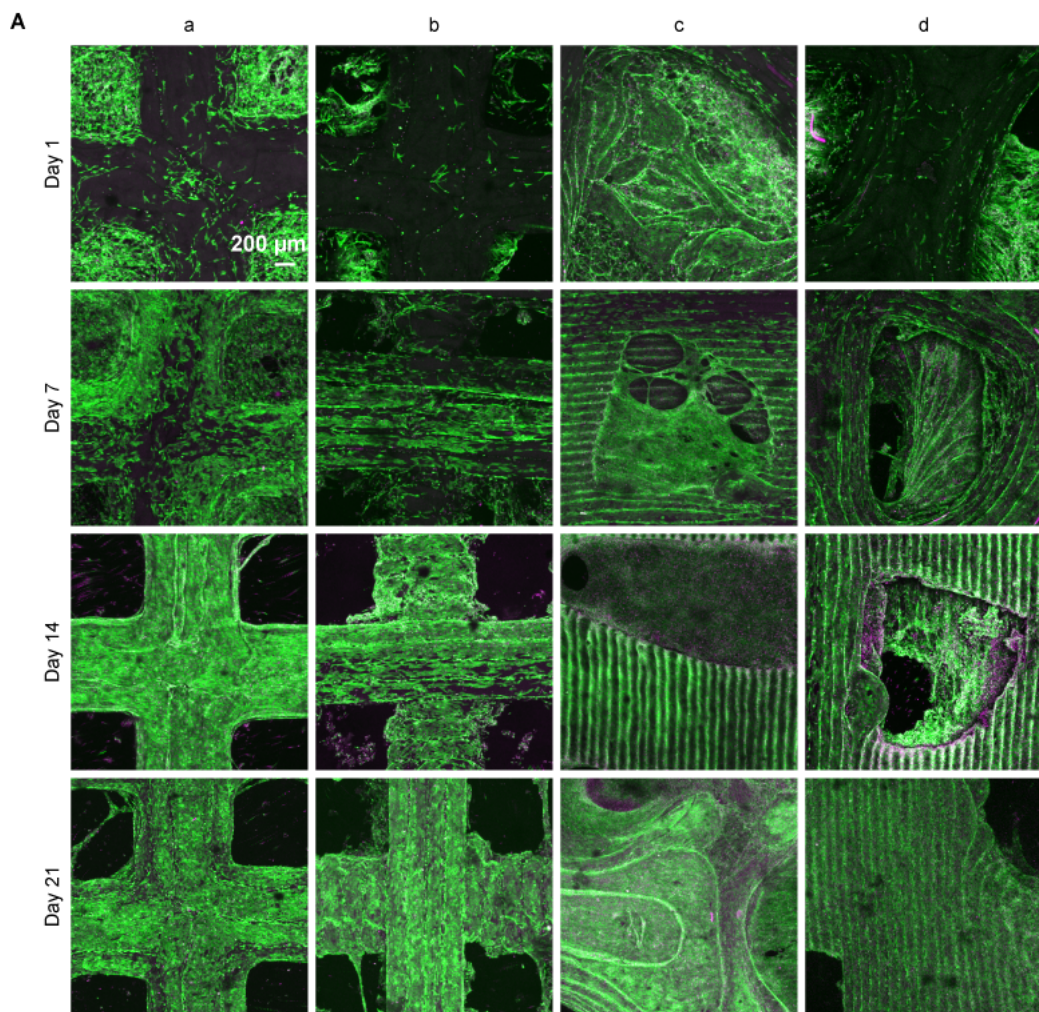
Figure 3.23. Phalloidin-Dapi staining for Regular porous cube and Voronoi 25 points, distance 1.2 with collagen and collagen-BG coating. a) Regular porous cube with collagen (51% porosity), b) Regular porous cube with collagen and 1% BG c) Voronoi 25 points, distance 1.2 with collagen, d) Voronoi 25 points, distance 1.2 (42% porosity) with collagen and 1% BG. The images with ∗ mark were not taken due to lack of cells inside the pores on days 14 and 21. A) Represents the images with 5× and B) shows then with 10× maginification. B shows the surface of the scaffold and inside the pores. Green indicates cytoskeleton and purple determines the nuclei. Scale bar is the same for each column and row.
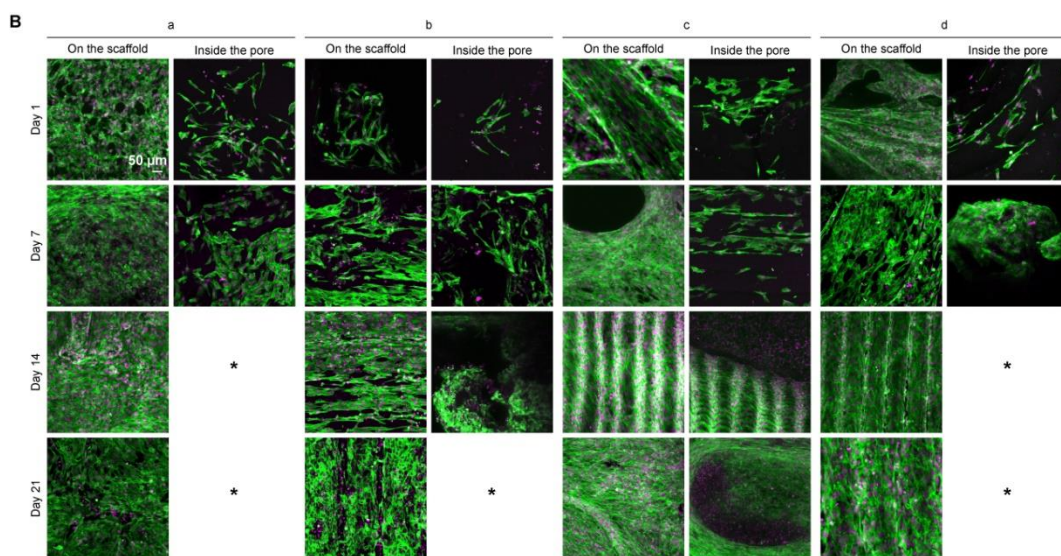
Figure 3.23. (cont'd) Phalloidin-Dapi staining for Regular porous cube and Voronoi 25 points, distance 1.2 with collagen and collagen-BG coating. a) Regular porous cube with collagen (51% porosity), b) Regular porous cube with collagen and 1% BG c) Voronoi 25 points, distance 1.2 with collagen, d) Voronoi 25 points, distance 1.2 (42% porosity) with collagen and 1% BG. The images with * mark were not taken due to lack of cells inside the pores on days 14 and 21. A) Represents the images with 5× and B) shows then with 10× maginification. B shows the surface of the scaffold and inside the pores. Green indicates cytoskeleton and purple determines the nuclei. Scale bar is the same for each column and row.

3.6.3.3   Analysis of Cell Distribution for Hydrogels

The hydrogels' phalloidin-dapi results support the Alamar blue and live-dead experiments. The cells' desired elongation and proliferation are observable in hydrogels containing collagen and collagen-BG (Figure 3.24). The blue color is proof of cytoskeleton existence, and orange color marks the nucleus of the cells.

116
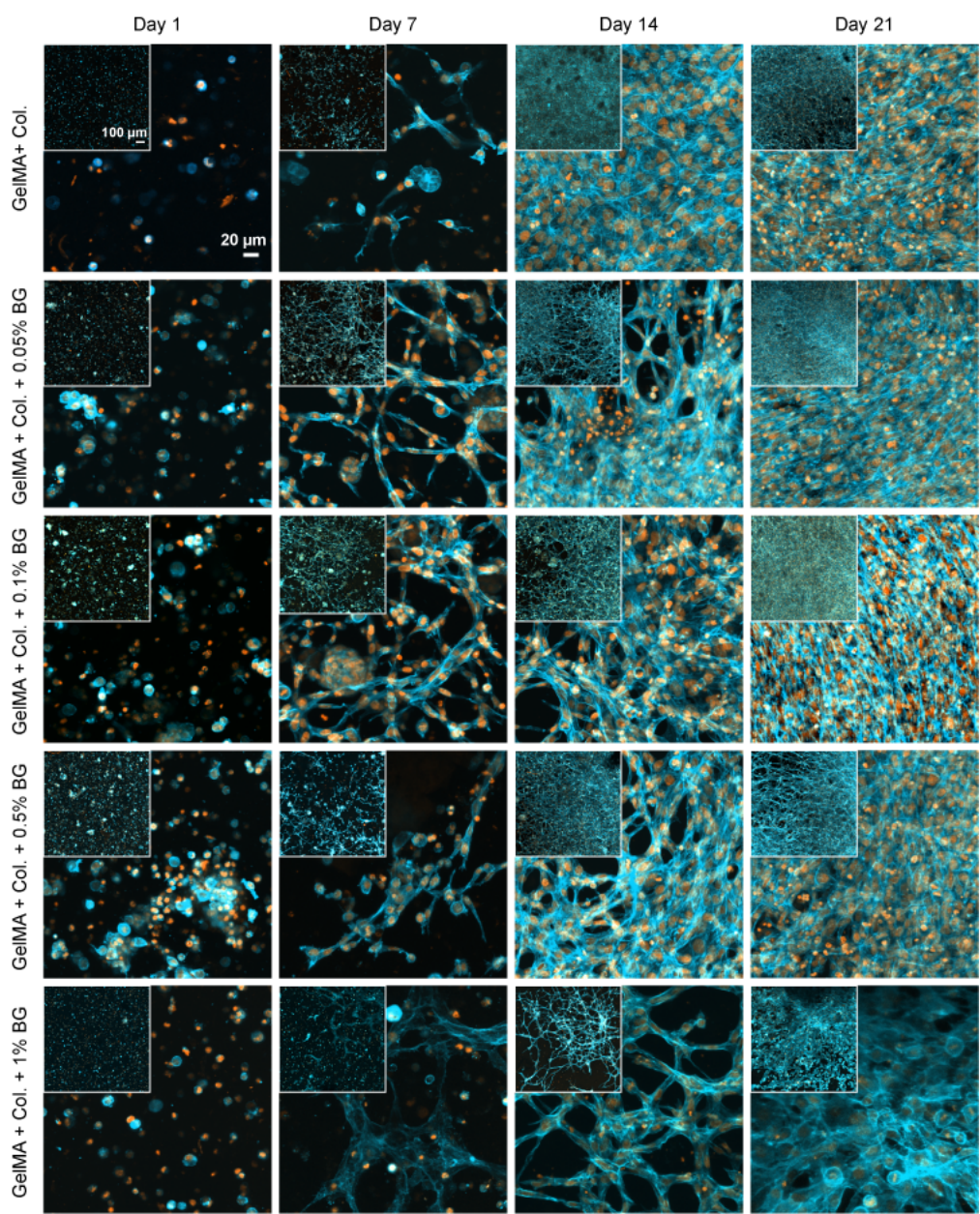
Figure 3.24. Confocal microscope images for collagen and collagen-BG loaded GelMA hydrogels. Orange color shows nucleus and blue represents cytoskeleton. Scale bar is the same for all images. 100 μm scale bar shows 5× and 20 μm shows 20× magnification.

3.6.3.4   Analysis of Cell Distribution for Hydrogel Filled 3D PLA Scaffolds

The figure below shows this staining for 3D PLA scaffolds (Voronoi type) filled with collagen and collagen-0.5% BG for 21 days. Although this type of geometry is highly porous (71%), a good extension of the cells and filopodia was observed. The BG-containing gels exhibit more flattened morphology for the cells.
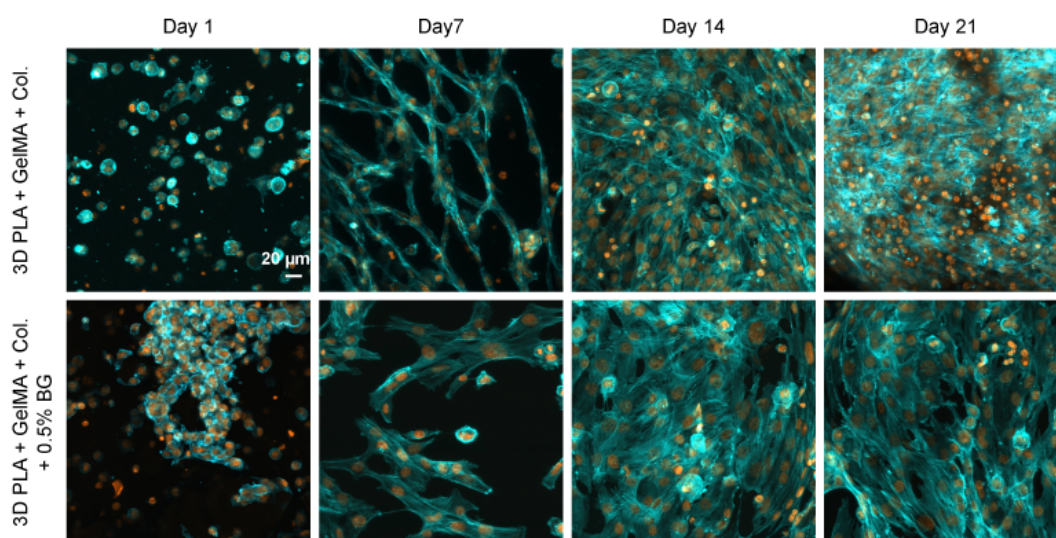
Figure 3.25. Phalloidin-Dapi staining for 3D PLA+GelMA+Col. (Voronoi 25 points with 0.8 distance) with and without BG

3.6.4   SEM Analysis of Cell Morphology on Scaffolds

3.6.4.1   Disk-Shaped PLA Scaffolds

SEM images of cells on the surface of the PLA scaffolds with different coating properties are presented in Figures 3.26A and 3.26B for days 1 and 21 . It can be easily recognized that in accordance with previous results, the number of cells on the surface considerably increased from day 1 to 21. Confluent coating of surface with cells was noticeable on day 21 in all groups. On the first day, filopodia and cell elongations are recognizable. Some of the cells are pointed with a red arrow.
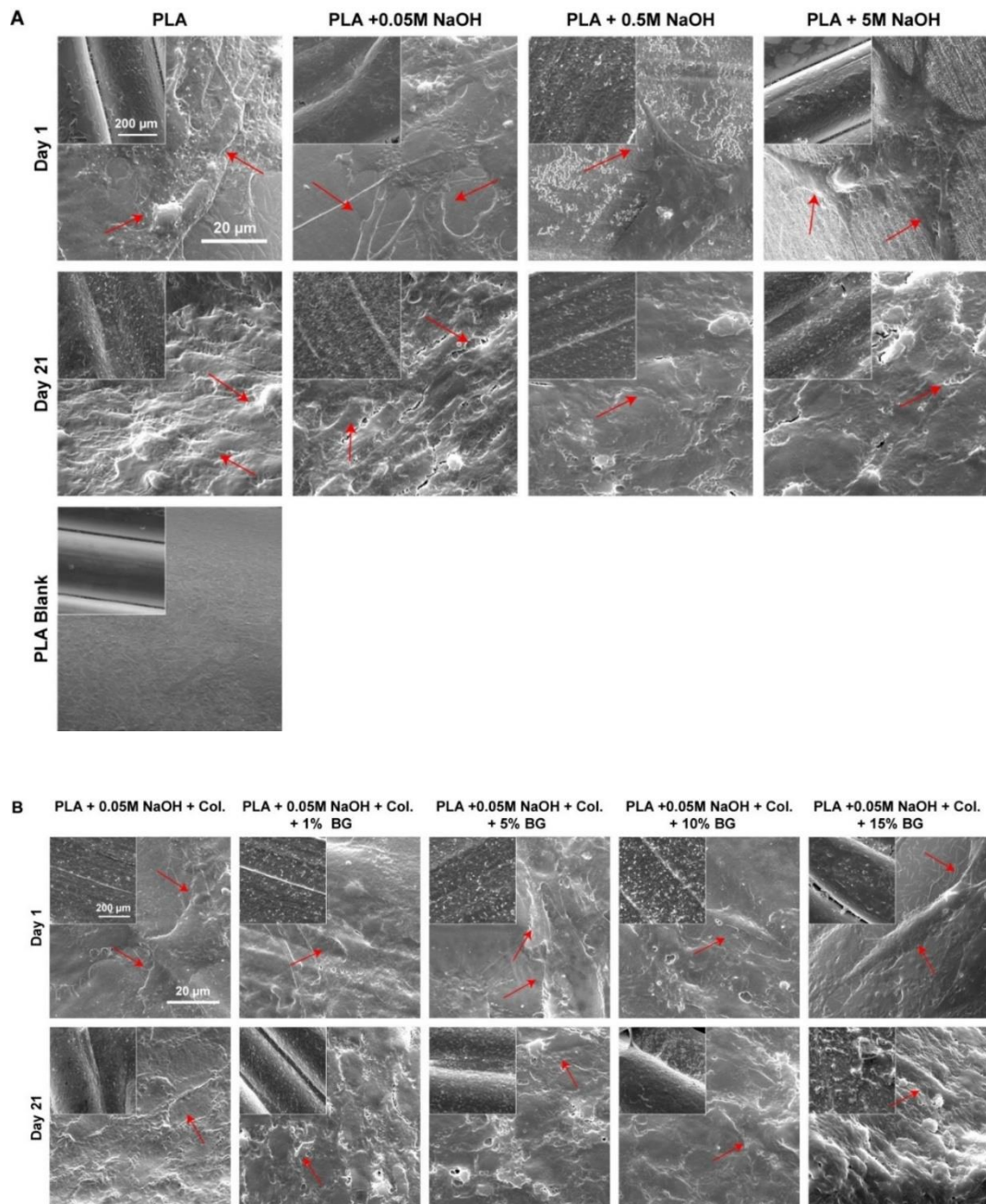
Figure 3.26. SEM images for disk-shaped PLA scaffolds. A) PLA scaffolds with different alkali treatments and blank PLA. B) PLA scaffolds with various coating properties. Red arrows are marking the cells. Scale bar is the same for each column and row. Small images are 500× magnification while the larger ones are 4000×.

3.6.4.2   3D PLA Scaffolds

The SEM images for 9 selected groups of 3D printed collagen-coated PLA scaffolds for day 7 are shown in Figure 3.27. Good proliferation and migration of the cells can be detected similar to the phalloidin-DAPI staining results. The effect of porosity, pore size, and geometry can be neglected for the cell proliferation and spread on the surface of these specific structures. Red arrows spot some of the cells.
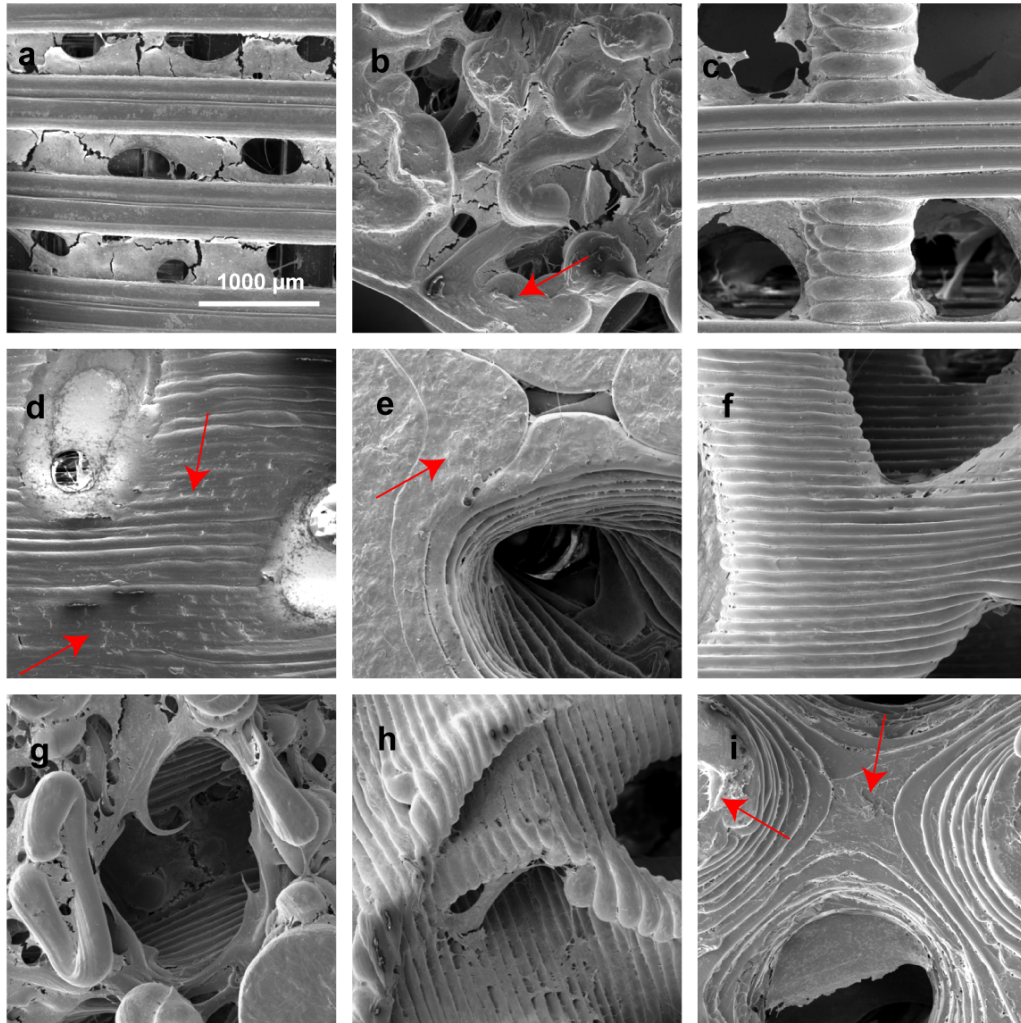
Figure 3.27. SEM images of collagen coated 3D PLA scaffolds. A) Shows the images with 100× magnification and B) shows 500× and 2000× magnifications. a) mesh cube (52% porosity), b) cube with regular small pores (47% porosity), c) cube with regular large pores (51% porosity), d) Voronoi 75 points, distance 1.2 (17% porosity), e) Voronoi 50 points, distance 1.2 (26% porosity), f) Voronoi 25 points, distance 1.2 (42% porosity), g) Diamond (76% porosity), h) gyroid 4 (76% porosity) and i) Schwarz-P 5 (76% porosity). Scale bar is the same in each column and row. Red arrows are spotting the cells.

B
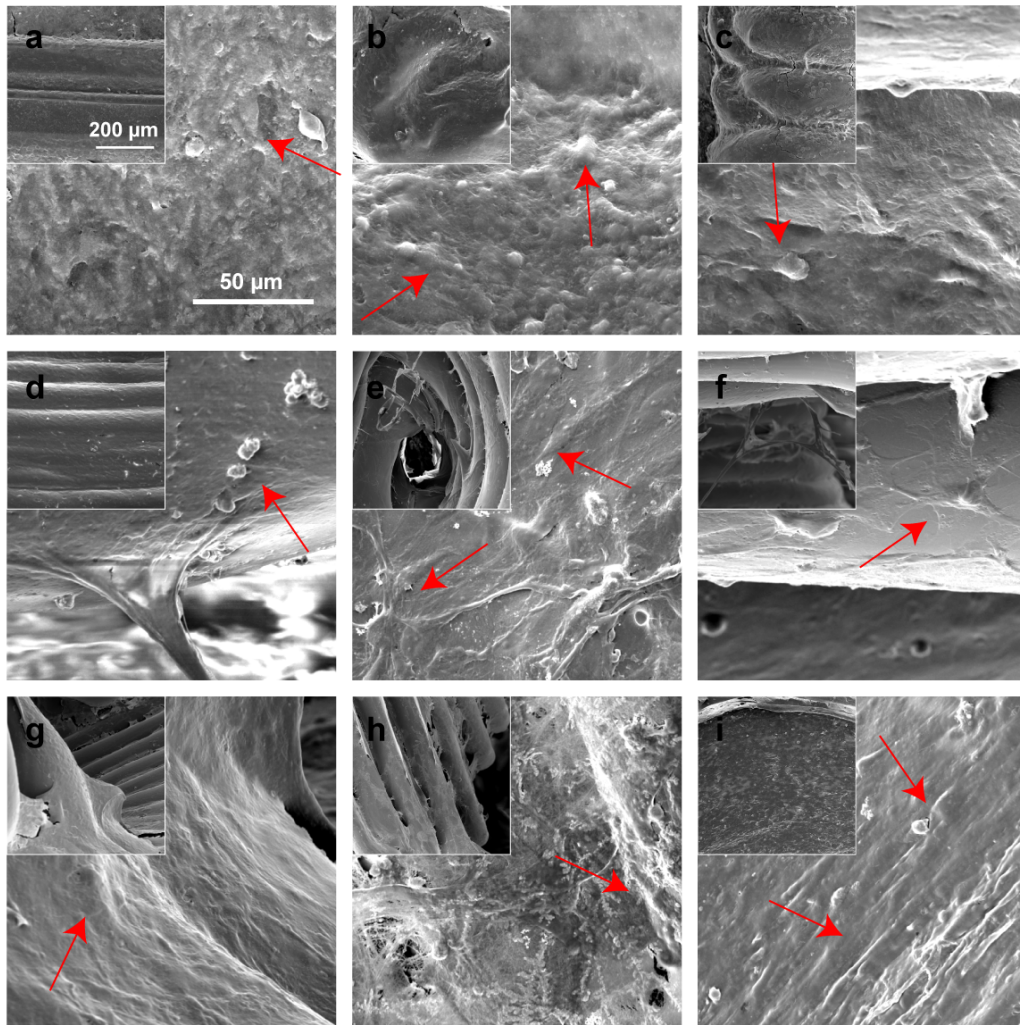
Figure 3.27. (cont'd) SEM images of collagen coated 3D PLA scaffolds. A) Shows the images with 100× magnification and B) shows 500× and 2000× magnifications. a) mesh cube (52% porosity), b) cube with regular small pores (47% porosity), c) cube with regular large pores (51% porosity), d) Voronoi 75 points, distance 1.2 (17% porosity), e) Voronoi 50 points, distance 1.2 (26% porosity), f) Voronoi 25 points, distance 1.2 (42% porosity), g) Diamond (76% porosity), h) gyroid 4 (76% porosity) and i) Schwarz-P 5 (76% porosity). Scale bar is the same in each column and row. Red arrows are spotting the cells.

3.6.4.3   3D PLA Scaffolds Filled with Hydrogel

The SEM images (Figure 3.28) show the cell migrations from gels toward the scaffold surface as cells were initially seeded inside gels for these types of scaffolds. The pores free of gels might result from GelMA degradation in the medium during the incubation period. Unlike the disk-shaped scaffolds, 3D scaffolds with gels showed globular morphology for the cells, particularly for day 1 and 7. With time, these globular structures were elongating, as we can see in the SEM results of days 14 and 21. However, the Voronoi type shows better expansion even for day 7. The least elongation of cells with the least filopodia is dedicated to schwarz geometry with highest porosity (76%). The other two geometries represent better proliferation and cell spread properties. Another remarkable outcome is the migration of the cells from gel toward scaffold surface, which supports the idea of filling the 3D scaffolds with hydrogel to provide an interconnected network.
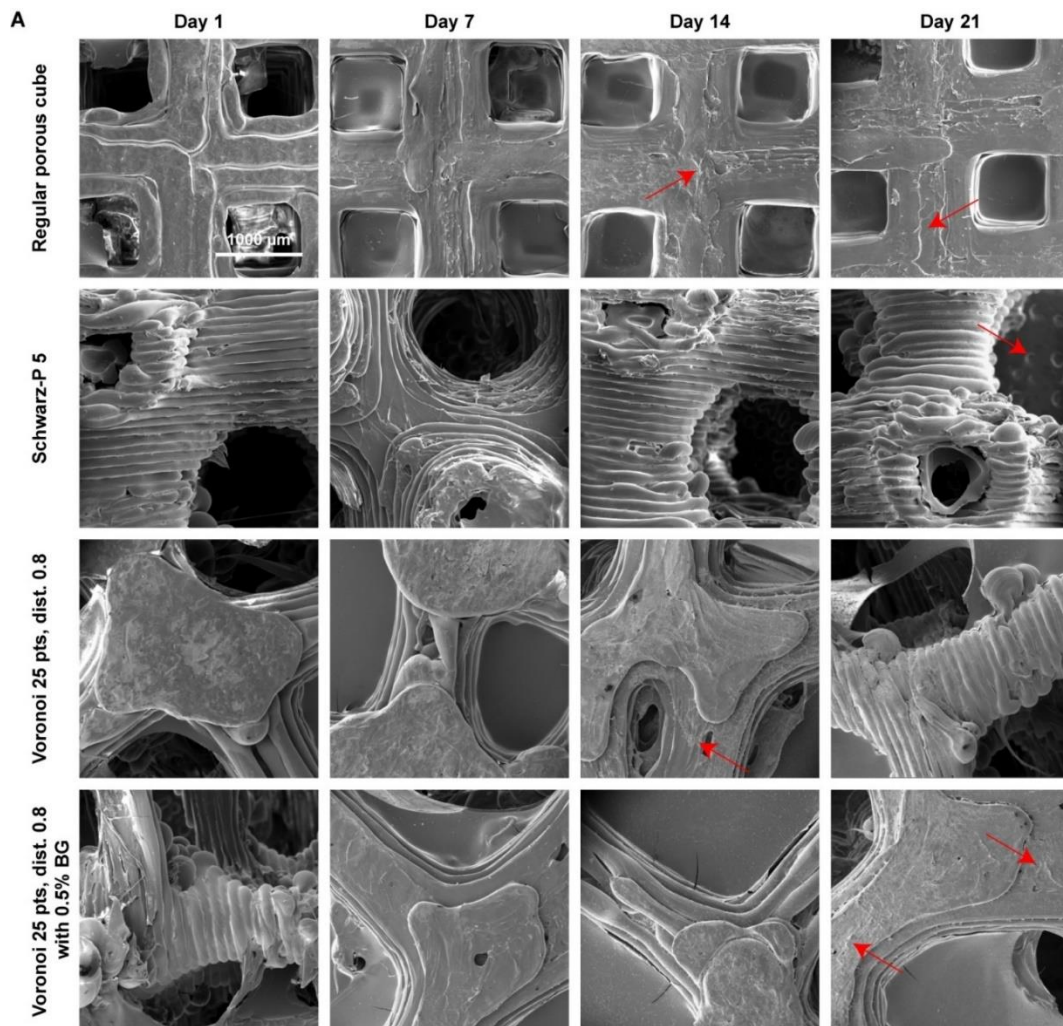
Figure 3.28. SEM results for gel filled 3D PLA scaffolds. A) Image of 100×
magnification. B) Shows 250× and 2000× magnifications. Scale bar is the same in
each column and row. Red arrows are spotting the cells.
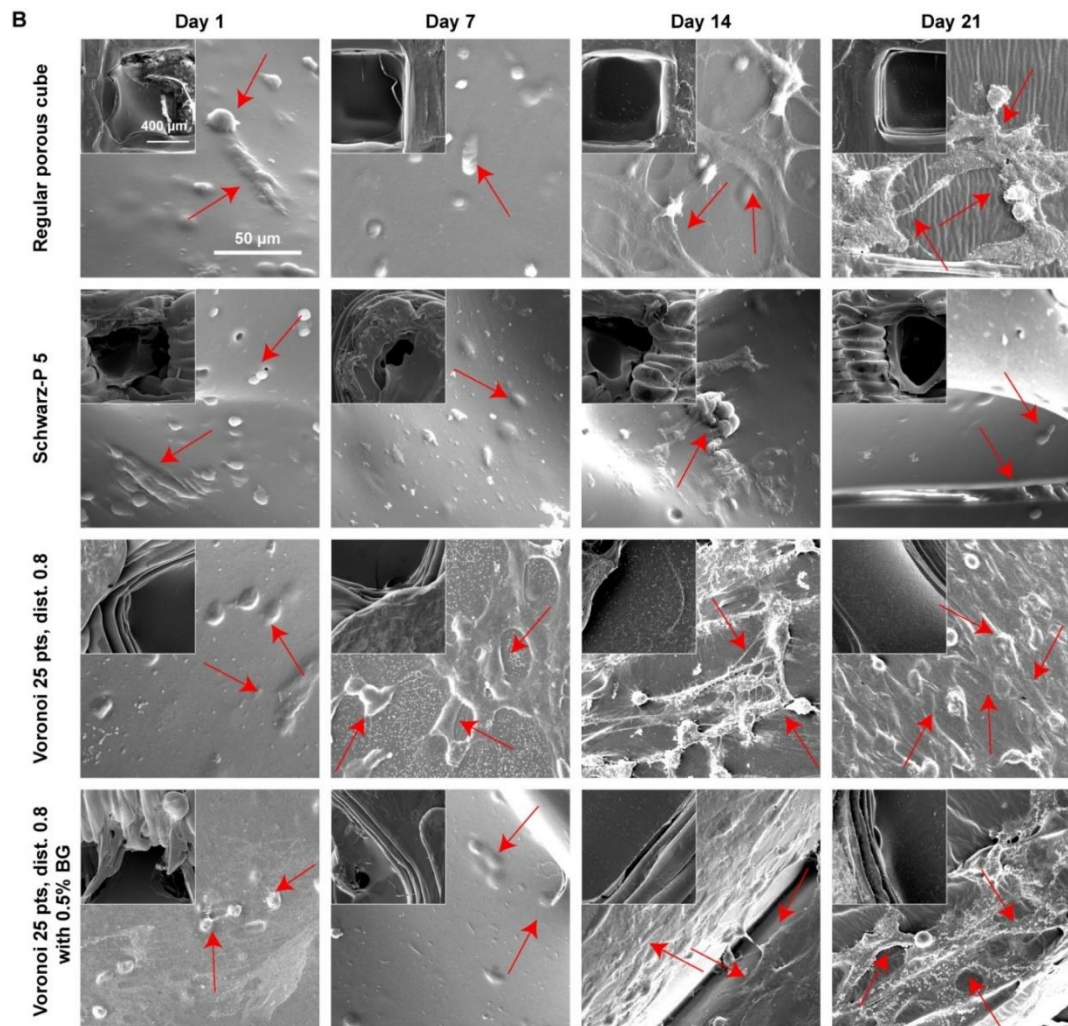
Figure 3.28. (cont'd) SEM results for gel filled 3D PLA scaffolds. A) Image of 100×
magnification. B) Shows 250× and 2000× magnifications. Scale bar is the same in
each column and row. Red arrows are spotting the cells.

3.7 Osteogenic Characterization

3.7.1 Alizarin Red Staining for Ca Deposition

3.7.1.1 Ca Deposition on Disk-Shaped Scaffolds

Alizarin red staining was used to evaluate calcium deposition by hFOB cells. For the disk-shaped scaffolds with 1×10^5 cells seeded and blank ones, the results given in Figures 3.29 and 3.30 were obtained. Figure 3.29 shows 1 and 21- day incubations for blank (unseeded samples in proliferation media), cell seeded samples in proliferation media, and cell seeded samples in osteogenic media. Nine groups of samples were analyzed in this experiment. Figure 3.30 shows the 3 sets and 9 groups on day 21. As it can be observed in Figure 3.29 and clearly in 3.30, after 21 days of incubation, in all groups, the Ca deposition is detected to be more for osteogenic media than proliferation media. The blank samples showed no increase in Ca deposition. It is shown (Figure 3.29) that the BG-containing samples have shown more Ca deposition compared to samples without BG.
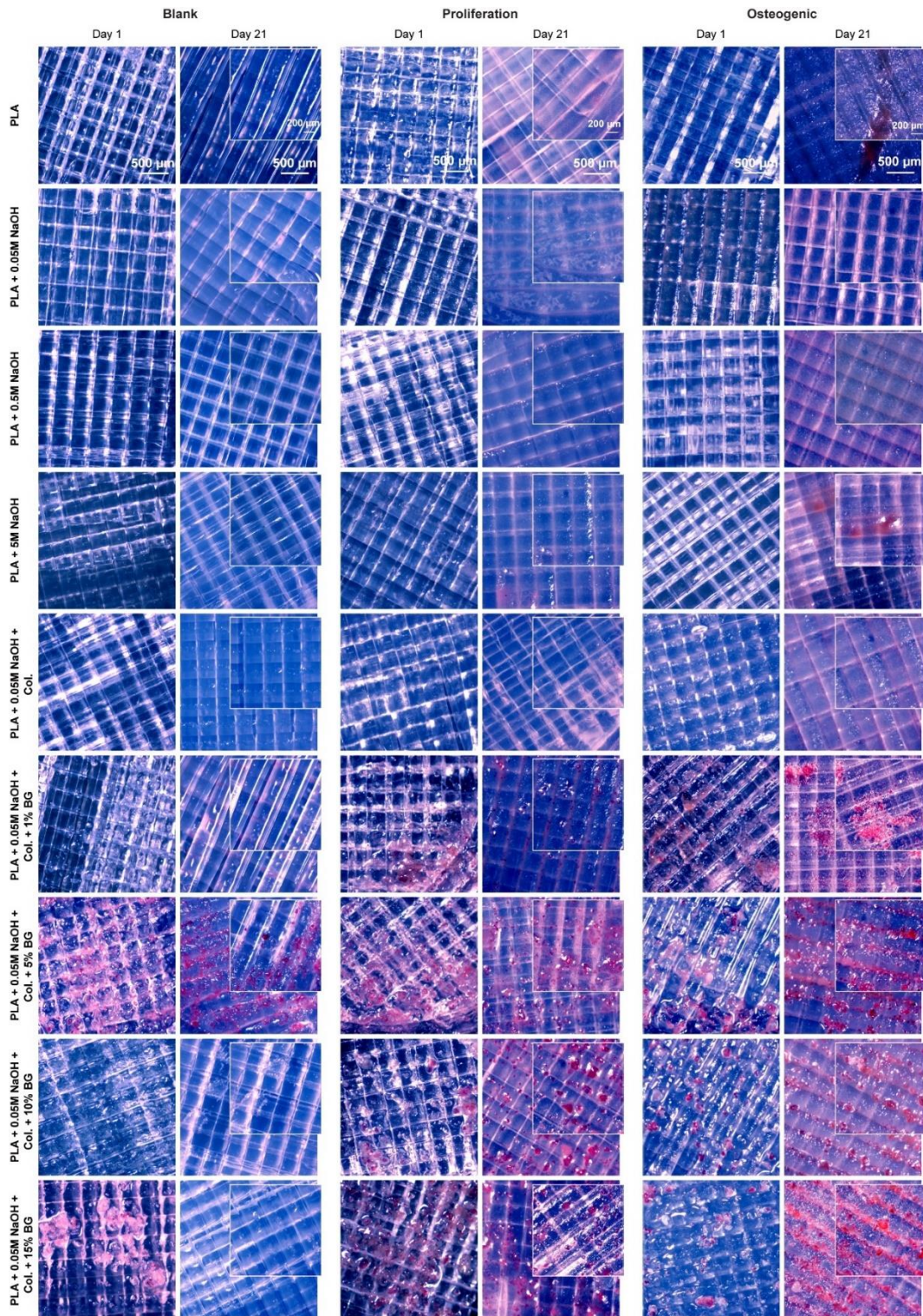
Figure 3.29. Alizarin Red staining for blank samples in proliferation media, samples in proliferation and samples in osteogenic media for days 1 and 21. Scale bar is the

same for the images of the same size. Small images are 4× and larger ones are 2.5× magnifications.
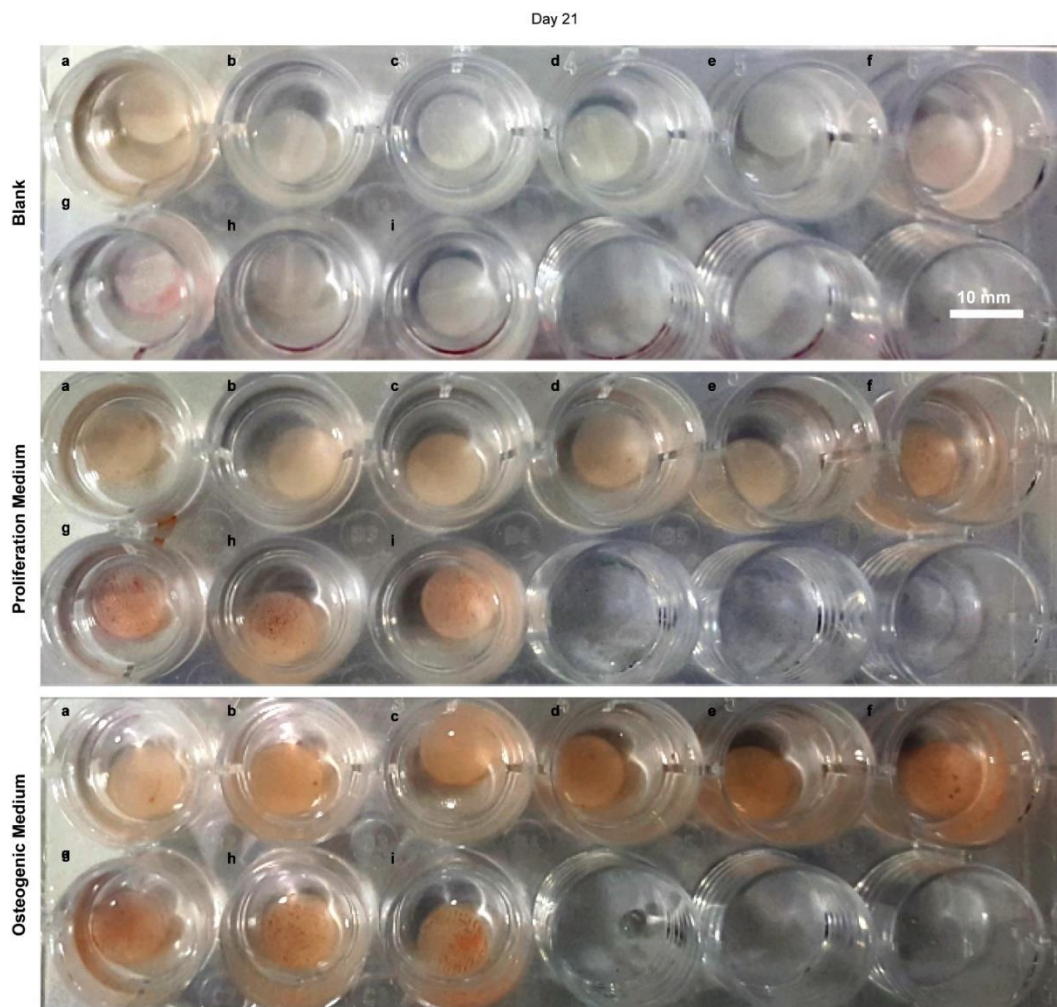
Figure 3.30. Alizarin Red staining for blank samples in proliferation media, samples in proliferation and samples in osteogenic media for day 21. In all sets, a) PLA, b) PLA + 0.05 M NaOH, c) PLA + 0.5 M NaOH, d) PLA + 5 M NaOH, e) PLA+0.05 M NaOH + Col., f) PLA+0.05 M NaOH + Col. + 1% BG, g) PLA+0.05 M NaOH + Col. + 5% BG, h) PLA+0.05 M NaOH + Col. + 10% BG and i) PLA+0.05 M NaOH + Col. + 15% BG.

The effect of BG can also be observed in Figure 3.31A. Cells (35×10^4) were seeded in these samples and incubated in proliferation media. The red color indicates Ca.

128

The red color intensity in BG coated samples is dependent on Ca existing in BG and mineralization. In these samples, the Ca deposition increases by increasing the BG concentration, and mineralization has increased during 14 days of the experiment. However, no significant mineralization is observed for the alkali modified (Figure 3.31B) and collagen coated samples.
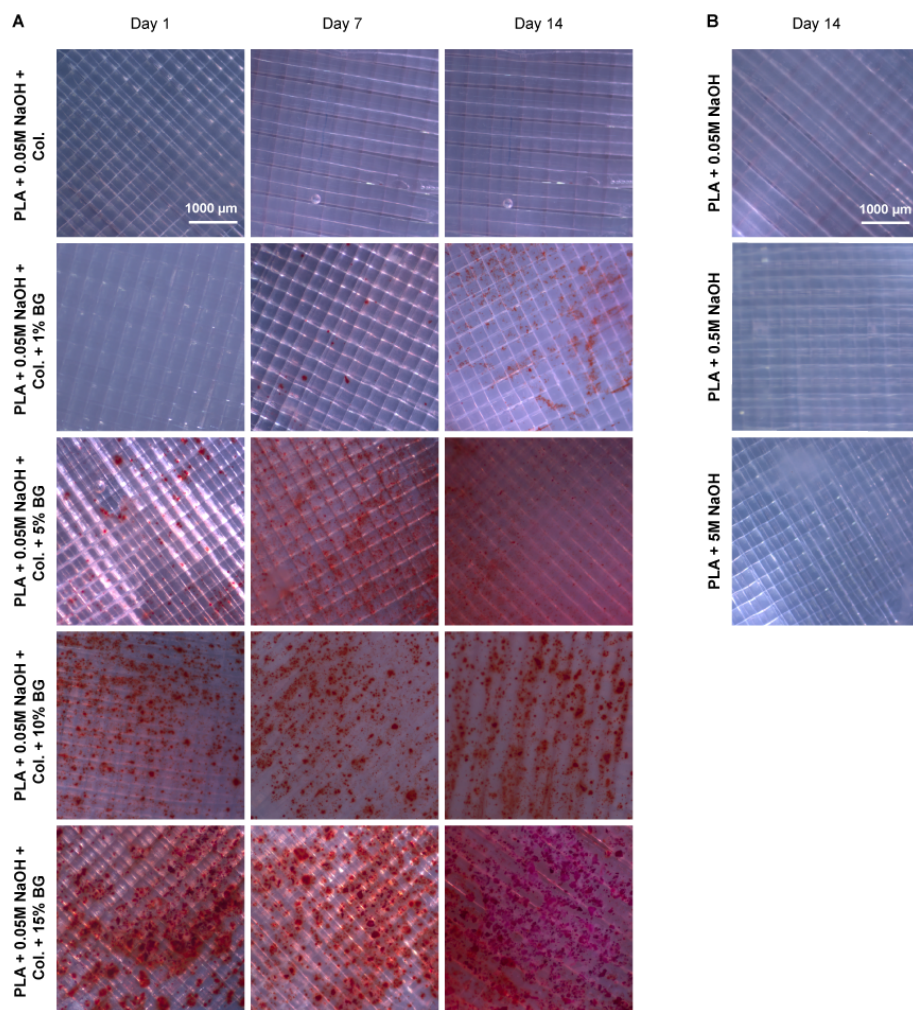
Figure 3.31. Alizarin red staining for alkali modified, collagen and collagen-BG coated scaffolds. A) Collagen and collagen-BG coated scaffolds for days 1, 7, and 14. B) Alkali modified scaffolds for day 14. Scale bar is the same for each column and row.

3.7.1.2 Ca Deposition on 3D PLA Scaffolds

For the collagen-coated selected 9 geometries (Figure 3.32A) the mineralization study shows no considerable Ca deposition on the scaffolds after 21 days of incubation in proliferation medium. Two groups of these 9 groups were selected and studied for further detailed Alizarin red experiments (Figure 3.32B). These results show the significant impact of the collagen-BG coating compared to collagen coating. It can be suggested that for Ca deposition and biomineralization BG-coated samples had increasing trend compared with their blank (unseeded) counterparts. In the blank samples, just the Ca content of BG is observable; therefore, the intensity of the red color is less than cell-seeded scaffolds with biomineralization. According to Figure 3.32 B porous cube collagen and BG coated group demonstrated the most recognizable coloration indicating more Ca deposition than the other geometry with same coating characteristic.
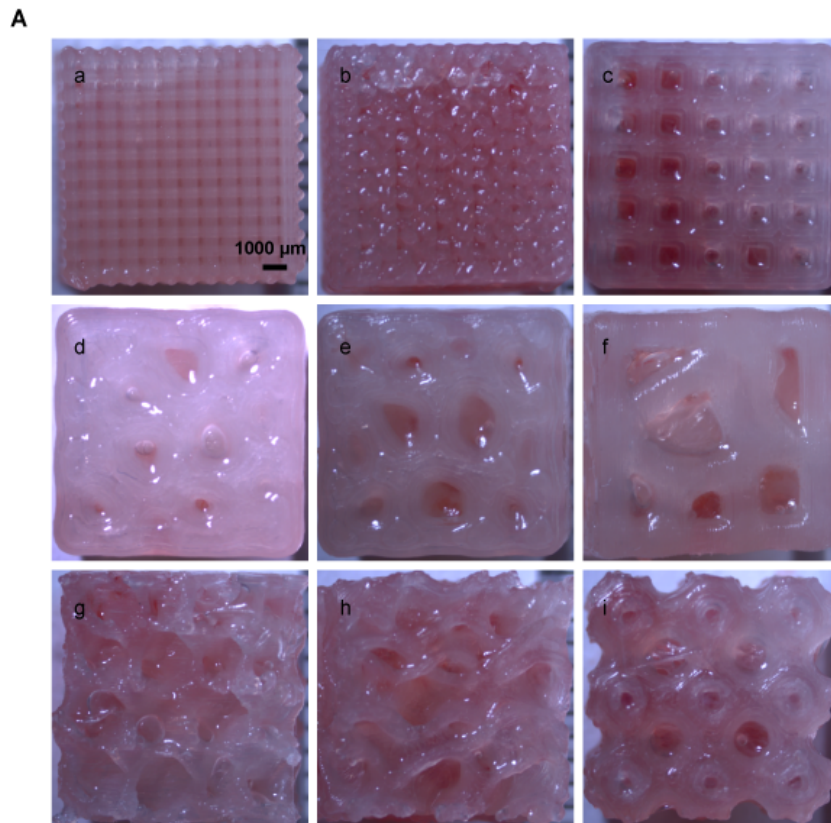
Figure 3.32. Alizarin red staining for 3D printed PLA scaffolds. A) Day 21 for collagen-coated 3D geometries, a) mesh cube, b) cube with regular small pores, c) cube with regular large pores, d) Voronoi 75 points, distance 1.2, e) Voronoi 50 points, distance 1.2, f) Voronoi 25 points, distance 1.2, g) diamond, h) gyroid 4 and i) Schwarz-P 5. B) Days 1, 7, 14 and 21 for two selected groups of 3D geometries (cube with regular large pores & Voronoi 25 points, distance 1.2) with collagen and collagen-BG coating. Scale bar is the same for each column and row.
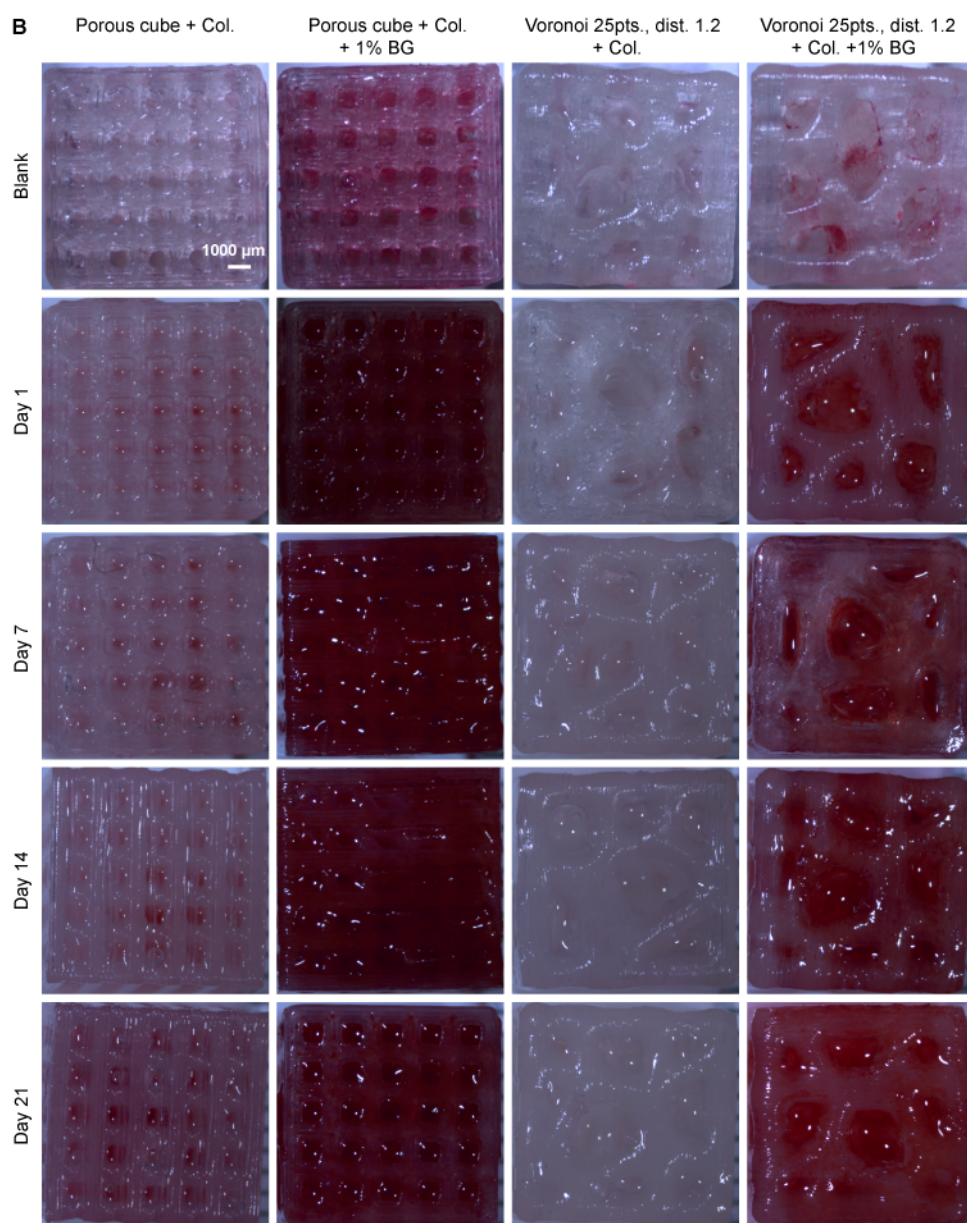
Figure 3.32. (cont'd) Alizarin red staining for 3D printed PLA scaffolds. A) Day 21 for collagen-coated 3D geometries, a) mesh cube, b) cube with regular small pores, c) cube with regular large pores, d) Voronoi 75 points, distance 1.2, e) Voronoi 50 points, distance 1.2, f) Voronoi 25 points, distance 1.2, g) diamond, h) gyroid 4 and i) Schwarz-P 5. B) Days 1, 7, 14 and 21 for two selected groups of 3D geometries (cube with regular large pores & Voronoi 25 points, distance 1.2) with collagen and collagen-BG coating. Scale bar is the same for each column and row.

3.7.1.3 Ca Deposition in Hydrogels

The biomineralization study for hydrogels was conducted for five groups. GelMA with collagen and with collagen and different BG concentration load. The dark brown spot and root structures indicate Ca deposition. The increasing color intensity from day 1 to 21 shows the increasing manner of biomineralization for all the groups. BG containing group (0.5%) (selected group for further 3D studies) shows satisfying deposition of Ca in hydrogel after 21 days. By looking at the images of day 21, the explicit growth of mineralization can be detected for the highest BG-containing groups (0.5% and 1%).
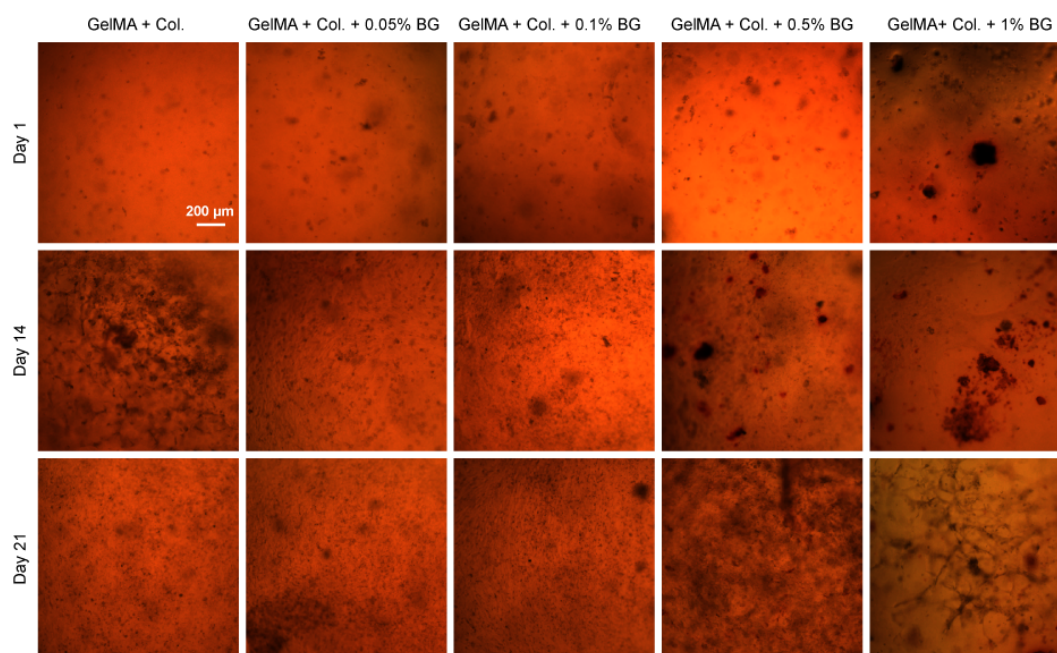
Figure 3.33. Alizarin red staining of GelMA with collagen and different concentrations of BG for days 1. 14 and 21.

3.7.2 Alkaline Phosphatase (ALP) Activity

ALP activity is an indicator of osteogenic differentiation. The ALP experiment was performed for PLA and hydrogel samples for some selected groups in growth media.

However, the decreasing trend from day 7 to day 21 were observed in Figure 3.34 for all groups. This reduction can be due to the enhancement of proliferation in growth media instead of osteogenic activity. The ALP activity of HFOB cells is significantly less than Saos2 cell lines [241]. The decreasing trend from day 7 to 14 is also reported in a study by Lobo et al. for hFOB cells [242]. Figure 3.34A shows the ALP activity per minute for alkaline modified PLA, collagen-coated, and collagen-1% BG coated scaffolds compared to cultured cells in tissue culture plates. Except for the groups marked in the picture, the statistical analysis shows no significant variation for each time point. Analyzing each group in different time point shows a significant decrease of ALP activity for 0.05 M NaOH modified PLA from day 7 to 14 ($P<0.001$) and day 7 to 21 ($P<0.01$), alkali modified and collagen-coated PLA from day 7 to 21, and day 14 to 21 ($P<0.01$), and for TCPS day 14 to 21 ($P<0.05$). The decrease for collagen- BG coated scaffold and increase for TCPS from day 7 to 14 were not significant.

In the case of hydrogels except the first time point (day 7) no significant variation among groups was observed (Figure 3.34B). However, significant ALP decreases between time points were observed for all groups.

These outcomes provide enhancement of ALP activity (an early osteogenic marker) with scaffold and hydrogel groups at early time points compared with TCPS even in growth media.
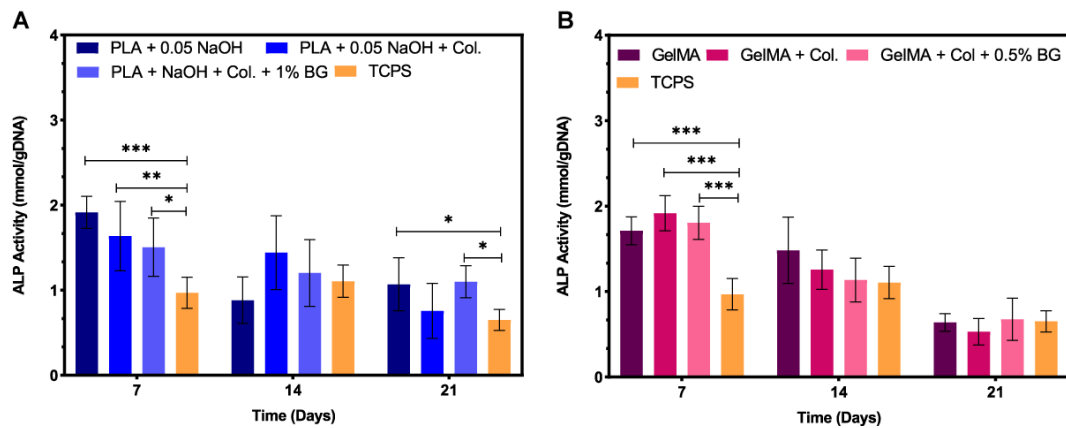
Figure 3.34. ALP activity per minute for the disk-shaped PLA Scaffolds and hydrogels for days 7, 14 and 21. A) PLA scaffolds vs. TCPS. B) Hydrogel groups vs. TCPS. ✱✱✱✱ indicates P≤0.0001, ✱✱✱ means P≤0.001. ✱✱ shows P≤0.01 and finally ✱ means P≤0.05.

3.7.3 Immunostaining

3.7.3.1 Disk-Shaped Scaffolds

Osteoblastic cells growth and differentiation can be divided into 3 main phases proliferation (in first 7 days), ECM maturation (day 7 to day 28), and mineralization (After day 28). Differentiation happens approximately after 7 days of incubation [243].

Confocal imaging and fluorescence intensity analysis for disk -shaped samples with 3 repeats are shown in Figures 3.35 and 3.36. Osteocalcin is a sensitive bone formation marker. The osteocalcin immunostaining intensity analysis (Figure. 3.36A) and confocal micrographs (Figures 3.35A and 3.35B) show a decreasing trend for all the groups from day 7 to day 14, consistent with ALP results since both are early bone formation markers. There are significant differences between almost all samples and nontreated PLA. The collagen and collagen -1% BG coated samples showed the highest osteocalcin release on days 7 and 14.

Osteopontin is calcium-binding protein that can be found in ECM. Osteopontin shows Max between day 7 and 28, as is reported in the literature. This indicates its increasing then decreasing trend during 28 days of incubation [243]. The results for osteopontin intensity (Figure 3.36B) and confocal fluorescence images (Figures 3.35A and 3.35B) represent an increase from day 7 to 14, which is supported by the literature. Two-way ANOVA results show the significant difference between nontreated PLA samples and other treated ones. The collagen and collagen - 1% BG coated samples have the highest values among all groups.

Osteonectin is a protein that is detected during the maturation phase. Osteoblasts secrete this protein during bone formation like osteopontin. Figures 3.35C-D and 3.36C, show a decrease in osteonectin intensity for all groups, which conflicts with the literature.

Collagen type I is an ECM-related protein that indicates osteoblast proliferation, which reaches its maximum during proliferation period [243]. The collagen type I expression decreases for most groups, as shown in Figures 3.35C-D and 3.36D. However, collagen coated scaffolds (Figure 35D and 36D) the collagen intensity is higher than uncoated groups for both day 7 and 14.
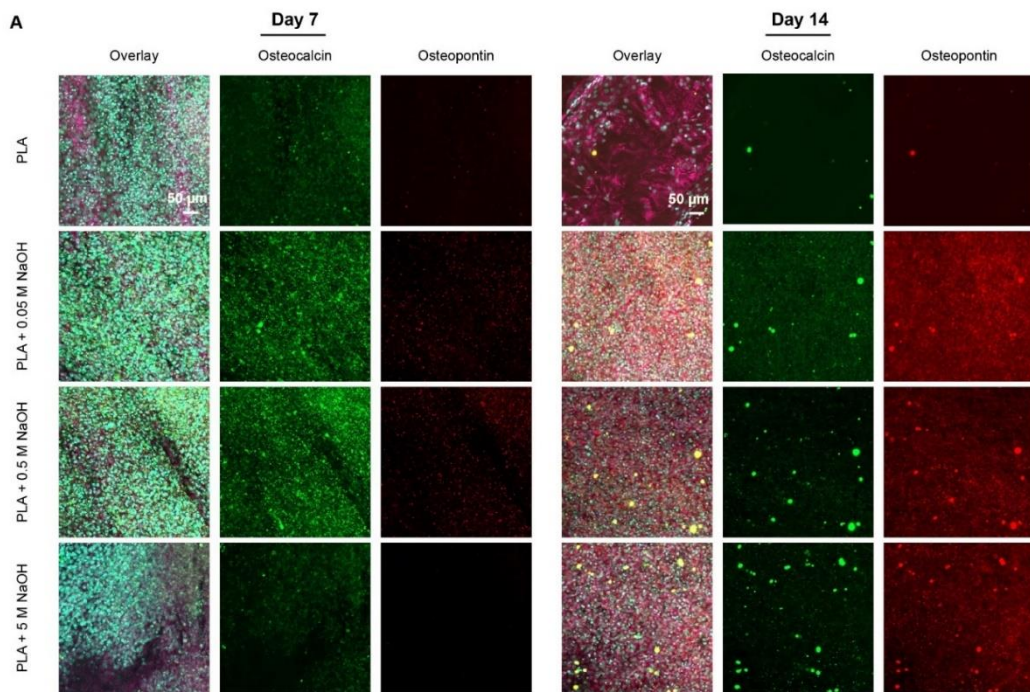
Figure 3.35. Immunostaining images for nine groups of disk-shaped PLA scaffolds. A) osteocalcin and osteopontin markers for PLA and alkali modified PLA groups, B) osteocalcin and osteopontin markers for collagen and collagen-BG containing groups, C) osteonectin and type I collagen markers for PLA and alkali modified PLA groups and D) osteonectin and type I collagen markers for collagen and collagen-BG containing groups. The scale bar is the same for all images.

Figure 3.35 (cont'd) Immunostaining images for nine groups of disk-shaped PLA scaffolds. A) osteocalcin and osteopontin markers for PLA and alkali modified PLA groups, B) osteocalcin and osteopontin markers for collagen and collagen-BG containing groups, C) osteonectin and type I collagen markers for PLA and alkali modified PLA groups and D) osteonectin and type I collagen markers for collagen and collagen-BG containing groups. The scale bar is the same for all images.

Figure 3.35 (cont'd) Immunostaining images for nine groups of disk-shaped PLA scaffolds. A) osteocalcin and osteopontin markers for PLA and alkali modified PLA groups, B) osteocalcin and osteopontin markers for collagen and collagen-BG containing groups, C) osteonectin and type I collagen markers for PLA and alkali modified PLA groups and D) osteonectin and type I collagen markers for collagen and collagen-BG containing groups. The scale bar is the same for all images.

Figure 3.35 (cont'd) Immunostaining images for nine groups of disk-shaped PLA scaffolds. A) osteocalcin and osteopontin markers for PLA and alkali modified PLA groups, B) osteocalcin and osteopontin markers for collagen and collagen-BG containing groups, C) osteonectin and type I collagen markers for PLA and alkali modified PLA groups and D) osteonectin and type I collagen markers for collagen and collagen-BG containing groups. The scale bar is the same for all images.

Figure 3.36. Fluorescence intensity for osteocalcin, osteopontin, osteonectin and collagen type I for days 7 and 14.

3.7.3.2   3D Scaffolds

The immunostaining results for different geometries of collagen coated 3D PLA scaffolds for day 21 is represented in Figure 3.37. In order to observe the osteogenic activity of the cells in a day other than 7 and 14, day 21 was chosen for the 3D scaffolds. For these groups, just osteocalcin and osteopontin markers were used and the 3D scaffolds have shown osteogenic differentiation according to these markers' results. The confocal micrograph results show the presence of osteocalcin and osteopontin on day 21.
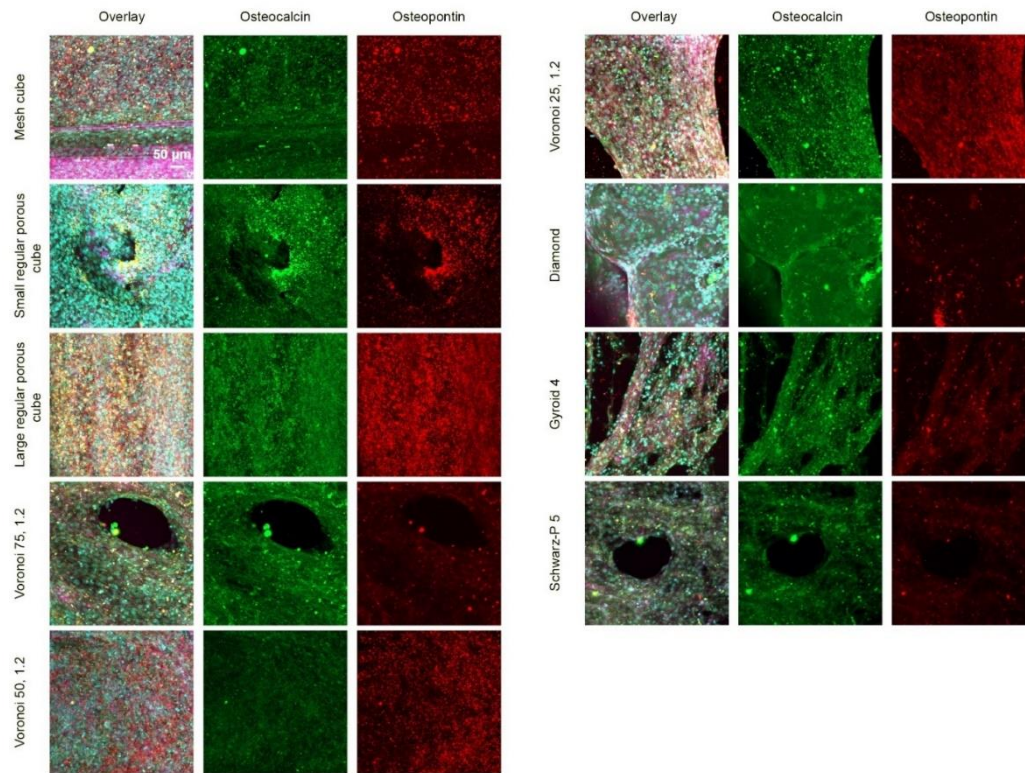
Figure 3.37. Immunostaining assay for 3D PLA scaffold with different collagen coated geometries. The scale bar is the same for all images.

3.7.3.3   Control Group (TCPS) for Disk-shaped Scaffold

As a control group for samples, 35×10^5 cells were seeded in 48 well plates. Figure 3.38 shows confocal images for 4 markers. It can be seen that osteocalcin and osteopontin proteins are increasing until 14 days and then decreasing (Figure 3.38A) and collagen type I increases in first 7 days then decreases (Figure 3.38B). These results are supported by the literature [243]. However, osteonectin displays a different trend than a few studies on this subject.
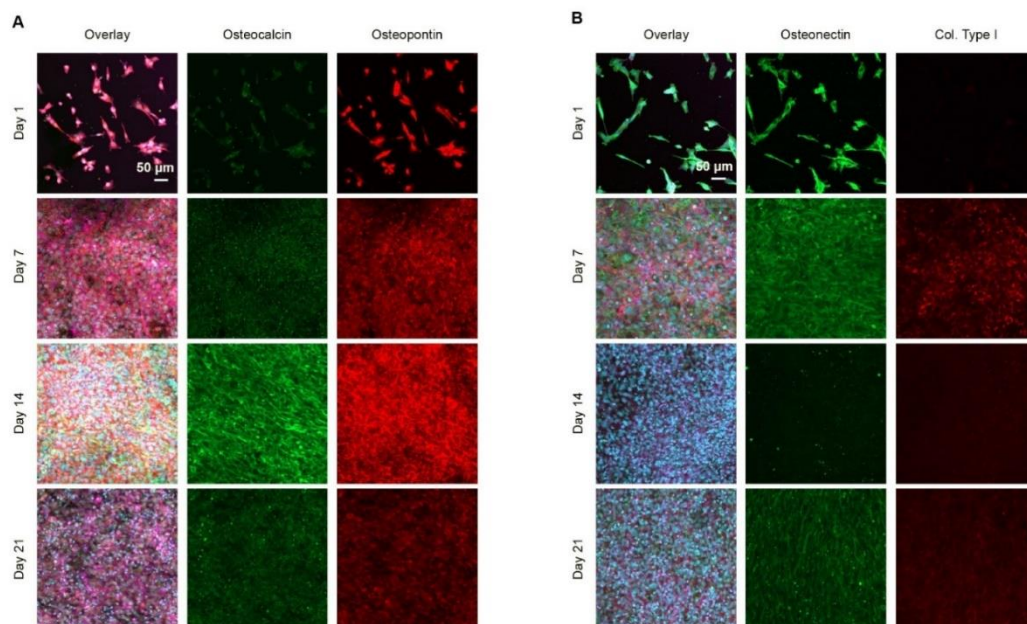
Figure 3.38. Immunostaining assay for control groups for days 1, 7, 14 and 21. A) osteocalcin and osteopontin markers and B) osteonectin and collagen type I markers. Scale bar is the same for all images.

3.7.4 Energy-Dispersive Spectroscopy (EDS) Analysis

The Ca and P elements produced by populated cells on the scaffolds were analyzed using EDS analysis during SEM. Calcium phosphate crystals act as nucleation factors in hydroxyapatite deposition in bone formation. Almost all of the calcium orthophosphates with different Ca-P ratios such as tricalcium phosphate (TCP), octa calcium phosphate (OCP), amorphous calcium phosphate (ACP), dicalcium phosphate dihydrate (DCPD), mono calcium phosphate monohydrate (MCPM) and mono calcium phosphate anhydrous (MCPA) have been used in biomedical applications. They are reported as precursors for making HA as well. However, these precursors are unstable and it is not easy to detect them during the biomineralization process [244]. The Ca/P ratio of stoichiometric HA is reported as 1.67. This ratio is 1.5 for TCP, 1.33 for OCP, 1 for DCPD, and 1.2-2.2 for ACP [245].

The EDS results are expressed as Ca/P ratios in Table 3.4 and Figure 3.39. for cell culture experiments with samples incubated in differentiation media, 5% and 15% BG containing groups Ca/P ratio were reported as 1.25 and 1.36 respectively after 21 days of incubation. This value approximately matches the one for OCP (1.33). OCP is produced in early stages of biomineralization, and it can be hydrolyzed to HA. The formation of OCP can be considered as a sign of biomineralization and differentiation. The Ca/P ratio for 1% BG containing sample is 0.64, which is close to MCPM or MCPA (0.5) and for 10% BG containing sample is 1.09, which is close to DCPD. MCPM is considered the most soluble calcium phosphate and HA precursor [246]. The samples without BG Ca/P ratio could not be calculated since P or both Ca and P are not detected.

For cell culture experiments with samples incubated in proliferation media, Ca/P ratio for the sample with 1% BG is 0.78, which is closer to DCPD (1) and for the other samples containing 5%, 10% and 15% BG are 1.43, 1.41 and 1.54, respectively. These values are closer to Ca/P ratio of tricalcium phosphate (1.5).

Ca deposition results obtained from Alizarin red assay (Figure 3.30) indicates more Ca deposition in samples incubated in osteogenic media than in proliferation media after 21 days. However, the Ca/P ratios for each group of samples incubated in proliferation media are higher than those in osteogenic media after 21 days of incubation. Also, Alizarin red assay shows Ca deposition in groups not containing BG such as 0.05 M NaOH modified PLA scaffold, while Ca is not detected in this sample in EDS analysis. In blank samples, Ca and P are not detected even for BG containing Ca and P samples.

EDS is not an accurate method for elemental analysis. Moreover, it is analyzed with just one repeat.

Figures 3.40 and 3.41 show the SEM micrographs taken during EDS analysis for samples in proliferation media and osteogenic media after 21 days. As it can be seen from the SEM images for day 21 the mineral deposition can be seen especially for BG containing groups in both proliferation and osteogenic media.

Table 3.4 Ca/P ratio in six groups of samples in three sets of experiments (blank, proliferation, and differentiation media). The values are reported on days 1 and 21.

Samples	Blank samples in proliferation media Ca/P		1×10^5 Cells/sample in proliferation media Ca (At%) P (At%) Ca/P		1×10^5 Cells/sample in osteogenic media Ca (At%) P (At%) Ca/P	
	Day 1	Day 21	Day 1	Day 21	Day 1	Day 21
PLA	-	-	-	Ca is not detected P: 0.36	-	Ca is not detected P: 0.26
PLA+0.05M NaOH+Col.	-	-	-	Ca is not detected P: 0.25	-	Ca is not detected P: 0.28
PLA+0.05M NaOH+Col.+1% BG	Ca and P are not detected	Ca and P are not detected	Ca and P are not detected	Ca/P: 0.78	Ca and P are not detected	Ca/P: 0.64
PLA+0.05M NaOH+Col.+5% BG	Ca and P are not detected	Ca and P are not detected	Ca/P: 1.3	Ca/P: 1.43	Ca/P: 1.41	Ca/P: 1.25
PLA+0.05M NaOH+Col.+10 % BG	Ca and P are not detected	Ca and P are not detected	Ca and P are not detected	Ca/P: 1.41	Ca/P:1.3	Ca/P: 1.09
PLA+0.05M NaOH+Col.+15 % BG	Ca and P are not detected	Ca and P are not detected	Ca/P: 2.08	Ca/P: 1.54	Ca and P are not detected	Ca/P: 1.36
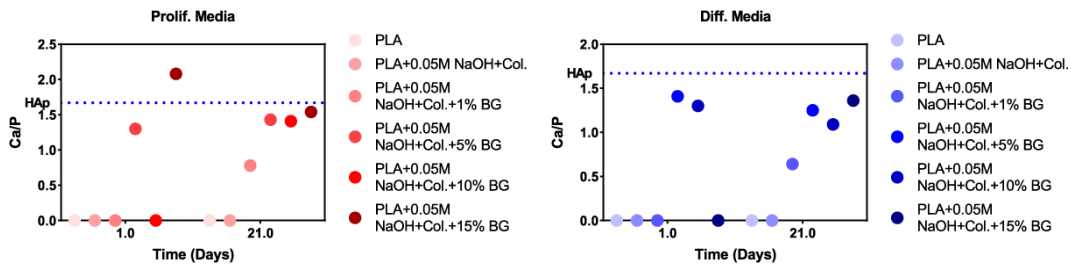
Figure 3.39. Ca/P ratio as a graph for six groups of samples in proliferation media (left) and osteogenic media (right).
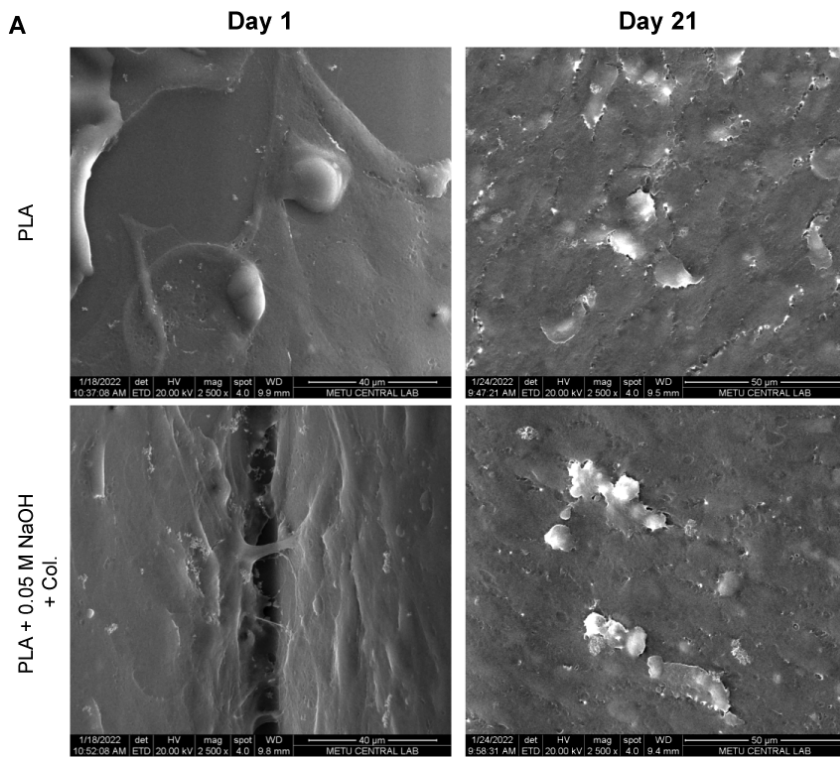
Figure 3.40. SEM micrographs for six groups of samples incubated in proliferation media for days 1 and 21. A) PLA without any treatment and PLA + 0.05 M NaOH and B) alkali modified and collagen-BG coated samples with different BG concentrations.
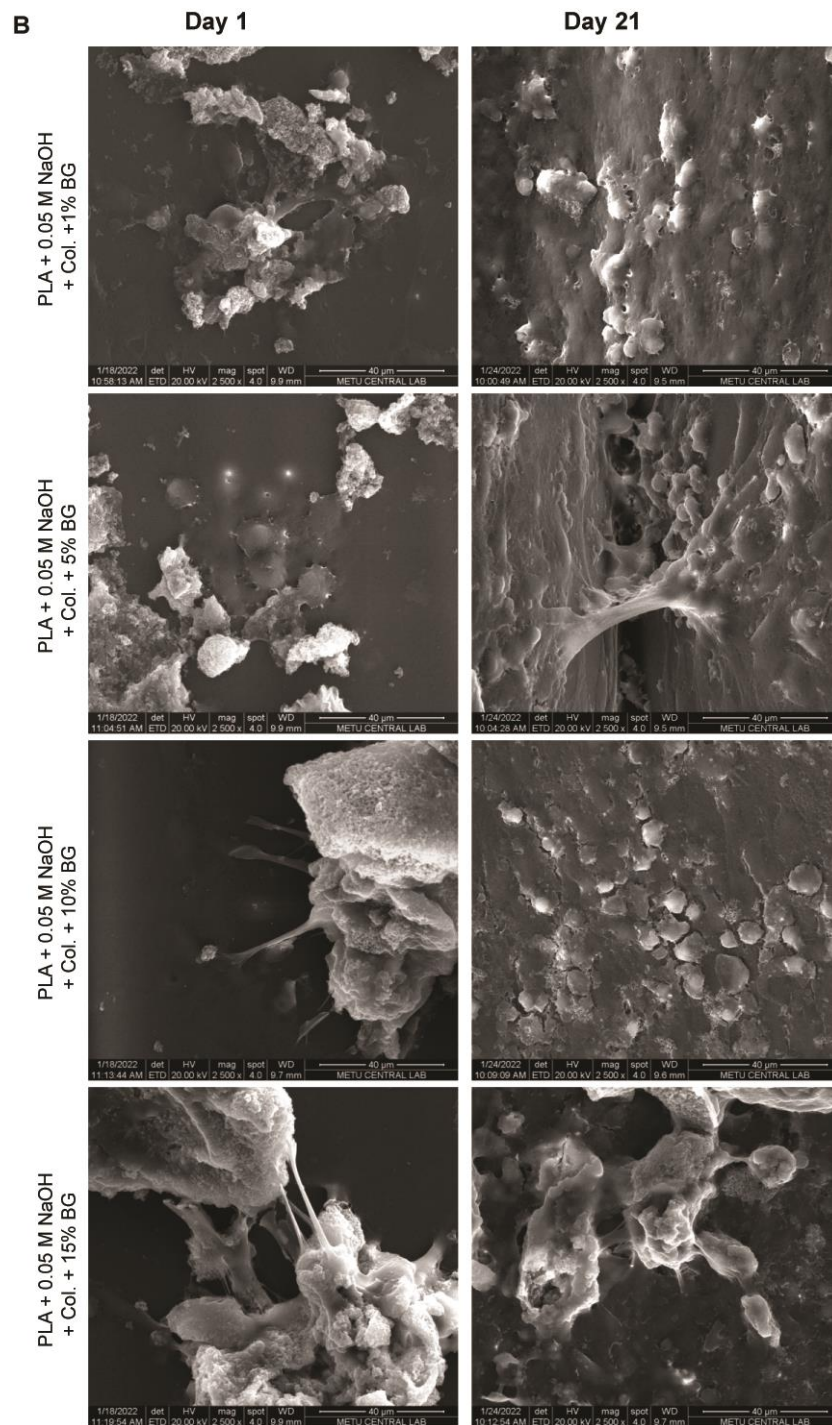
Figure 3.40. (cont'd) SEM micrographs for six groups of samples incubated in proliferation media for days 1 and 21. A) PLA without any treatment and PLA + 0.05 M NaOH and B) alkali modified and collagen-BG coated samples with different BG concentrations.
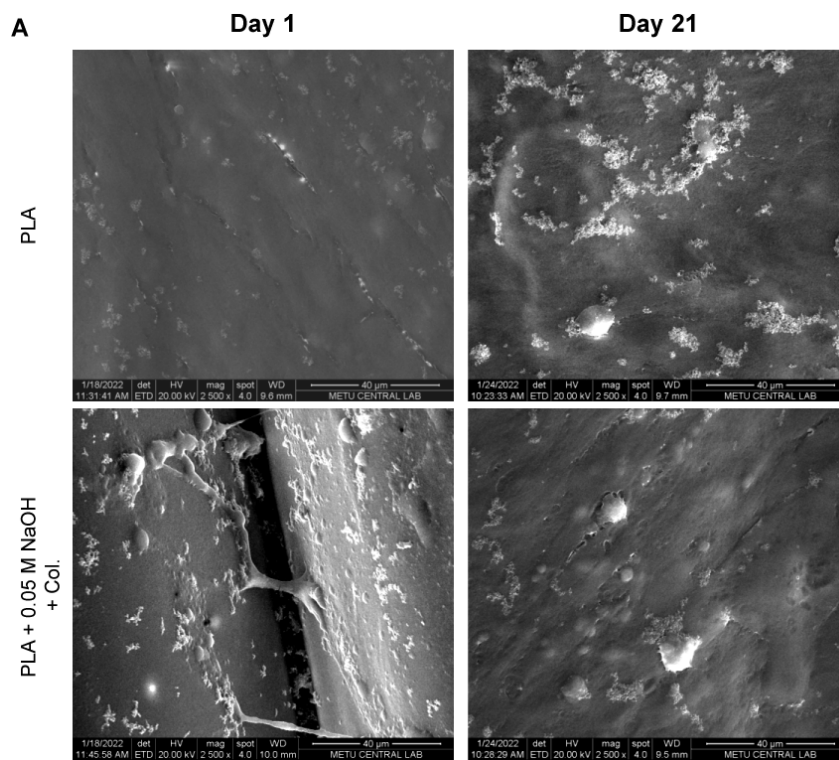
Figure 3.41. SEM micrographs for six groups of samples incubated in differentiation media for days 1 and 21. A) PLA without any treatment and PLA + 0.05 M NaOH and B) alkali modified and collagen-BG coated samples with different BG concentrations.
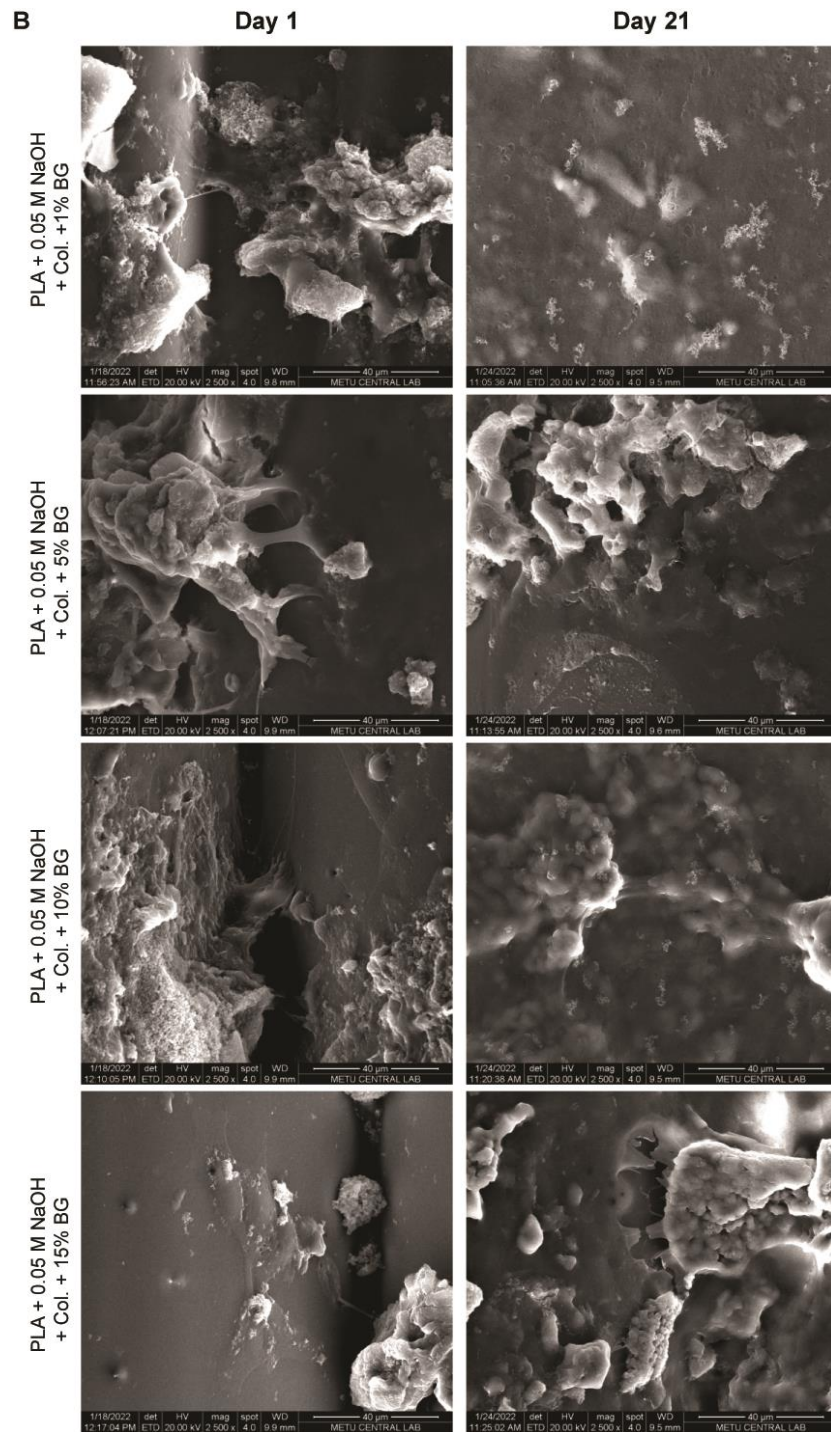
Figure 3.41. (cont'd) SEM micrographs for six groups of samples incubated in differentiation media for days 1 and 21. A) PLA without any treatment and PLA + 0.05 M NaOH and B) alkali modified and collagen-BG coated samples with different BG concentrations.

CHAPTER 4

CONCLUSIONS AND FUTURE WORK

4.1   Conclusions

Bone tissue engineering is a growing field of research. Today scaffolds with good mechanical strength mimicking bone ECM biochemistry and biodegradable biomaterials to allow tissue growth are in high need. This study combined the engineering aspects of mechanical design and manufacturing practices with biomaterials knowledge to obtain a novel bone scaffold.

In this study, disk-shaped and various three-dimensional regular geometries were designed via CAD tools. PLA-based porous scaffolds were 3D printed by FDM. CAD and FDM methods have been shown as great candidates for modeling and producing scaffolds with controlled geometry and porosity. CAD allows precise modeling of the desired designs, and both size and geometry can be controlled to the point. These methods allow one-of-a-kind production of 3D structures if desired (without the need for mold production) and also a replication of products with high fidelity. The compressive modulus of the designed PLA porous scaffolds was in the range of $39\pm8.6 - 504\pm13.22$ MPa, which is compatible with human trabecular bone (10-900 MPa).

This study is composed of two parts. In the first part, disk-shaped and candidate 3D scaffolds were alkali modified and coated with collagen and collagen-BG with different concentrations of BG (1, 5, 10, and 15 w/v%). HFOB cells were seeded on the scaffolds for further *in vitro* studies. Collagen and BG coating of the disk-shaped PLA scaffolds presented better osteogenic results compared to untreated surfaces. Ca deposition for all the groups was increased by incubating in osteogenic media compared to proliferation media. The collagen and collagen-1% BG coated groups represented better osteocalcin and osteopontin differentiation results.

Nine groups of collagen coated 3D structures, regardless of different porosities and pore shapes showed goof cell proliferation and migration results.

In the second part of the study, three candidate 3D PLA scaffolds were filled with collagen and collagen-BG (0.05, 0.1, 0.5, and 1 w/v%) loaded GelMA hydrogel to provide an interconnective network and facilitate cell migration and proliferation. Highly porous trabecular like structure (Voronoi-type structure) filled with collagen loaded GelMA and collagen-0.5% BG loaded GelMA have shown better cell viability, proliferation and migration among three groups of geometries. The positive effect of BG in osteogenic activities of cells was also observed in hydrogels.

To sum up, the novel scaffolds -surface-treated 3D PLA scaffolds and GelMA loaded 3D PLA scaffolds- were biocompatible and suitable for cell adhesion, proliferation, and to some extent differentiation. Therefore, they have a great potential to go for *in vivo* studies. The Voronoi structure can be considered a candidate bone scaffold for further studies.

4.2   Future work

The research into the osteogenicity of the samples are still under investigation. First of all, a more in-depth ALP activity analysis could be performed. ALP activity for the samples incubated in osteogenic media can be compared to proliferation media. Second, the ALP activity of the cells in the osteogenic medium could be performed in more details (more time points and sample types). Unfortunately, due to the ALP analytes' supply chain issues, a detailed analysis was not performed.

The proposed scaffolds are good candidates for *in vivo* studies. Therefore, the next step can be the in vivo studies before clinical research.

Different cell types such as BMSCs and their differentiation can also be investigated using designed scaffolds.

PLA-BG composites can be used as ink for 3D printing instead of coating the PLA scaffolds with BG. In this method, the consistency of the BG concentration during the whole experiment period is ensured.

REFERENCES

[1] X. Wang and S. Puram, "The toughness of cortical bone and its relationship with age," *Ann. Biomed. Eng.*, vol. 32, no. 1, pp. 123–135, 2004.

[2] S. Preethi Soundarya, A. Haritha Menon, S. Viji Chandran, and N. Selvamurugan, "Bone tissue engineering: Scaffold preparation using chitosan and other biomaterials with different design and fabrication techniques," *Int. J. Biol. Macromol.*, vol. 119, pp. 1228–1239, 2018.

[3] A. S. Alagöz, "Bone Tissue Engineering Using Macroporous PHA-PLA and PHBV Scaffolds Produced by Additive Manufacturing and Wet Spinning," Middle East Technical University, 2016.

[4] "Skeletal System." [Online]. Available: https://connortodd.weebly.com/anatomy.html. [Accessed: 11-Oct-2021].

[5] T. Kovářík, T. Křenek, P. Bělský, and J. Šesták, "Biomaterials and Nanotechnology Approach to Medical Enhancement," *Therm. Phys. Therm. Anal.*, no. November 2020, pp. 449–470, 2017.

[6] T. Arnett, "Bone Structure and Bone Remodelling," London: University College London, 2014.

[7] U. Jammalamadaka and K. Tappa, "Recent advances in biomaterials for 3D printing and tissue engineering," *J. Funct. Biomater.*, vol. 9, no. 1, 2018.

[8] T. Bian, K. Zhao, Q. Meng, Y. Tang, H. Jiao, and J. Luo, "The construction and performance of multi-level hierarchical hydroxyapatite (HA)/collagen composite implant based on biomimetic bone Haversian motif," *Mater. Des.*, vol. 162, pp. 60–69, 2019.

[9] R. Langer and J. P. Vacanti, "Tissue engineering," *Science*, vol. 260, no. 5110, pp. 920–926, 1993.

[10]   M. I. Santos and R. L. Reis, "Vascularization in bone tissue engineering: Physiology, current strategies, major hurdles and future challenges," *Macromol. Biosci.*, vol. 10, no. 1, pp. 12–27, 2010.

[11]   M. M. Stevens, "Biomaterials for bone tissue engineering," *Mater. Today*, vol. 11, no. 5, pp. 18–25, 2008.

[12]   Z. Y. Zhang, S. H. Teoh, J. H. P. Hui, N. M. Fisk, M. Choolani, and J. K. Y. Chan, "The potential of human fetal mesenchymal stem cells for off-the-shelf bone tissue engineering application," *Biomaterials*, vol. 33, no. 9, pp. 2656–2672, 2012.

[13]   R. Siddappa, R. Licht, C. V. Blitterswijk, and J. D. Boer, "Donor Variation and Loss of Multipotency during In Vitro Expansion of Human Mesenchymal Stem Cells for Bone Tissue Engineering," *Wiley Intersci.*, pp. 1029–1041, 2007.

[14]   J. R. Mauney, D. Ph, V. Volloch, D. Ph, D. L. Kaplan, and D. Ph, "Role of Adult Mesenchymal Stem Cells in Bone Tissue-Engineering Applications: Current Status and Future Prospects," *Tissue Eng.*, vol. 11, no. 5/6, pp. 787–802, 2005.

[15]   B. N. Teixeira, P. Aprile, R. H. Mendonça, D. J. Kelly, and R. M. da S. M. Thiré, "Evaluation of bone marrow stem cell response to PLA scaffolds manufactured by 3D printing and coated with polydopamine and type I collagen," *J. Biomed. Mater. Res. - Part B Appl. Biomater.*, vol. 107, no. 1, pp. 37–49, 2019.

[16]   J. Venugopal, P. Vadgama, T. S. Sampath Kumar, and S. Ramakrishna, "Biocomposite nanofibres and osteoblasts for bone tissue engineering," *Nanotechnology*, vol. 18, no. 5, 2007.

[17]   M. P. Prabhakaran, J. Venugopal, and S. Ramakrishna, "Electrospun nanostructured scaffolds for bone tissue engineering," *Acta Biomater.*, vol. 5, no. 8, pp. 2884–2893, 2009.

[18]   Y. Zhang, J. R. Venugopal, A. El-turki, S. Ramakrishna, B. Su, and T. C. Lim, "Electrospun biomimetic nanocomposite nanofibers of hydroxyapatite/chitosan for bone tissue engineering," *Biomaterials*, vol. 29, pp. 4314–4322, 2008.

[19]   D. Dufrane, "Impact of Age on Human Adipose Stem Cells for Bone Tissue Engineering," *Cell Transplant.*, vol. 26, no. 9, pp. 1496–1504, 2017.

[20]   D. W. Hutmacher and M. Sittinger, "Periosteal Cells in Bone Tissue Engineering," *Tissue Eng.*, vol. 9, p. S-45-S64, 2003.

[21]   K. Lee, E. A. Silva, and D. J. Mooney, "Growth factor delivery-based tissue engineering: General approaches and a review of recent developments," *J. R. Soc. Interface*, vol. 8, no. 55, pp. 153–170, 2011.

[22]   B. Meinel, L. Zoidis, E. Zapf, J. Hassa, P. Hottiger, M. O. Auer, and J. A. Von Rechenberg, "Localized insulin-like growth factor I delivery to enhance new bone 95 formation," *Bone*, vol. 33, no. 4, pp. 660–672, 2003.

[23]   P. Yilgor, K. Tuzlakoglu, R. L. Reis, N. Hasirci, and V. Hasirci, "Incorporation of a sequential BMP-2/BMP-7 delivery system into chitosan-based scaffolds for bone tissue engineering," *Biomaterials*, vol. 30, no. 21, pp. 3551–3559, 2009.

[24]   D. Kaigler, G. Avila, L. Wisner-Lynch, M. L. Nevins, M. Nevins, G. Rasperini, S. E. Lynch, and W. V. Giannobile, "Platelet-derived growth factor applications in periodontal and peri-implant bone regeneration," *Expert Opin. Biol. Ther.*, vol. 11, no. 3, pp. 375–385, 2011.

[25]   D. Qu, J. Li, Y. Li, Y. Gao, Y. Zuo, Y. Hsu, and J. Hu, "Angiogenesis and osteogenesis enhanced by bFGF ex vivo gene therapy for bone tissue engineering in reconstruction of calvarial defects," *J. Biomed. Mater. Res. - Part A*, vol. 96 A, no. 3, pp. 543–551, 2011.

[26]   G. Chen, C. Deng, and Y. P. Li, "TGF-β and BMP signalling in osteoblast differentiation and bone formation," *International Journal of Biological Sciences*, vol. 8, no. 2. pp. 272–288, 2012.

[27]   T. Luo, W. Zhang, B. Shi, X. Cheng, and Y. Zhang "Enhanced bone regeneration around dental implant with bone morphogenetic protein 2 gene and vascular endothelial growth factor protein delivery," *Clin. Oral Implants Res.*, vol. 23, no. 4, pp. 467–473, 2012.

[28]   F. Langenbach and J. Handschel, "Effects of dexamethasone, ascorbic acid and β -glycerophosphate on the osteogenic differentiation of stem cells in vitro," *Stem Cell Res. Ther.*, vol. 4, p. 117, 2013.

[29]   S. Ahdjoudj, F. Lasmoles, B. O. Oyajobi, A. Lomri, P. Delannoy, and P. J. Marie, "Reciprocal control of osteoblast/chondroblast and osteoblast/adipocyte differentiation of multipotential clonal human marrow stromal F/STRO-1+ cells," *J. Cell. Biochem.*, vol. 81, no. 1, pp. 23–38, 2001.

[30]   A. Haleem, M. Javaid, R. H. Khan, and R. Suman, "3D printing applications in bone tissue engineering," *J. Clin. Orthop. Trauma*, vol. 11, pp. S118–S124, 2020.

[31]   H. Yoshikawa and A. Myoui, "Bone tissue engineering with porous hydroxyapatite ceramics," *J. Artif. Organs*, vol. 8, no. 3, pp. 131–136, 2005.

[32]   L. Zhang, G. Yang, B. N. Johnson, and X. Jia, "Three-dimensional (3D) printed scaffold and material selection for bone repair," *Acta Biomater.*, vol. 84, pp. 16–33, Jan. 2019.

[33]   F. Dehghani and N. Annabi, "Engineering porous scaffolds using gas-based techniques," *Curr. Opin. Biotechnol.*, vol. 22, no. 5, pp. 661–666, 2011.

[34]   N. Sultana and M. Wang, "PHBV/PLLA-based composite scaffolds fabricated using an emulsion freezing/freeze-drying technique for bone tissue

engineering: Surface modification and in vitro biological evaluation," *Biofabrication*, vol. 4, no. 1, 2012.

[35]   L. Roseti, V. Parisi, M. Petretta, C. Cavallo, G. Desando, I. Bartolotti, and B. Grigolo, "Scaffolds for Bone Tissue Engineering: State of the art and new perspectives," *Mater. Sci. Eng. C*, vol. 78, pp. 1246–1262, 2017.

[36]   D. Puppi, F. Chiellini, A. M. Piras, and E. Chiellini, "Polymeric materials for bone and cartilage repair," *Prog. Polym. Sci.*, vol. 35, no. 4, pp. 403–440, 2010.

[37]   H. F. Ko, C. Sfeir, and P. N. Kumta, "Novel synthesis strategies for natural polymer and composite biomaterials as potential scaffolds for tissue engineering," *Philos. Trans. R. Soc. A Math. Phys. Eng. Sci.*, vol. 368, no. 1917, pp. 1981–1997, 2010.

[38]   C. X. F. Lam, X. M. Mo, S. H. Teoh, and D. W. Hutmacher, "Scaffold development using 3D printing with a starch-based polymer," *Mater. Sci. Eng. C*, vol. 20, no. 1–2, pp. 49–56, 2002.

[39]   G. A. Di Lullo, S. M. Sweeney, J. Körkkö, L. Ala-Kokko, and J. D. San Antonio, "Mapping the ligand-binding sites and disease-associated mutations on the most abundant protein in the human, type I collagen," J. *Biol. Chem.*, vol. 277, no. 6, pp. 4223–4231, 2002.

[40]   R. H. Bogue, "Conditions Affecting the Hydrolysis of Collagen to Gelatin," *Ind. Eng. Chem.*, vol. 15, no. 11, pp. 1154–1159, 1923.

[41]   S. Ricard-Blum, "The Collagen Family," *Cold Spring Harb. Perspect. Biol.*, vol. 3, no. 1, pp. 1–19, 2011.

[42]   M. Ashokkumar and P. M. Ajayan, "Materials science perspective of multifunctional materials derived from collagen," *International Materials Reviews,* vol. 66, no. 3. pp. 160–187, 2021.

157

[43] K. M. Courtney Townsend, R. Daniel Beauchamp, and B. Mark Evers, "Wound Healing," Sabiston Textbook of Surgery, The Biological Basis of Modern Surgical Practice, 20th ed., 2016.

[44] S. A. Sell, P. S. Wolfe, K. Garg, J. M. McCool, I. A. Rodriguez, and G. L. Bowlin, "The use of natural polymers in tissue engineering: A focus on electrospun extracellular matrix analogues," *Polymers (Basel).*, vol. 2, no. 4, pp. 522–553, 2010.

[45] A. Aravamudhan, D. M. Ramos, J. Nip, M. D. Harmon, R. James, M. Deng, C. T. Laurencin, X. Yu, and S. G. Kumbar, "Cellulose and collagen derived micro-nano structured scaffolds for bone tissue engineering," *J. Biomed. Nanotechnol.*, vol. 9, no. 4, pp. 719–731, 2013.

[46] M. B. Keogh, F. J. O'Brien, and J. S. Daly, "A novel collagen scaffold supports human osteogenesis - Applications for bone tissue engineering," *Cell Tissue Res.*, vol. 340, no. 1, pp. 169–177, 2010.

[47] A. Ahmadi, S. L. Thorn, E. I. Alarcon, M. Kordos, D. T. Padavan, T. Hadizad, G. O. Cron, R. S. Beanlands, J. N. Dasilva, M. Ruel, R. A. deKemp, and E. J. Suuronen, "PET imaging of a collagen matrix reveals its effective injection and targeted retention in a mouse model of myocardial infarction," *Biomaterials*, vol. 49, pp. 18–26, 2015.

[48] S. S. Johl and R. A. Burgett, "Dermal filler agents: A practical review," *Curr. Opin. Ophthalmol.*, vol. 17, no. 5, pp. 471–479, 2006.

[49] M. Mian, F. Beghè, and E. Mian, "Collagen as a pharmacological approach in wound healing," *Int. J. Tissue React.*, vol. 14, pp. 1–9, 1992.

[50] J. L. Drury and D. J. Mooney, "Hydrogels for tissue engineering scaffold design variablesand applications," *Biomaterials*, vol. 24, pp. 4337–4351, 2003.

[51] Y. Taguchi, N. Amizuka, M. Nakadate, H. Ohnishi, N. Fujii, K. Oda, S. Nomura, and T. Maeda, "A histological evaluation for guided bone regeneration induced by a collagenous membrane," *Biomater.* 26(31, vol. 26, no. 31, pp. 6158–6166, 2005.

[52] B. Zhang, Q. Luo, B. Deng, Y. Morita, Y. Ju, and G. Song, "Construction of tendon replacement tissue based on collagen sponge and mesenchymal stem cells by coupled mechano-chemical induction and evaluation of its tendon repair abilities," *Acta Biomater.*, vol. 74, pp. 247–259, 2018.

[53] H. Keshaw, N. Thapar, A. J. Burns, N. Mordan, J. C. Knowles, A. Forbes, and R. M. Day, "Microporous collagen spheres produced via thermally induced phase separation for tissue regeneration," *Acta Biomater.*, vol. 6, no. 3, pp. 1158–1166, 2010.

[54] A. Sobczak-Kupiec, A. Drabczyk, W. Florkiewicz, M. Głąb, S. Kudłacik-Kramarczyk, D. Słota, A. Tomala, and B. Tyliszczak, "Review of the applications of biomedical compositions containing hydroxyapatite and collagen modified by bioactive components," *Materials (Basel).*, vol. 14, no. 9, 2021.

[55] Y. F. Qian, K. H. Zhang, F. Chen, Q. F. Ke, and X. M. Mo, "Cross-linking of gelatin and chitosan complex nanofibers for tissue-engineering scaffolds," *J. Biomater. Sci. Polym. Ed.*, vol. 22, no. 8, pp. 1099–1113, 2011.

[56] J. W. Nichol, S. T. Koshy, H. Bae, C. M. Hwang, S. Yamanlar, and A. Khademhosseini, "Cell-laden microengineered gelatin methacrylate hydrogels," *Biomaterials*, vol. 31, no. 21, pp. 5536–5544, 2010.

[57] Schrieber R and Gareis H, Gelatine Handbook: Theory and Industrial Practice. John Wiley & Sons., 2007.

[58] A. J. Kuijpers, G. H. M. Engbers, J. Krijgsveld, S. A. J. Zaat, J. Dankert, and J. Feijen, "Cross-linking and characterisation of gelatin matrices for

biomedical applications," *J. Biomater. Sci. Polym. Ed.*, vol. 11, no. 3, pp. 225–243, 2000.

[59]   P. Fagerholm, N. S. Lagali, K. Merrett, W. B. Jackson, R. Munger, Y. Liu, J. W. Polarek, M. Söderqvist, and M. Griffith, "A biosynthetic alternative to human donor tissue for inducing corneal regeneration: 24-Month follow-up of a phase 1 clinical study," *Sci. Transl. Med.*, vol. 2, no. 46, 2010.

[60]   L. Ren, K. Tsuru, S. Hayakawa, and A. Osaka, "Novel approach to fabricate porous gelatin–siloxane hybrids for bone tissue engineering," *Biomaterials*, vol. 23, no. 24, pp. 4765–4773, 2002.

[61]   Y. Ge, J. Wang, Z. Shi, and J. Yin, "Gelatin-assisted fabrication of water-dispersible graphene and its inorganic analogues," *J. Mater. Chem.*, vol. 22, no. 34, pp. 17619–17624, 2012.

[62]   A. I. Van Den Bulcke, B. Bogdanov, N. De Rooze, E. H. Schacht, M. Cornelissen, and H. Berghmans, "Structural and rheological properties of methacrylamide modified gelatin hydrogels," *Biomacromolecules*, vol. 1, no. 1, pp. 31-38, 2000.

[63]   Z. Dong, Q. Yuan, K. Huang, W. Xu, G. Liu, and Z. Gu, "Gelatin methacryloyl (GelMA)-based biomaterials for bone regeneration," *RSC Adv.*, vol. 9, no. 31, pp. 17737–17744, 2019.

[64]   J. Wu, N. S. Lagali, K. Merrett, W. B. Jackson, R. Munger, Y. Liu, J. W. Polarek, M. Söderqvist, and M. Griffith, "Stem cell-laden injectable hydrogel microspheres for cancellous bone regeneration," *Chem. Eng. J.*, vol. 393, no. November 2019, p. 124715, 2020.

[65]   N. Celikkin, S. Mastrogiacomo, J. Jaroszewicz, X. F. Walboomers, and W. Swieszkowski, "Gelatin methacrylate scaffold for bone tissue engineering: The influence of polymer concentration," *J. Biomed. Mater. Res. - Part A*, vol. 106, no. 1, pp. 201–209, 2018.

[66] W. Schuurman, P. A. Levett, M. W. Pot, P. René van Weeren, W. J. A. Dhert, D. W. Hutmacher, F. P.W. Melchels, T. J. Klein, and J. Malda, "Gelatin-methacrylamide hydrogels as potential biomaterials for fabrication of tissue-engineered cartilage constructs," *Macromol. Biosci.*, vol. 13, no. 5, pp. 551–561, 2013.

[67] H. Shin, J. W. Nichol, and A. Khademhosseini, "Cell-adhesive and mechanically tunable glucose-based biodegradable hydrogels," *Acta Biomater.,* vol. 7, no. 1, pp. 106–114, 2011.

[68] Y. Lee, J. M. Lee, P.-K. Bae, I. Y. Chung, B. H. Chung, and B. G. Chung, "Photo-crosslinkable hydrogel-based 3D microfluidic culture device," *Electrophoresis*, vol. 36, no. 7–8, p. NA-NA, 2015.

[69] M. K. Joshi, S. Lee, A. P. Tiwari, B. Maharjan, S. B. Poudel, C. H. Park, and C. S. Kim, "Integrated design and fabrication strategies for biomechanically and biologically functional PLA/β-TCP nanofiber reinforced GelMA scaffold for tissue engineering applications," *Int. J. Biol. Macromol.*, vol. 164, pp. 976–985, 2020.

[70] X. Hou, Y. Chen, F. Chen, J. Liu, T. Wang, Y. Luo, S. Jia, P. Wang, S. Tan, B. Lu, Z. Zhou, and L. Zheng, "The hydroxyapatite microtubes enhanced GelMA hydrogel scaffold with inner 'pipeline framework' structure for bone tissue regeneration," *Compos. Part B Eng.*, vol. 228, p. 109396, 2022.

[71] S. Xiao, T. Zhao, J. Wang, C. Wang, J. Du, L. Ying, J. Lin, C. Zhang, W. Hu, L. Wang, and K. Xu, "Gelatin Methacrylate (GelMA)-Based Hydrogels for Cell Transplantation: an Effective Strategy for Tissue Engineering," *Stem Cell Rev. Reports*, vol. 15, no. 5, pp. 664–679, 2019.

[72] H. Stratesteffen, M. Köpf, F. Kreimendahl, A. Blaeser, S. Jockenhoevel, and H. Fischer, "GelMA-collagen blends enable drop-on-demand 3D printablility and promote angiogenesis.," *Biofabrication*, vol. 9, no. 4, p. 45002, Sep. 2017.

[73] W. Xiao, J. He, J. W. Nichol, L. Wang, C. B. Hutson, B. Wang, Y. Du, H. Fan, and A. Khademhosseini, "Synthesis and characterization of photocrosslinkable gelatin and silk fibroin interpenetrating polymer network hydrogels.," *Acta Biomater.*, vol. 7, no. 6, pp. 2384–2393, 2011.

[74] D. N. Heo, N. J. Castro, S.-J. Lee, H. Noh, W. Zhu, and L. G. Zhang, "Enhanced bone tissue regeneration using a 3D printed microstructure incorporated with a hybrid nano hydrogel," *Nanoscale*, vol. 9, no. 16, pp. 5055–5062, 2017.

[75] J. P. Magnusson, A. O. Saeed, F. Fernández-Trillo, and C. Alexander, "Synthetic polymers for biopharmaceutical delivery," *Polym. Chem.*, vol. 2, no. 1, pp. 48–59, 2011.

[76] M. Hakkarainen and A. C. Albertsson, "Degradation products of aliphatic and aliphatic-aromatic polyesters," *Adv. Polym. Sci.*, vol. 211, no. 1, pp. 85–116, 2008.

[77] E. S. Place, J. H. George, C. K. Williams, and M. M. Stevens, "Synthetic polymer scaffolds for tissue engineering," *Chemical Society Reviews*, vol. 38, no. 4. pp. 1139–1151, 2009.

[78] P. A. Gunatillake, R. Adhikari, and N. Gadegaard, "Biodegradable synthetic polymers for tissue engineering," *Eur. Cells Mater.*, vol. 5, pp. 1–16, 2003.

[79] A. C. Albertsson and I. K. Varma, "Recent developments in ring opening polymerization of lactones for biomedical applications," *Biomacromolecules*, vol. 4, no. 6, pp. 1466–1486, 2003.

[80] S. Farah, D. G. Anderson, and R. Langer, "Physical and mechanical properties of PLA, and their functions in widespread applications — A comprehensive review," *Adv. Drug Deliv. Rev.*, vol. 107, pp. 367–392, 2016.

[81] C. Zhou, Q. Shi, W. Guo, L. Terrell, A. T. Qureshi, D. J. Hayes, and Q. Wu, "Electrospun bio-nanocomposite scaffolds for bone tissue engineering by

cellulose nanocrystals reinforcing maleic anhydride grafted PLA," *ACS Appl. Mater. Interfaces*, vol. 5, no. 9, pp. 3847–3854, 2013.

[82] J. C. Middleton and A. J. Tipton, "Synthetic biodegradable polymers as orthopedic devices," *Biomaterials*, vol. 21, no. 23, pp. 2335–2346, 2000.

[83] Y. Ramot, M. Haim-Zada, A. J. Domb, and A. Nyska, "Biocompatibility and safety of PLA and its copolymers," *Adv. Drug Deliv. Rev.*, vol. 107, pp. 153–162, 2016.

[84] M. Guvendiren, J. Molde, R. M. D. Soares, and J. Kohn, "Designing Biomaterials for 3D Printing," *ACS Biomater. Sci. Eng.*, vol. 2, no. 10, pp. 1679–1693, 2016.

[85] A. J. R. Lasprilla, G. A. R. Martinez, B. H. Lunelli, A. L. Jardini, and R. M. Filho, "Poly-lactic acid synthesis for application in biomedical devices - A review," *Biotechnol. Adv.*, vol. 30, no. 1, pp. 321–328, 2012.

[86] G. W. Hastings, C. Chem, P. Ducheyne, Macromolecular Biomaterials, 1st ed., CRC Press, Boca Raton, 1984.

[87] J. Yang, G. Shi, J. Bei, S. Wang, Y. Cao, Q. Shang, G. Yang, and W. Wang, "Fabrication and surface modification of macroporous poly(L-lactic acid) and poly(L-lactic-co-glycolic acid) (70/30) cell scaffolds for human skin fibroblast cell culture," *J. Biomed. Mater. Res.*, vol. 62, no. 3, pp. 438–446, 2002.

[88] P. Gentile, V. Chiono, I. Carmagnola, and P. V. Hatton, "An overview of poly(lactic-co-glycolic) Acid (PLGA)-based biomaterials for bone tissue engineering," *Int. J. Mol. Sci.*, vol. 15, no. 3, pp. 3640–3659, 2014.

[89] M. A. Valantin, C. Aubron-Olivier, J. Ghosn, E. Laglenne, M. Pauchard, H. Schoen, R. Bousquet, P. Katz, D. Costagliola, and C. Katlama, "Polylactic acid implants (New-Fill)® to correct facial lipoatrophy in HIV-infected

patients: Results of the open-label study VEGA," *Aids*, vol. 17, no. 17, pp. 2471–2477, 2003.

[90] R. Fitzgerald, L. M. Bass, D. J. Goldberg, M. H. Graivier, and Z. P. Lorenc, "Physiochemical Characteristics of Poly-L-Lactic Acid (PLLA)," *Aesthetic Surg. J.*, vol. 38, no. April, pp. S13–S17, 2018.

[91] N. Rodrigues et al., "Manufacture and Characterisation of Porous PLA Scaffolds," *Procedia CIRP*, vol. 49, pp. 33–38, 2016.

[92] R. Donate, M. Monzón, M. E. Alemán-Domínguez, and Z. Ortega, "Enzymatic degradation study of PLA-based composite scaffolds," *Rev. Adv. Mater. Sci.*, vol. 59, no. 1, pp. 170–175, 2020.

[93] F. S. Senatov, K. V. Niaza, M. Y. Zadorozhnyy, A. V. Maksimkin, S. D. Kaloshkin, and Y. Z. Estrin, "Mechanical properties and shape memory effect of 3D-printed PLA-based porous scaffolds," *J. Mech. Behav. Biomed. Mater.*, vol. 57, pp. 139–148, 2016.

[94] H. Zhang, X. Mao, Z. Du, W. Jiang, X. Han, D. Zhao, D. Han, and Q. Li, "Three dimensional printed macroporous polylactic acid/hydroxyapatite composite scaffolds for promoting bone formation in a critical-size rat calvarial defect model," *Sci. Technol. Adv. Mater.*, vol. 17, no. 1, pp. 136–148, 2016.

[95] S. Sahmani, A. Khandan, S. Esmaeili, S. Saber-Samandari, M. Ghadiri Nejad, and M. M. Aghdam, "Calcium phosphate-PLA scaffolds fabricated by fused deposition modeling technique for bone tissue applications: Fabrication, characterization and simulation," *Ceram. Int.*, vol. 46, no. 2, pp. 2447–2456, 2020.

[96] F. S. Senatov, K. V. Niaza, A. A. Stepashkin, and S. D. Kaloshkin, "Low-cycle fatigue behavior of 3d-printed PLA-based porous scaffolds," *Compos. Part B Eng.*, vol. 97, pp. 193–200, 2016.

[97]   T. Yang, Y. Hu, C. Wang, and B. P. Binks, "Fabrication of Hierarchical Macroporous Biocompatible Scaffolds by Combining Pickering High Internal Phase Emulsion Templates with Three-Dimensional Printing," *ACS Appl. Mater. Interfaces*, vol. 9, no. 27, pp. 22950–22958, 2017.

[98]   S. Hassanajili, A. Karami-Pour, A. Oryan, and T. Talaei-Khozani, "Preparation and characterization of PLA/PCL/HA composite scaffolds using indirect 3D printing for bone tissue engineering," *Mater. Sci. Eng. C*, vol. 104, no. March, 2019.

[99]   T. Serra, J. A. Planell, and M. Navarro, "High-resolution PLA-based composite scaffolds via 3-D printing technology," *Acta Biomater.*, vol. 9, no. 3, pp. 5521–5530, 2013.

[100] X. Chen, C. Gao, J. Jiang, Y. Wu, P. Zhu, and G. Chen, "3D printed porous PLA/nHA composite scaffolds with enhanced osteogenesis and osteoconductivityin vivo for bone regeneration," *Biomed. Mater.*, vol. 14, no. 6, 2019.

[101] T. Kokubo, Bioceramics and Their Clinical Applications. Elsevier: Amsterdom, The Netherlands, 2008.

[102] L. L. Hench, An Introduction to Bioceramics. Singapore: World Scientific, 2013.

[103] P. Diaz-Rodriguez and M. Landin, "Biomorphic Ceramics for Drug Delivery in Bone Tissue Regeneration," *Curr. Pharm. Des.*, vol. 23, no. 24, pp. 3507–3514, 2017.

[104] D. Arcos and M. Vallet-Regí, "Bioceramics for drug delivery," *Acta Mater.*, vol. 61, no. 3, pp. 890–911, 2013.

[105] G. Fernandez de Grado, L. Keller, Y. Idoux-Gillet, Q. Wagner, A. M. Musset, N. Benkirane-Jessel, F. Bornert, and D. Offner, "Bone substitutes: a review

of their characteristics, clinical use, and perspectives for large bone defects management," *Journal of Tissue Engineering*, vol. 9. 2018.

[106] K. Lin, C. Wu, and J. Chang, "Advances in synthesis of calcium phosphate crystals with controlled size and shape," *Acta Biomater.*, vol. 10, no. 10, pp. 4071–4102, 2014.

[107] C. E. Corcione, F. Gervaso, F. Scalera, S. Padmanabhan, M. Madaghiele, F. Montagna, A. Sannino, A. Licciulli, and A. Maffezzoli, "Highly loaded hydroxyapatite microsphere/ PLA porous scaffolds obtained by fused deposition modelling," *Ceram. Int.*, vol. 45, no. 2, pp. 2803–2810, 2019.

[108] C. Cunha, S. Sprio, S. Panseri, M. Dapporto, M. Marcacci, and A. Tampieri, "High biocompatibility and improved osteogenic potential of novel Ca-P/titania composite scaffolds designed for regeneration of load-bearing segmental bone defects," *J. Biomed. Mater. Res. - Part A,* vol. 101 A, no. 6, pp. 1612–1619, 2013.

[109] Z. Tang, X. Li, Y. Tan, H. Fan, and X. Zhang, "The material and biological characteristics of osteoinductive calcium phosphate ceramics," *Regen. Biomater.*, vol. 5, no. 1, pp. 43–59, 2018.

[110] S. S. Liao, F. Z. Cui, W. Zhang, and Q. L. Feng, "Hierarchically Biomimetic Bone Scaffold Materials: Nano-HA/Collagen/PLA Composite," *J. Biomed. Mater. Res. - Part B Appl. Biomater.*, vol. 69, no. 2, pp. 158–165, 2004.

[111] Z. Xiong, Y. Yan, S. Wang, R. Zhang, and C. Zhang, "Fabrication of porous scaffolds for bone tissue engineering via low-temperature deposition," *Scr. Mater.*, vol. 46, no. 11, pp. 771–776, 2002.

[112] M. Barbeck. T. Serra, P. Booms, S. Stojanovic, S. Najman, E. Engel, R. Sader, C. J. Kirkpatrick, M. Navarro, and S. Ghanaati, "Analysis of the in vitro degradation and the in vivo tissue response to bi-layered 3D-printed scaffolds combining PLA and biphasic PLA/bioglass components –

Guidance of the inflammatory response as basis for osteochondral regeneration," *Bioact. Mater.*, vol. 2, no. 4, pp. 208–223, 2017.

[113] K. Eldesoqi, D. Henrich, A. M. El-Kady, M. S. Arbid, B. M. Abd El-Hady, I. Marzi, and C. Seebach, "Safety evaluation of a bioglass-polylactic acid composite scaffold seeded with progenitor cells in a rat skull critical-size bone defect," *PLoS One*, vol. 9, no. 2, pp. 1–13, 2014.

[114] S. Eqtesadi, A. Motealleh, F. H. Perera, A. Pajares, and P. Miranda, "Poly-(lactic acid) infiltration of 45S5 Bioglass® robocast scaffolds: Chemical interaction and its deleterious effect in mechanical enhancement," *Mater. Lett.*, vol. 163, pp. 196–200, 2016.

[115] M. Laczka, K. Cholewa-Kowalska, A. Laczka-Osyczka, M. Tworzydlo, and B. Turyna, "Gel-derived materials of a CaO-P2O5-SiO2 system modified by boron, sodium, magnesium, aluminum, and fluorine compounds," *J. Biomed. Mater. Res.*, vol. 52, no. 4, pp. 601–612, 2000.

[116] A. A. El-Rashidy, J. A. Roether, L. Harhaus, U. Kneser, and A. R. Boccaccini, "Regenerating bone with bioactive glass scaffolds: A review of in vivo studies in bone defect models," *Acta Biomater.*, vol. 62, pp. 1–28, 2017.

[117] L. L. Hench and J. Wilson, An Introduction to Bioceramics, vol. 1. World Scientific Publishing Co. Pte. Ltd., 1993.

[118] S. K. Nandi, B. Kundu, and S. Datta, "Development and Applications of Varieties of Bioactive Glass Compositions in Dental Surgery, Third Generation Tissue Engineering, Orthopaedic Surgery and as Drug Delivery System," 2003.

[119] L. L. Hench and J. K. West, "Biological Applications of Bioactive Glasses," *Life Chem. Reports*, vol. 13, pp. 187–241, 1996.

[120] T. Albrektsson and C. Johansson, "Osteoinduction, osteoconduction and osseointegration," *European Spine Journal*, vol. 10, pp. 96–101, 2001.

[121] T. Serra, M. A. Mateos-Timoneda, J. A. Planell, and M. Navarro, "3D printed PLA-based scaffolds: A versatile tool in regenerative medicine," *Organogenesis*, vol. 9, no. 4, pp. 239–244, 2013.

[122] S. Anil, P. S. Anand, H. Alghamdi, and J. A. Jansen, "Dental Implant Surface Enhancement and Osseointegration," *Implant Dentistry: A Rapidly Evolving Practice*, InTech, Rijeka Croatia, 2005.

[123] B. Kükürtcü, "Biyoaktif Cam ve Cam-Seramik Malzemelerin Üretimi ve Yapay Vücut Sivisi İçerisindeki Davranimlarinin İncelenmesi," İstanbul Teknik Üniversites, 2008.

[124] J. N. Oliver, D. Zhu, Y. Su, X. Lu, P. Kuo, and J. Du, "Bioactive Materials Bioactive glass coatings on metallic implants for biomedical applications," *Bioact. Mater.*, vol. 4, no. September, pp. 261–270, 2019.

[125] Z. Abbasi, M. Bahrololoom, M. Shariat, and R. Bagheri, "Bioactive Glasses in Dentistry: A Review Bioactive Glasses in Dentistry: A Review," *J. Dent. Biomater.*, vol. 2, no. 1, 2015.

[126] M. Montazerian and E. D. Zanotto, "History and trends of bioactive glass-ceramics," *J. Biomed. Mater. Res. Part A*, vol. 104A, pp. 1231–1249, 2016.

[127] A. Kumar et al., "Bioactive Glass Nanoparticles (NovaMin ®) for Applications in Dentistry," *IOSR J. Dent. Med. Sci.*, vol. 14, no. 8, pp. 30–35, 2015.

[128] L. L. Hench, "The story of Bioglass," *Journal of Materials Science: Materials in Medicine,* vol. 17, pp. 967–978, 2006.

[129] C. Vichery and J. M. Nedelec, "Bioactive Glass Nanoparticles_ From Synthesis to Materials Design for Biomedical Applications," *Mater.*, vol. 9(4):288, 2016.

[130] W. Xia and J. Chang, "Preparation and characterization of nano-bioactive-glasses (NBG) by a quick alkali-mediated sol – gel method," *Mat. Lett.*, vol. 61, no. 3, pp. 3251–3253, 2007.

[131] A. Motealleh, S. Eqtesadi, A. Pajares, and P. Miranda, "Enhancing the mechanical and in vitro performance of robocast bioglass scaffolds by polymeric coatings: Effect of polymer composition," *J. Mech. Behav. Biomed. Mater.*, vol. 84, pp. 35–45, 2018.

[132] V. Maquet, A. R. Boccaccini, L. Pravata, I. Notingher, and R. Jérôme, "Porous poly(α-hydroxyacid)/Bioglass® composite scaffolds for bone tissue engineering. I: Preparation and in vitro characterisation," *Biomaterials*, vol. 25, no. 18, pp. 4185–4194, 2004.

[133] L. C. Gerhardt and A. R. Boccaccini, "Bioactive glass and glass-ceramic scaffolds for bone tissue engineering," *Materials (Basel).*, vol. 3, no. 7, pp. 3867–3910, 2010.

[134] J. R. Jones, L. M. Ehrenfried, and L. L. Hench, "Optimising bioactive glass scaffolds for bone tissue engineering," *Biomaterials,* vol. 27, pp. 964–973, 2006.

[135] L. M. Mukundan, R. Nirmal, D. Vaikkath, and P. D. Nair, "A new synthesis route to high surface area sol gel bioactive glass through alcohol washing: a preliminary study," *Biomatter*, 3(2), 2013.

[136] L. L. Hench, "Bioceramics: From Concept to Clinic," *J. Am. Ceram. Soc.*, vol. 74, no. 7, pp. 1487–1510, 1991.

[137] Z. Hong, A. Liu, L. Chen, X. Chen, and X. Jing, "Preparation of bioactive glass ceramic nanoparticles by combination of sol – gel and coprecipitation method," *J. Non. Cryst. Solids*, vol. 355, no. 6, pp. 368–372, 2009.

[138] L. Uebersax, H. Hagenmüller, S. Hofmann, E. Gruenbalatt, R. Müller, G. Vunjak-novakovic, D. L. Kaplan, H. P. Merkle, and L. Meinel, "Effect of

Scaffold Design on Bone Morphology In Vitro," *Tissue Eng*., vol. 12, no. 12, pp. 3417–3429, 2006.

[139]   V. Karageorgiou and D. Kaplan, "Porosity of 3D biomaterial scaffolds and osteogenesis," *Biomaterials*, vol. 6, pp. 5474–5491, 2005.

[140]   Z. Tang, X. Li, Y. Tan, and H. Fan, "The material and biological characteristics of osteoinductive calcium phosphate ceramics," *Regenerative Biomaterials,* pp. 43–59, 2018.

[141]   S. Bose, S. Vahabzadeh, and A. Bandyopadhyay, "Bone tissue engineering using 3D printing," *Materials Today*, vol. 16, no. 12. pp. 496–504, 2013.

[142]   F. Baino, S. Fiorilli, and C. Vitale-brovarone, "Bioactive glass-based materials with hierarchical porosity for medical applications : Review of recent advances," *Acta Biomater*., vol. 42, pp. 18–32, 2016.

[143]   P. Diaz-Rodriguez et al., "Drug-loaded biomimetic ceramics for tissue engineering," *Pharmaceutics*, vol. 10, no. 4. 2018.

[144]   X. D. Zhu, M. Sánchez, and M. Landin, "Effect of phase composition and microstructure of calcium phosphate ceramic particles on protein adsorption." *Acta Biomaterialia,* vol. 6, 4, pp. 1536-1541, 2010.

[145]   S. J. Hollister, R. D. Maddox, and J. M. Taboas, "Optimal design and fabrication of scaffolds to mimic tissue properties and satisfy biological constraints," *Biomaterials*, vol. 23, pp. 4095–4103, 2002.

[146]   J. M. Taboas, R. D. Maddox, P. H. Krebsbach, and S. J. Hollister, "Indirect solid free form fabrication of local and global porous, biomimetic and composite 3D polymer-ceramic scaffolds," *Biomaterials*, vol. 24, pp. 181–194, 2003.

[147]   U. Ritz, R. Gerke, H. Götz, S. Stein, and P. M. Rommens, "A new bone substitute developed from 3D-prints of polylactide (PLA) loaded with collagen i: An in vitro study," *Int. J. Mol. Sci*., vol. 18, no. 12, 2017.

[148] V. Martin, I. A. Ribeiro, M. M. Alves, L. Gonçalves, R. A. Claudio, L. Grenho, M. H. Fernandes, P. Gomes, C. F. Santos, and A. F. Bettencourt, "Engineering a multifunctional 3D-printed PLA-collagen-minocycline-nanoHydroxyapatite scaffold with combined antimicrobial and osteogenic effects for bone regeneration," *Mater. Sci. Eng. C*, vol. 101, no. March, pp. 15–26, 2019.

[149] S. Gómez, M. D. Vlad, J. López, and E. Fernández, "Design and properties of 3D scaffolds for bone tissue engineering," *Acta Biomater.*, vol. 42, pp. 341–350, 2016.

[150] B. Herath, S. Suresh, D. Downing, S. Cometta, R. Tino, N. J. Castro, M. Leary, B. Schmutz, M. -L. Wille, and D. W. Hutmacher, "Mechanical and geometrical study of 3D printed Voronoi scaffold design for large bone defects," *Mater. Des.*, vol. 212, p. 110224, 2021.

[151] H. Chen, Y. Liu, C. Wang, A. Zhang, B. Chen, Q. Han, and J. Wang, "Design and properties of biomimetic irregular scaffolds for bone tissue engineering," *Comput. Biol. Med.*, vol. 130, p. 104241, 2021.

[152] J. Nam, B. Starly, A. Darling, and W. Sun, "Computer Aided Tissue Engineering for Modeling and Design of Novel Tissue Scaffolds," *Comput. Aided. Des.* Appl., vol. 1, no. 1–4, pp. 633–640, 2004.

[153] S. Vijayavenkataraman, L. Y. Kuan, and W. F. Lu, "3D-printed ceramic triply periodic minimal surface structures for design of functionally graded bone implants," *Mater. Des.*, vol. 191, p. 108602, 2020.

[154] S. Yu, J. Sun, and J. Bai, "Investigation of functionally graded TPMS structures fabricated by additive manufacturing," *Mater. Des.*, vol. 182, p. 108021, 2019.

[155] L. Yang, C. Yan, H. Fan, Z. Li, C. Cai, P. Chen, Y. Shi, and S. Yang, "Investigation on the orientation dependence of elastic response in Gyroid

cellular structures," *J. Mech. Behav. Biomed. Mater.*, vol. 90, pp. 73–85, 2019.

[156] S. Bose, M. Roy, and A. Bandyopadhyay, "Recent advances in bone tissue engineering scaffolds," *Trends Biotechnol.*, vol. 30, no. 10, pp. 546–554, 2012.

[157] H. N. Chia and B. M. Wu, "Recent advances in 3D printing of biomaterials," *J. Biol. Eng.*, vol. 9, no. 1, pp. 1–14, 2015.

[158] R. Murugan, R. N. Mitilesh, and S. Singamneni, "Influence of process parameters on the mechanical behaviour and processing time of 3D printing," *Int. J. Mod. Manuf. Technol.*, vol. 10, no. 1, pp. 69–75, 2018.

[159] O. A. Mohamed, S. H. Masood, and L. J. Bhowmik, "Optimization of fused deposition modeling process parameters: a review of current research and future prospects," *Adv. Manuf.*, vol. 3, pp. 42–53, 2015.

[160] B. Duan, M. Wang, W. Y. Zhou, W. L. Cheung, Z. Y. Li, and W. W. Lu, "Three-dimensional nanocomposite scaffolds fabricated via selective laser sintering for bone tissue engineering," *Acta Biomater.*, vol. 6, no. 12, pp. 4495–4505, 2010.

[161] M. M. Barak and M. A. Black, "A novel use of 3D printing model demonstrates the effects of deteriorated trabecular bone structure on bone stiffness and strength," *J. Mech. Behav. Biomed. Mater.*, vol. 78, pp. 455–464, 2018.

[162] A. K. Sood, R. K. Ohdar, and S. S. Mahapatra, "Parametric appraisal of mechanical property of fused deposition modelling processed parts," *Mater. Des.,* vol. 31, pp. 287–295, 2010.

[163] J. S. Chohan, R. Singh, K. S. Boparai, R. Penna, and F. Fraternali, "Dimensional accuracy analysis of coupled fused deposition modeling and

vapour smoothing operations for biomedical applications," *Compos. Part B*, vol. 117, pp. 138–149, 2017.

[164] P. Parandoush and D. Lin, "A review on additive manufacturing of polymer-fiber composites," *Compos. Struct.*, vol. 182, pp. 36–53, 2017.

[165] Y.-C. Chou, D. Lee, T. M. Chang, Y. -H. Hsu, Y. -H. Yu, S. -J. Liu, S. W. - N. Ueng, "Development of a Three-Dimensional (3D) Printed Biodegradable Cage to Convert Morselized Corticocancellous Bone Chips into a Structured Cortical Bone Graft," *Int. J. Mol. Sci.*, vol. 17, no. 4, 2016.

[166] A. Grémare, V. Guduric, R. Bareille, V. Heroguez, S. Latour, N. L'heureux, J. -C. Fricain, S. Catros, and D. Le Nihouannen, "Characterization of printed PLA scaffolds for bone tissue engineering," *J. Biomed. Mater. Res. - Part A*, vol. 106, no. 4, pp. 887–894, 2018.

[167] S. Naghieh, M. Badrossamay, E. Foroozmehr, and M. Kharaziha, "Combination of PLA Micro-fibers and PCL-Gelatin Nano-fibers for Development of Bone Tissue Engineering Scaffolds," *Int. J. Swarm Intell. Evol. Comput.*, vol. 6, pp. 1–4, 2017.

[168] W. Wang, B. Zhang, M. Li, J. Li, C. Zhang, Y. Han, L. Wang, K. Wang, C. Zhou, L. Liu, Y. Fan, and X. Zhang, "3D printing of PLA/n-HA composite scaffolds with customized mechanical properties and biological functions for bone tissue engineering," *Compos. Part B Eng.,* vol. 224, p. 109192, 2021.

[169] S. A. Park, S. J. Lee, J. M. Seok, J. H. Lee, W. D. Kim, and I. K. Kwon, "Fabrication of 3D Printed PCL/PEG Polyblend Scaffold Using Rapid Prototyping System for Bone Tissue Engineering Application," *J. Bionic Eng.*, vol. 15, no. 3, pp. 435–442, 2018.

[170] E. Nyberg, A. Rindone, A. Dorafshar, and W. L. Grayson, "Comparison of 3D-Printed Poly-ε-Caprolactone Scaffolds Functionalized with Tricalcium Phosphate, Hydroxyapatite, Bio-Oss, or Decellularized Bone Matrix," *Tissue Eng. Part A*, vol. 23, no. 11–12, pp. 503–514, Jun. 2017.

[171] R. Donate, M. Monzón, and M. E. Alemán-Domínguez, "Additive manufacturing of PLA-based scaffolds intended for bone regeneration and strategies to improve their biological properties," *E-Polymers,* vol. 20, no. 1, pp. 571–599, 2020.

[172] E. H. Baran and H. Y. Erbi, "Surface Modification of 3D Printed PLA Objects by Fused Deposition Modeling: A Review," *Colloids and Interfaces*, vol. 3, no. 43, 2019.

[173] K. Anselme, "Osteoblast adhesion on biomaterials," *Biomaterials*, vol. 21, pp. 667–681, 2000.

[174] M. Bächle and R. Kohal, "A systematic review of the influence of different titanium surfaces on proliferation, differentiation and protein synthesis of osteoblast-like MG63 cells," *Clin Oral Implant. Res*., vol. Dec;15(6), pp. 683–692, 2004.

[175] K. Kim, J. S. Cho, S. Han, Y. W. Beag, B. H. Kang, S. Ha, and S. Koh, "Permanent Hydrophilic Surface Formation by Ion Assisted Reaction," in Engineering Conferences International, 2003.

[176] M. Padial-molina, P. Galindo-moreno, J. M. Fernández-barbero, F. O'Valle, A. B. Jódar-reyes, J. L. Ortega-vinuesa, and P. J. Ramón-torregrosa, "Role of wettability and nanoroughness on interactions between osteoblast and modified silicon surfaces," *Acta Biomater*., vol. 7, no. 2, pp. 771–778, 2011.

[177] W. Norde, "Adsorption of Proteins from Solution at the Solid-Liquid Interface," *Adv. Colloid Interface Sci*., vol. 25, pp. 267–340, 1986.

[178] S. Bodhak, S. Bose, and A. Bandyopadhyay, "Role of surface charge and wettability on early stage mineralizationand bone cell–materials interactions of polarized hydroxyapatite," *Acta Biomater*., vol. 5, pp. 178–2188, 2009.

[179] T. R. Kyriakides, "Molecular Events at Tissue – Biomaterial Interface," *Host Response to Biomaterials: The Impact of Host Response on Biomaterial Selection*, Academic Press, pp. 81-116, 2015.

[180] M. Nuzaimah, S. M. Sapuan, R. Nadlene, and M. Jawaid, "Sodium Hydroxide Treatment of Waste Rubber Crumb and Its Effects on Properties of Unsaturated Polyester Composites," *Appl. Sci.*, vol. 10, no. 3913, 2020.

[181] S. Cai, C. Wu, W. Yang, W. Liang, H. Yu, and L. Liu, "Recent advance in surface modi fi cation for regulating cell adhesion and behaviors," *Nanotechnol. Rev.*, vol. 9, no. 1, pp. 971–989, 2020.

[182] J. van den Dolder and J. Jansen, "The response of osteoblast-like cells towards collagen type I coating immobilized by p-nitrophenylchloroformate to titanium," *J Biomed Mater Res A.*, vol. 83, no. 3, pp. 712–719, 2007.

[183] B. Holmes, W. Zhu, J. Li, J. D. Lee, and L. G. Zhang, "Development of novel three-dimensional printed scaffolds for osteochondral regeneration," *Tissue Eng. - Part A*, vol. 21, no. 1–2, pp. 403–415, 2015.

[184] B. Holmes, K. Bulusu, M. Plesniak, and L. G. Zhang, "A synergistic approach to the design, fabrication and evaluation of 3D printed micro and nano featured scaffolds for vascularized bone tissue repair," *Nanotechnology*, vol. 27, no. 6, p. 64001, 2016.

[185] A. R. Boccaccini, I. Notingher, V. Maquet, and R. Jérôme, "Bioresorbable and bioactive composite materials based on polylactide foams filled with and coated by Bioglass® particles for tissue engineering applications," *J. Mater. Sci. Mater. Med.*, vol. 14, no. 5, pp. 443–450, 2003.

[186] M. Joshi and B. S. Butola, "Application technologies for coating, lamination and finishing of technical textiles," *Advances in the dyeing and finishing of technical textiles,* Woodhead Publishing Series in Textiles, pp. 355–411, 2013.

[187] I. A. Neacşu, A. I. Nicoara, O. R. Vasile, and B. Ş. Vasile, "Inorganic micro-and nanostructured implants for tissue engineering," *Nanobiomaterials in Hard Tissue Engineering*, pp. 271–295, 2016.

[188] M. Camović, A. Biščević, I. Brčić, K. Borčak, S. Bušatlić, N. Ćenanović, A. Dedović, A. Mulalić, M. Osmanlić, M. Sirbubalo, A. Tucak, and E. Vranić, "Coated 3D Printed PLA Microneedles as Transdermal Drug Delivery Systems," *IFMBE Proceedings - CMBEBIH*, vol. 73, pp. 735–742, 2019.

[189] J. Zhu, J. L. Chen, R. K. Lade, W. J. Suszynski, and L. F. Francis, "Water-based coatings for 3D printed parts," *J. Coatings Technol. Res.*, vol. 12, no. 5, pp. 889–897, 2015.

[190] M. Schneider, C. Günter, and T. Andreas, "Co-deposition of a hydrogel/calcium phosphate hybrid layer on 3D printed poly(lactic acid) scaffolds via dip coating: Towards automated biomaterials fabrication," *Polymers (Basel).*, vol. 10, no. 3, 2018.

[191] C. A. Haynes and W. Norde, "Globular proteins at solid / liquid interfaces," *Colloids Surfaces B Biointerfaces*, vol. 2, no. 6, pp. 517–566, 1994.

[192] M. Malmsten, "Biopolymers at Interfaces," Biopolymers at Interfaces, New York: Dekker, 1998, p. 181.

[193] D. Becker, U. Geißler, U. Hempel, S. Bierbaum, D. Scharnweber, H. Worch, and K. W. Wenzel, "Proliferation and differentiation of rat calvarial osteoblasts on type I collagen-coated titanium alloy," *J Biomed Mater Res*, vol. 59, pp. 516–527, 2002.

[194] H. Huang, Y. Zhao, Z. Liu, Y. Zhang, H. Zhang, T. Fu, and X. Ma, "Enhanced Osteoblast Functions on RGD Immobilized Surface," *J Oral Implant.*, vol. 29, no. 2, pp. 73–79, 2003.

[195] Y. Ku, C. Chung, and J. Jang, "The effect of the surface modification of titanium using a recombinant fragment of fibronectin and vitronectin on cell behavior," *Biomaterials*, vol. 26, no. 25, pp. 5153–5157, 2005.

[196] Y. Yang, R. Cavin, and J. Ong, "Protein adsorption on titanium surfaces and their effect on osteoblast attachment," *J Biomed Mater Res A.*, vol. 67, no. 1, pp. 344–349, 2003.

[197] M. Vandrovcová, T. Douglas, D. Hauk, B. Grössner-Schreiber, J. Wiltfang, L. Bačáková, and P. H. Warnke, "Influence of Collagen and Chondroitin Sulfate (CS) Coatings on Poly-(Lactide-co-Glycolide) (PLGA) on MG 63 Osteoblast-Like Cells," *Physiol. Res.*, vol. 60, pp. 797–813, 2011.

[198] M. Mizuno, R. Fujisawa, and Y. Kuboki, "Type I collagen-induced osteoblastic differentiation of bone-marrow cells mediated by collagen-α2β1 integrin interaction," *J Cell Physiol.*, vol. 184, no. 2, pp. 207–213, 2000.

[199] U. Geißler, U. Hempel, C. Wolf, D. Scharnweber, H. Worch, and K. Wenzel, "Collagen type I-coating of Ti6Al4V promotes adhesion of osteoblasts," *J. Biomed. Mater. Res.*, vol. 51, no. 4, pp. 752–760, 2000.

[200] C. Wang, W. Huang, Y. Zhou, L. He, Z. He, Z. Chen, X. He, S. Tian, J. Liao, B. Lu, Y. Wei, and M. Wang, "3D printing of bone tissue engineering scaffolds," *Bioact. Mater.*, vol. 5, no. 1, pp. 82–91, 2020.

[201] D. H. Rosenzweig, E. Carelli, T. Steffen, P. Jarzem, and L. Haglund, "3D-printed ABS and PLA scaffolds for cartilage and nucleus pulposustissue regeneration," *Int. J. Mol. Sci.*, vol. 16, no. 7, pp. 15118–15135, Jul. 2015.

[202] M. F. Afrose, S. H. Masood, P. Iovenitti, M. Nikzad, and I. Sbarski, "Effects of part build orientations on fatigue behaviour of FDM-processed PLA material," *Prog. Addit. Manuf.*, vol. 1, no. 1–2, pp. 21–28, 2016.

[203] O. H. Ezeh and L. Susmel, "Fatigue strength of additively manufactured polylactide (PLA): effect of raster angle and non-zero mean stresses," *Int. J. Fatigue*, vol. 126, no. March, pp. 319–326, 2019.

[204] D. W. Abbot, D. V. V. Kallon, C. Anghel, and P. Dube, "Finite element analysis of 3D printed model via compression tests," *Procedia Manuf.*, vol. 35, pp. 164–173, 2019.

[205] L. Polo-Corrales, M. Latorre-Estevas, and J. E. Ramirez-Vick, "Scaffold Design for Bone Regeneration," *Nanosci Nanotechnol.*, vol. 14, no. 1, pp. 15–56, 2014.

[206] J. Bae, C. Oh, J. Nam, J. Lee, and H. Lee, "A tensile test technique for the freestanding PMMA thin films," *Curr. Appl. Phys.*, vol. 9, no. 1, pp. S107–S109, 2009.

[207] J. R. C. Dizon, A. H. Espera, Q. Chen, and R. C. Advincula, "Mechanical characterization of 3D-printed polymers," *Addit. Manuf.*, vol. 20, pp. 44–67, 2018.

[208] K. V. Niaza, F. S. Senatov, S. D. Kaloshkin, A. V. Maksimkin, and D. I. Chukov, "3D-printed scaffolds based on PLA/HA nanocomposites for trabecular bone reconstruction," *J. Phys. Conf. Ser.*, vol. 741, no. 1, 2016.

[209] A. Szojka, K. Lalh, S. H. J. Andrews, N. M. Jomha, M. Osswald, and A. B. Adesida, "Biomimetic 3D printed scaffolds for meniscus tissue engineering," *Bioprinting*, vol. 8, no. April, pp. 1–7, 2017.

[210] "Rhinoceros forums-Solid porous voronoi structure and porosity percentage." [Online]. Available: https://discourse.mcneel.com/t/solid-porous-voronoi-structure-and-porosity-percentage/83579/3. [Accessed: 11-Oct-2021].

[211] "Parametric house-Gyroid Minimal Surface." [Online]. Available: https://parametrichouse.com/gyroid-minimal-surface/. [Accessed: 11-Oct-2021].

[212] "Triply Periodic Minimal Surfaces." [Online]. Available: https://wewanttolearn.wordpress.com/2019/02/03/triply-periodic-minimal-surfaces/. [Accessed: 11-Oct-2021].

[213] P. Glover, "Chapter 5: Porosity." [Online]. Available: http://homepages.see.leeds.ac.uk. [Accessed: 25-Jan-2022].

[214] H. Mirsandi, W. J. Smit, G. Kong, M. W. Baltussen, E. A. J. F. Peters, and J. A. M. Kuipers, "Influence of wetting conditions on bubble formation from a submerged orifice," *Exp. Fluids*, vol. 61, no. 3, p. 83, 2020.

[215] R. M. Rad, "Borate Modified Bioglass Containing Scaffolds for Dental Tissue Engineering Applications," Middle East Technical University, 2018.

[216] H. Jodati, Z. Evis, and D. Keskin, "Synthesis and characterization of magnesium-lanthanum dual doped bioactive glasses," *Ceramics International,* vol. 46, pp. 10503–10511, 2020.

[217] V. Mortazavi, M. Mehdikhani Nahrkhalaji, M. H. Fathi, S. B. Mousavi, and B. Nasr Esfahani, "Antibacterial effects of sol-gel-derived bioactive glass nanoparticle on aerobic bacteria," *J. Biomed. Mater. Res.* - Part A, vol. 94, no. 1, pp. 160–168, 2010.

[218] A. S. Alagoz, J. C. Rodriguez-Cabello, and V. Hasirci, "PHBV wet-spun scaffold coated with ELR-REDV improves vascularization for bone tissue engineering," *Biomed. Mater.*, vol. 13, no. 5, 2018.

[219] A. Doostmohammadi, A. Monshi, R. Salehi, M. H. Fathi, Z. Golniya, and A. U. Daniels, "Bioactive glass nanoparticles with negative zeta potential," *Ceram. Int.,* vol. 37, no. 7, pp. 2311–2316, 2011.

[220] R. de Tayrac, S. Chentouf, H. Garreau, C. Braud, I. Guiraud, P. Boudeville, M. Vert, "In vitro degradation and in vivo biocompatibility of poly(lactic acid) mesh for soft tissue reinforcement in vaginal surgery.," J. *Biomed. Mater. Res. B. Appl. Biomater.*, vol. 85, no. 2, pp. 529–536, 2008.

[221] X. Yuan, A. F. T. Mak, and K. Yao, "Comparative observation of accelerated degradation of poly(L-lactic acid) fibres in phosphate buffered saline and a dilute alkaline solution," *Polym. Degrad. Stab.*, vol. 75, pp. 45–53, 2002.

[222] B. Qian, X. Liang, S. Yang, S. He, and L. Gao, "Effects of lanthanum addition on the structure and properties of iron phosphate glasses," *J. Mol. Struct.*, vol. 1027, pp. 31–35, 2012.

[223] W. Xia, and J. Chang, "Preparation and Characterization of Nano-Bioactive-Glasses (NBG) by a quick alkali-mediated sol – gel method," *Mat. Lett.*, vol. 61, pp. 3251-3252, 2007.

[224] S. Grangeon, F. Claret, Y. Linard, and C. Chiaberge, "X-ray diffraction: a powerful tool to probe and understand the structure of nanocrystalline calcium silicate hydrates," *Acta Crystallogr. Sect. B*, vol. 69, no. 5, pp. 465–473, Oct. 2013.

[225] X. V. Bui and T. H. Dang, "Bioactive glass 58S prepared using an innovation sol-gel process," *Process. Appl. Ceram.*, vol. 13, no. 1, pp. 98–103, 2019.

[226] Y. F. Goh, A. Z. Alshemary, M. A. Akram, M. R. A. Kadir, and R. Hussain, "Bioactive Glass: An In_Vitro Comparative Study of Doping with Nanoscale Copper and Silver Particles*," Int. J. Appl. Glas. Sci.*, vol. 5, pp. 255–266, 2014.

[227] A. Meiszterics, L. Rosta, H. Peterlik, J. Rohonczy, S. Kubuki, P. Henits, and K. Sinkó, "Structural Characterization of Gel-Derived Calcium Silicate Systems," *J. Phys. Chem. A*, vol. 114, no. 38, pp. 10403–10411, Sep. 2010.

[228] D. Bellucci, R. Salvatori, A. Anesi, L. Chiarini, and V. Cannillo, "SBF assays, direct and indirect cell culture tests to evaluate the biological performance of bioglasses and bioglass-based composites: Three paradigmatic cases," *Mater. Sci. Eng. C*, vol. 96, pp. 757–764, 2019.

[229] L. L. Hench and J. K. West, "The sol-gel process," *Chem. Rev.*, vol. 90, no. 1, pp. 33–72, Jan. 1990.

[230] D. P. Ferreira, J. Cruz, and R. Fangueiro, "Chapter 1 - Surface modification of natural fibers in polymer composites," Green Composites for Automotive Applications, G. Koronis and A. Silva, Eds. Woodhead Publishing, 2019, pp. 3–41.

[231] C. Yang, U. Tartaglino, and B. N. J. Persson, "Influence of surface roughness on superhydrophobicity," *Phys. Rev. Lett.*, vol. 97, no. 11, pp. 1–4, 2006.

[232] S. Lee and C. H. Park, "Influence of alkaline treatment on surface roughness and wetting properties of hydrophobized silk fabrics," *Text. Res. J.*, vol. 88, no. 7, pp. 777–789, Jan. 2017.

[233] A. R. Sadeghi, S. Nokhasteh, A. M. Molavi, M. Khorsand-Ghayeni, H. Naderi-Meshkin, and A. Mahdizadeh, "Surface modification of electrospun PLGA scaffold with collagen for bioengineered skin substitutes," *Mater. Sci. Eng.* C, vol. 66, pp. 130–137, 2016.

[234] A. Fiorani, C. Gualandi, S. Panseri, M. Montesi, M. Marcacci, M. L. Focarete, and A. Bigi, "Comparative performance of collagen nanofibers electrospun from different solvents and stabilized by different crosslinkers," *J. Mater. Sci. Mater. Med.*, vol. 25, no. 10, pp. 2313–2321, 2014.

[235] A. M. El-Kady and A. F. Ali, "Fabrication and characterization of ZnO modified bioactive glass nanoparticles," *Ceram. Int.*, vol. 38, no. 2, pp. 1195–1204, 2012.

[236] C. D. F. Moreira, S. M. Carvalho, H. S. Mansur, and M. M. Pereira, "Thermogelling chitosan–collagen–bioactive glass nanoparticle hybrids as potential injectable systems for tissue engineering," *Mater. Sci. Eng. C*, vol. 58, pp. 1207–1216, 2016.

[237] M. M. Pereira, A. E. Clark, and L. L. Hench, "Calcium phosphate formation on sol-gel-derived bioactive glasses in vitro.," *J. Biomed. Mater. Res.*, vol. 28, no. 6, pp. 693–698, Jun. 1994.

[238] A. A. R. de Oliveira, D. A. de Souza, L. L. S. Dias, S. M. de Carvalho, H. S. Mansur, and M. de Magalhães Pereira, "Synthesis, characterization and cytocompatibility of spherical bioactive glass nanoparticles for potential hard tissue engineering applications," *Biomed. Mater.*, vol. 8, no. 2, p. 025011, Mar. 2013.

[239] Y. Zuo, X. Liu, D. Wei, J. Sun, W. Xiao, H. Zhao, L. Guo, Q. Wei, H. Fan, and X. Zhang, "Photo-Cross-Linkable Methacrylated Gelatin and Hydroxyapatite Hybrid Hydrogel for Modularly Engineering Biomimetic Osteon," *ACS Appl. Mater. Interfaces*, vol. 7, no. 19, pp. 10386–10394, May 2015.

[240] C. Bektaş, "3D Printed, Cell Carrying GelMA Hydrogels in Corneal Stroma Engineering," Middle East Technical University, 2018.

[241] S. Yu, L. M. Yerges-Armstrong, Y. Chu, J. M. Zmuda, and Y. Zhang, "Transcriptional Regulation of Frizzled-1 in Human Osteoblasts by Sp1.," *PLoS One*, vol. 11, no. 10, 2016.

[242] A. O. Lobo, S. Afewerki, M. M. M. de Paula, P. Ghannadian, F. R. Marciano, Y. S. Zhang, T. J. Webster, and A. Khademhosseini, "Electrospun nanofiber blend with improved mechanical and biological performance," *Int. J. Nanomedicine*, vol. 13, pp. 7891–7903, 2018.

[243] B. Setzer, M. Bächle, M. C. Metzger, and R. J. Kohal, "The gene-expression and phenotypic response of hFOB 1.19 osteoblasts to surface-modified titanium and zirconia.," *Biomaterials*, vol. 30, no. 6, pp. 979–990, 2009.

[244] O. Suzuki, S. Kamakura, and T. Katagiri, "Surface chemistry and biological responses to synthetic octacalcium phosphate.," *J. Biomed. Mater. Res. B. Appl. Biomater.*, vol. 77, no. 1, pp. 201–212, Apr. 2006.

[245] M. D. Francis and N. C. Webb, "Hydroxyapatite formation from a hydrated calcium monohydrogen phosphate precursor," *Calcif. Tissue Res*., vol. 6, no. 1, pp. 335–342, 1970.

[246] S. Jinawath, D. Pongkao, W. Suchanek, and M. Yoshimura, "Hydrothermal synthesis of monetite and hydroxyapatite from monocalcium phosphate monohydrate," *Int. J. Inorg. Mater*., vol. 3, no. 7, pp. 997–1001, 2001.

APPENDICES

A. Differential Scanning Calorimetry

The colorless Premium Poly-Lactic Acid (PLA) filaments were purchased from FormFutura (The Netherlands). The premium PLA is thermally stable, its crystallization process is faster than modified PLA, and it complies with Food and Drug Administration (FDA) regulations and legislation.

Differential Scanning Calorimetry (DSC) was conducted in Middle East Technical University Central Laboratory before and after treatment on PLA filaments. In this thermoanalytical method, the polymer's thermal transition is determined. The difference between the heat required for increasing the temperature of the sample and the reference can be measured as a function of temperature.

The Differential Scanning Calorimetry (DSC) curves are represented in Figure A.1 for the raw PLA (Figure A.1a), and PLA from 3D printed samples (Figure A.1b). A heat-cool-heat cycle at a fixed rate of 10 ℃/min from -50 to 200 ℃ is applied for both samples. The initial heating and cooling cycles are performed to eliminate the thermal history of the sample. The temperature is raised above the melting temperature (in this case, 200 ℃), followed by cooling to -50 ℃ at the same rate. Accordingly, the parameters of interest of the ""as-received"" sample can be determined from the first heating ramp. During the second heating ramp, the parameters of interest independent of the thermal history of the samples are obtained. In the results presented herein, convex curves represent an exothermic process (i.e. crystallization), and concave curves represent an endothermic process (i.e. melting). The first kink in the heat flow vs. temperature plot represents the glass transition point upon heating. The glass transition temperature is taken at the middle of the slope. It denotes the temperature at which the mechanical properties of a material change from brittle to elastic upon heating beyond the glass transition point. Following glass transition, the exothermic peak denotes crystallization, and the endothermic peak denotes melting.

185

Attending at the second heating ramp, i.e., the thermal history independent results, the glass transition temperature is similar for both samples, 57.3 and 56.5 ℃ for PLA and PLA Post T, respectively. Similarly, the crystallization temperatures are similar for both samples at 112.5 and 111.9 ℃. Finally, the melting temperatures for PLA and PLA Post T are 147.8 and 148.4 ℃.

"""""However, the properties of ""as received" " samples, obtained from the first heating rate, show some disparities. The glass transition temperature is again similar for both samples at 58.2 and 58.3 ℃. On the other hand, the crystallization temperature is slightly higher for the PLA Post T (104.1 ℃) as compared with the PLA (100.1 ℃), and the melting temperature of PLA Post T (151.1 ℃) is also above that of PLA (146.2 ℃). The results show that the 3D printing of PLA samples does not significantly affect the thermal properties of the material.
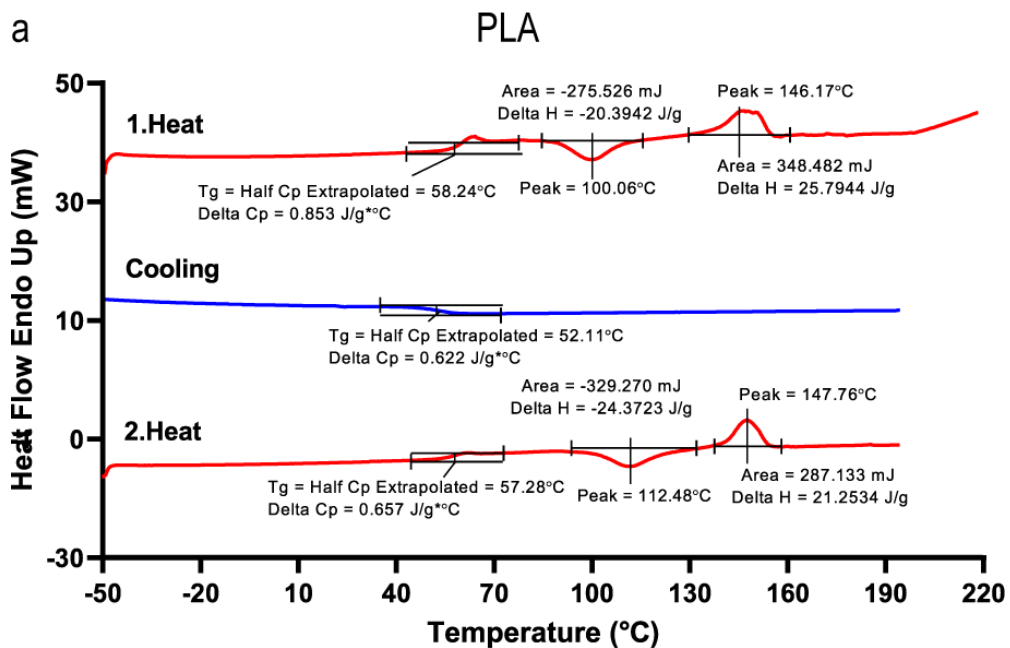

Figure A.1. DSC curves of heat flow vs. temperature for (a) a raw PLA and (b) PLA from 3D printed samples (Post T).
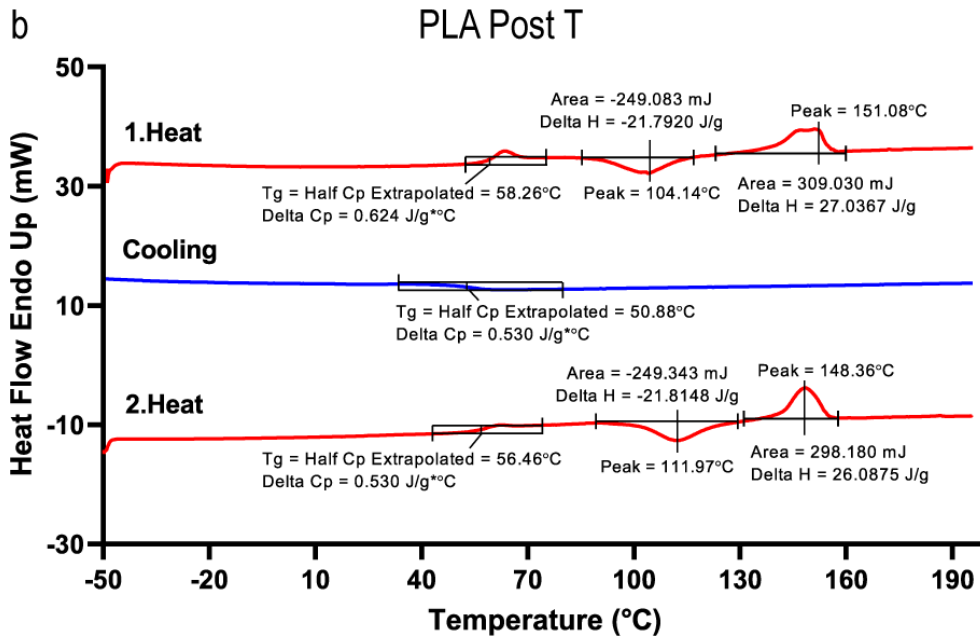
Figure A.1. (cont'd) DSC curves of heat flow vs. temperature for (a) a raw PLA and (b) PLA from 3D printed samples (Post T).
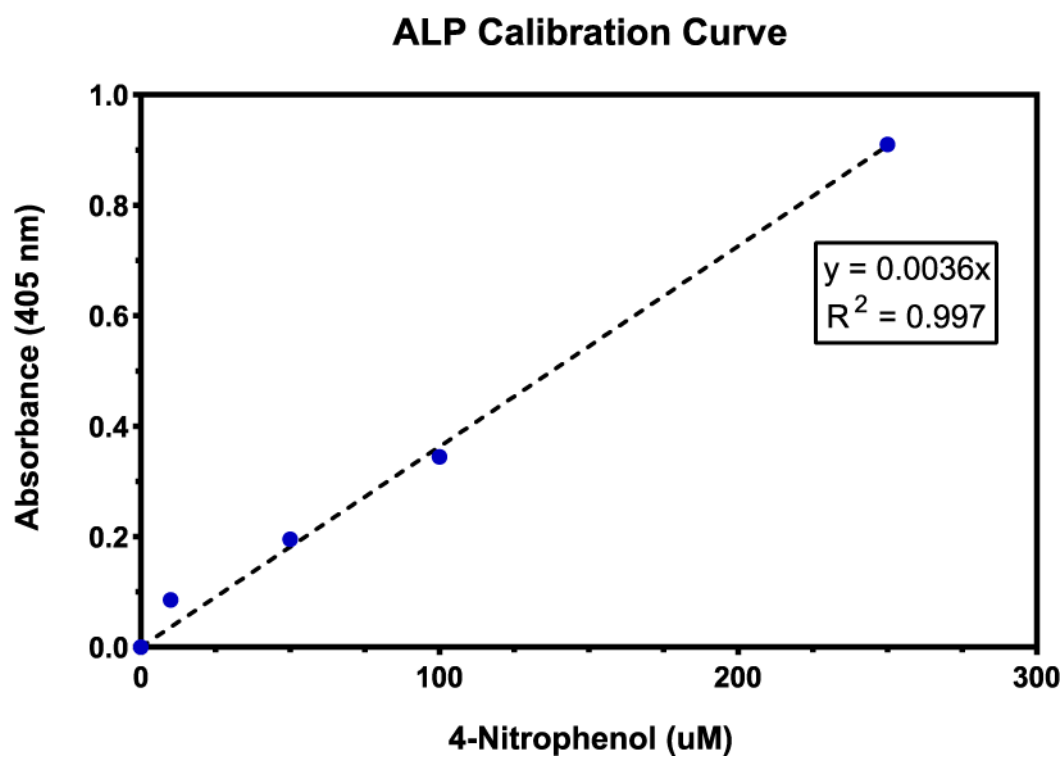
B. Calibration Curve for ALP

Figure B.1. Calibration curve for ALP assay. Different concentrations of 4-nitrophenol were used as a standard for the calibration curve.
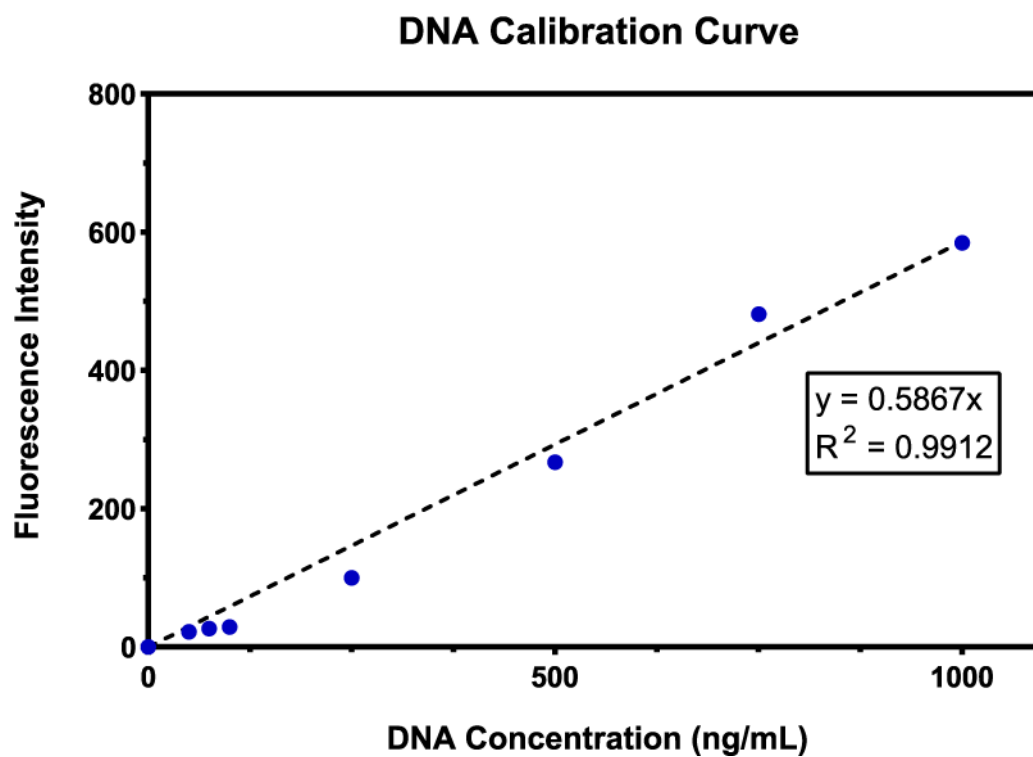
C. Calibration Curve for DNA Concentration

DNA Calibration Curve

$y = 0.5867x$
$R^2 = 0.9912$

Figure C.1. Calibration curve for DNA content. Different concentrations of λ DNA were used as a standard for the calibration curve.